UNIVERSITAT DE BARCELONA

Few Interacting Particles in Low-Dimensional Quantum Systems: From Harmonic Oscillators to Fractal Lattices

Abel Rojo Francàs

Doctoral thesis

Few Interacting Particles in Low-Dimensional Quantum Systems: From Harmonic Oscillators to Fractal Lattices

ABEL ROJO FRANCÀS

Dr. Bruno Juliá Díaz

UNIVERSITAT DE BARCELONA

Few Interacting Particles in Low-Dimensional Quantum Systems: From Harmonic Oscillators to Fractal Lattices

Memòria presentada per optar al grau de doctor per la
Universitat de Barcelona

Programa de doctorat en física

Autor
Abel Rojo Francàs

Director
Dr. Bruno Juliá Díaz

Tutor
Dr. Joan Soto Riera

UNIVERSITAT DE BARCELONA

Table of Contents

List of Figures

List of publications

This thesis is based on

- A. Rojo-Francàs, F. Isaule, B. Juliá-Díaz "Direct diagonalization method for a few particles trapped in harmonic potentials" Physical Review A **105**, 063326 (2022).
- A. Rojo-Francàs, F. Isaule, and B. Juliá-Díaz, "Few particles with an impurity in a one-dimensional harmonic trap", Physica Scripta **99**, 045408 (2024).
- A. Rojo-Francàs, P. Pansari, U. Bhattacharya, B. Juliá-Díaz, T. Grass "Anomalous quantum transport in fractal lattices" Commun Phys **7**, 259 (2024).
- A. Rojo-Francàs, F. Isaule, A. Santos, B. Juliá-Díaz, N. Zinner, "Stable collective charging of ultracold atoms quantum batteries", Phys. Rev. A **110**, 032205 (2024).

Other publications made during the Ph.D

- F. Sabater, A. Rojo-Francàs, G.E. Astrakharchik, and B. Juliá-Díaz, "A BCS state formulation for the fermionic Tonks-Girardeau gas", arXiv:2407.13270 (2024).
- F. Sabater, A. Rojo-Francàs, G.E. Astrakharchik, and B. Juliá-Díaz, "Universal Composite Boson Formation in Strongly Interacting One-Dimensional Fermionic Systems", Physical Review Letters **132**, 193401 (2024).
- A. Usui, A. Rojo-Francàs, J. Schloss, B. Juliá-Díaz, "Spin-orbit coupling in symmetric and mixed spin-symmetry", arXiv:2403.07188 (2024).
- F. Isaule, A. Rojo-Francàs, B. Juliá-Díaz "Bound impurities in a one-dimensional Bose lattice gas: low-energy properties and quench-induced dynamics", SciPost Phys. Core **7**, 049 (2024).
- J.W.T. Keeble, M. Drissi, A. Rojo-Francàs, B. Juliá-Díaz, A. Rios, "Machine learning one-dimensional spinless trapped fermionic systems with neural- network quantum states", Physical Review A **108**, 063320 (2023).

Abstract

Quantum mechanics is a fascinating field to explore, where its effects are usually non-trivial and counterintuitive. In this Thesis, we focus on systems with a small number of particles in low dimensions, where the quantum effects are enhanced. We consider experimentally realistic systems, considering either an external harmonic confinement or a lattice potential. These systems can be created nowadays in ultracold atom laboratories worldwide, where they can control the dimensionality, the external potential, as well as the number of particles and the interactions.

Our goal is to understand the static and dynamic properties of different systems involving few particles and a wide range of interactions. In particular, we focus on the one-dimensional harmonic trap, fractal lattices, and one-dimensional three-site lattices. In each system, we consider a contact interaction potential defined by a delta function in the continuum space or an on-site interaction for the lattices. In addition, we compute different properties, such as energy spectra, densities, pair correlations, mean square displacement, and population of each site, in both static and time-dependent cases.

We combine analytical and numerical techniques to study the different systems. In particular, the numerical part is mostly done using exact diagonalization techniques. With this approach, we can only examine systems with few particles due to the intrinsic limitations of the method, although it provides the capacity to obtain any property needed. The case of the harmonic oscillator trap includes an additional limitation due to the exact diagonalization method, as the basis must be truncated, resulting in upper-bound energies. We show how to correct this error and obtain a better estimate of the energy and the density by using the analytical solution of the two-particle system. We demonstrate that this correction works for a larger number of particles by computing results for up to eight particles.

For the systems with harmonic oscillator confinement, we compute the energy spectrum as a function of the interaction strength, the density for different interaction values, and pair correlations. We present the results for the symmetric $SU(N)$ case and then study systems with broken interaction symmetry. We present different interaction configurations, and we explore the ground state structure, where the correlations play an important role. We also consider the impurity case, where one particle interacts with all the bath particles but the bath particles do not interact with each other. We show that the impurity system can be mapped to an effective one particle in a double-well

model, showing two phases: the miscible and the immiscible.

Afterwards, we study fractal lattice systems, where the sites and the tunneling connections are configured in a non-standard scheme creating an effective finite representation of a fractal structure. Under this situation, we explore the effect on the transport of a single-particle obtaining the diffusion exponent and relating it to spectral properties. We demonstrate that the fractal slows down the motion of the particle and that this effect is robust against a random potential. Using the slower dynamics, we show how the fractal system can preserve information about the initial phase of the wavefunction for much longer times than a regular lattice. We also explore the entanglement of a two-particle system and how the interactions affect entanglement creation.

Finally, we study a three-site lattice where each site has a different energy and the couplings are time-dependent. We implement the spatial adiabatic passage protocol, that transfers a single particle from the first to the third site, and generalize it for a few particle systems with interactions. Due to the interactions, the adiabaticity of the protocol is lost, but we demonstrate that it is possible to populate the third state for certain interaction strength values. As a result, since the final state populates the most energetic site of the system, we propose this setup as a quantum battery model.

Resum

La mecànica quàntica és un camp fascinant a explorar, on els efectes solen ser no trivials i contraintuïtius. En aquesta Tesis, ens centrem en sistemes amb poques partícules i en dimensions petites, on els efectes quàntics s'accentuen. Considerem sistemes experimentalment realistes, considerant tant un confinament d'oscil·lador harmònic extern com un potencial reticular. Aquests sistemes poden ser creats actualment en laboratoris d'àtoms ultrafreds per tot el món, on poden controlar la geometria, els potencials externs, i també el numero de partícules i les interaccions. La interacció més comú en aquests sistemes es en ona s, modelitzat per una funció delta en les nostres simulacions.

El nostre objectiu és calcular numèricament les propietats de diferents sistemes que involucren poques partícules interactuant. En particular, ens centrem en un oscil·lador harmònic unidimensional, retícules fractals i retícules unidimensionals de tres pous. En cada sistema, considerem interaccions de contacte definides per una delta en l'espai continu o per una interacció in situ per a les retícules. En aquests casos, calculem diferents propietats com els espectres d'energia, densitats, correlacions a parelles, desplaçament quadràtic mitjà, població en cada pou, tant en casos estàtics com dependents del temps.

Obtenim els nostres resultats per mitjà de simulacions numèriques dels sistemes, on específicament fem servir el mètode de diagonalització exacta. Amb aquest plantejament, podem estudiar sistemes només amb poques partícules per les limitacions intrínseques del mètode, tot i que podem obtenir qualsevol propietat que necessitem. El cas de l'oscil·lador harmònic inclou una limitació addicional a la diagonalització exacta, ja que s'ha de truncar la base, amb l'efecte d'obtenir cotes superiors de la energia. Mostrem com corregir aquest error per obtenir una millor estimació de la energia i la densitat utilitzant el resultat analític del cas de dues partícules. Demostrem que aquesta correcció funciona per a més partícules obtenint resultats fins a vuit partícules.

Per als sistemes amb l'oscil·lador harmònic, calculem l'espectre d'energia en funció de la intensitat de la interacció, la densitat per a diferents valors de la interacció i les correlacions a parelles. Presentem els resultats per al cas simètric $SU(N)$ i després estudiem sistemes amb la simetria d'interacció trencada. Mostrem diferents configuracions d'interacció i explorem la estructura del estat fonamental, on les correlacions tenen un rol important. També estudiem el cas de sistemes amb una impuresa, on una partícula interacciona amb totes les partícules del bany però les partícules del bany no interaccionen entre elles. Mostrem que el sistema amb la impuresa es pot mapejar a un model

efectiu d'una partícula en un doble pou, tenint dues fases: la fase miscible i la immiscible.

A continuació, estudiem sistemes formats per una retícula fractal, on els pous i les connexions de tuneleig estan configurades en una forma no estàndard creant una representació finita d'una estructura fractal. En aquesta situació, explorem els efectes del transport d'una partícula obtenint l'exponent de difusió i relacionant-lo amb una propietat espectral. Demostrem que el fractal enlenteig el moviment i que aquest efecte és robust sota un potencial aleatori. Fent servir la dinàmica més lenta, mostrem com el sistema fractal preserva informació de la fase inicial de la funció d'ona per temps molt més llargs comparat amb les retícules estàndard. També explorem l'entrellaçament de sistemes de dues partícules i com la interacció afecta a la creació d'entrellaçament.

Finalment, estudiem un sistema de tres pous on cada pou té una energia diferent i els acoblaments tenen dependència temporal. Utilitzant el protocol SAP (pas adiabàtic espacial) que transfereix una partícula del primer pou al tercer, ho implementem per a sistemes amb poques partícules amb interaccions. Degut a les interaccions, la adiabacitat del protocol es perd, però demostrem que es possible poblar el tercer pou per a certs valors de la interacció. Proposem aquest sistema com a un model de bateria quàntica.

Acknowledgements

This Thesis would not be realized without the teachings, help, and support during my academic life.

First of all, I want to thank my Thesis supervisor, Bruno Juliá, who guided me during these last four years. Bruno, I have learned a lot from you, not only physics. Working with you has been a pleasure and I enjoyed it. Thank you for your closeness and support in the not-so-good moments and for your knowledge, patience, and explanations when the results were not the expected ones. Probably I can say that I have become a better researcher thanks to you.

This work would not have been possible without Joan Martorell and Felipe Isaule, with who I collaborated almost throughout the thesis. The weekly discussions and meetings were especially useful and enriching for me. Thank you for helping me to improve the thesis as well as other manuscripts. You have become an important part of my Ph.D. and my career.

I want to thank Nikolaj Zinner and Tobias Grass, who received me for three months each in Aarhus and Donostia respectively. These stays helped me to develop my research career, by working and collaborating with more people and opening the scope of my research. Collaborating with yours has been especially interesting and, of course, enriching for me.

An important part of scientific research is collaboration, and I had the luck to have amazing collaborators such as Arnau Rios, Ayaka Usui, Alan Santos, and Francesc Sabater with whom I discussed largely and helped me to improve my knowledge. I also want to thank the rest of my collaborators, James Keeble, Mehdi Drissi, James Schloss, Utso Bhattacharya, and Grigori Astrakharchik. It was a pleasure collaborating with you.

Everybody knows that the Thesis can be stressful, but I want to thank my office colleagues, Maria Arazo, Carlos Ramos, Héctor Briongos, and Eric Sanchez for liven up the days. You helped me, not only with physics discussions but also by having good moments and enjoyable days.

However, to arrive here it was necessary to take previous steps. In a special position, I want to thank Artur Polls, who co-supervised with Bruno Juliá my master thesis.

I learned a lot about physics with Artur, who was an excellent teacher, but the most important thing I will remember is how a good and wonderful person was. I also want to thank Àngels Ramos for supervising my final degree project, probably the first research project I have done.

També voldria agrair al professors que em van iniciar en la física, Tomàs Agulló i Núria Sala, per a introduir-me en el món de la física i ajudar a adonar-me a que em volia dedicar. Gracies a vosaltres he arribat fins aquí.

Per suposat, moltes gràcies als amics que m'han fet suport durant tots els anys, Oriol Roqué, Enric Sarlé, Oriol Falip, Aleix Solernou, Moises Olmedo i Oriol Gasulla per estar sempre a prop quan fa falta. Gràcies a vosaltres els moments durs han sigut més amens i faltaria dir, que seria la vida sense amics!

I sobretot, moltíssimes gràcies a tota la família. Pare, mare, moltíssimes gràcies per tot el suport durant tota la vida i tot l'esforç per a donar-me la millor educació possible. Gràcies a això he pogut arribar fins aquí. Els esforços han valgut la pena. Eva, gràcies per formar part de la meva vida. Estic agraït de tenir una germana com tu, amb qui sé que podré comptar-hi sempre. Avia, moltes gràcies pel teu amor i carinyo, sempre et porto al cor. Abuela, muchas gracias por tu apoyo incondicional, ya sabes que siempre te tengo presente. I no m'oblido de la resta de vosaltres, però si he d'anar un per un no acabaria mai. Espero que us serveixi amb un: moltes gràcies a tots per formar part de la meva vida.

This Thesis has been supported by the grant PREDOCS-UB from Universitat de Barcelona, the grant FPU20/06174 from Ministerio de Ciencia, Innovación y Universidades, and the national projects PID2020-114626GB-I00 from the MICIN/AEI/10.13039/ 501100011033 and PID2023-147475NB-I00 funded by MICIU/AEI/10.13039/501100011033 and FEDER, UE.

1

Introduction

Quantum physics is a fascinating field that began development more than a century ago, see (Kleppner and Jackiw, 2000) for a historical introduction. Even though the field was motivated by quantum effects (Zeilinger, 1999) such as black-body radiation (Planck, 1900) and the photoelectric effect (Einstein, 1905), the theory required decades to be developed. One of the most important results was the Schrödinger equation (Schrödinger, 1926), which gives the time-dependent equation in quantum mechanics. Quantum mechanics results in a very successful theory for describing the microscopic world, allowing us to understand atomic properties and create lasers, for example. Unfortunately, the experimental access to a few particle systems and their manipulation was not possible until the past few decades (Anderson et al., 1995; Kinoshita et al., 2004). Nowadays, it is possible to control quantum systems in ultracold atom laboratories worldwide, see (Lewenstein et al., 2012) for a general overview of the field. In these experiments, it is possible to control the geometry of the system, the traps, the interactions, and the number of particles with incredible precision, see examples in (Bloch et al., 2008; Dalfovo et al., 1999; Giorgini et al., 2008). This new scenario opens the door to exploring fundamental quantum mechanics, where the quantum effects are enhanced in low dimensions and with a few particles (Giamarchi, 2003).

From a theoretical point of view, the study of quantum systems requires solving the Schrödinger equation. In general, it cannot be solved analytically, except for specific potentials and usually for only a single particle or specific circumstances, see for example Deuretzbacher et al. (2008) and Viana-Gomes and Peres (2011). Sometimes the two-particle system can also be solved analytically, for example, if the Hamiltonian can be separated into center-of-mass and relative parts (Busch et al., 1998; Kanjilal and Blume, 2004). Another seminal example is the hydrogen atom. However, when one tries to study a general system with more than two particles, it becomes necessary to use numerical tools to solve the equations. Another option is to use quantum devices to simulate other quantum systems, known as quantum simulators, see examples in Banerjee et al. (2013); Bloch et al. (2012); Dobrzyniecki and Sowiński (2020); Mistakidis et al. (2023); Schäfer et al. (2020).

We focus on realistic setups, using traps and interactions that can be produced experimentally. In addition, we go beyond the most recent experimental advances by studying systems with interactions or levels of control that are not yet achieved in the most recent experiments. See a review of the state of the art of one-dimensional systems in Sowiński and García-March (2019).

In recent decades, the study of ultracold atoms has experienced huge advances since the first realization of a Bose-Einstein Condensate in 1995 (Anderson et al., 1995; Davis et al., 1995). A Bose-Einstein condensate is a phase of matter where all the atoms occupy the same quantum state and behave collectively, forming a macroscopic quantum object. It was predicted by Bose (Bose, 1924) and Einstein (Einstein, 1924) but it took decades to become experimentally feasible. To achieve this, atoms must be cooled below microkelvin temperatures, which requires sophisticated cooling techniques (Phillips, 1998).

Using advances in lasers during the second half of the 20th century, it was possible to engineer laser cooling techniques for atomic gases. Different cooling methods are based on the control using lasers, such as laser cooling, see Vogl and Weitz (2009) for examples, or the evaporation method, see an example in Holland et al. (2000). In addition, it is possible to create a potential due to the effect of counter-propagating lasers, and if one has a periodic structure, then, a lattice structure is created. By controlling the intensity of the trap in each dimension, it is possible to create an effective one-dimensional or two-dimensional system.

Due to the low temperature of the atoms, in the first approximation, the interaction is dominated by the s-wave scattering length. In ultracold atomic gases, one usually models the interaction with a contact delta with an interaction strength that is related to the s-wave scattering length, which can be tuned via Feshbach resonances (Chin et al., 2010) through an external magnetic field.

Ultracold atom experiments are a unique platform to simulate quantum mechanics in a controlled environment (Gross and Bloch, 2017), allowing us to gain insight into small quantum systems, and quantum collective phenomena. The advances produced in the control of these experiments open the door to theoretical exploration, physics prediction, and crosschecking of the experiments.

In this Thesis, we are interested in studying quantum systems with a few particles. Moreover, we restrict our study to low dimensions, where the quantum effects are enhanced (Giamarchi, 2003). We investigate how the interactions affect the systems, which correlations are created, and describe the resulting phase transitions.

Even though our systems may appear simple, they can be challenging to describe, as they are impossible to solve analytically, and the numerical procedures involve complex calculations. The motivation for studying systems with a few particles is based

on the possibility of creating and controlling experimental systems with these specific conditions in ultracold atom laboratories.

Along the Thesis, we expose several topics and systems with a few particles, where the interactions are of paramount importance. We organize the Thesis by placing the different publications on which we base the Thesis in different Chapters. In particular, here we present a summary of the topics explained in each Chapter.

The Chapter 2 includes the results presented in Rojo-Francàs et al. (2022) while providing additional explanations and introductions. In this Chapter, we present an introduction to quantum mechanics by explaining the second quantization formalism, and some aspects of the time evolution. In addition, we present the Hamiltonians we use in the rest of the Thesis: the harmonic oscillator and the Hubbard model. Then, after presenting the different numerical techniques, we explain a method to correct the exact diagonalization calculations with harmonic confinement. We detail the way the correction formula is obtained, and we show that even though it is derived from the exact result of a two-particle system, it is also useful to correct the results for a larger number of particles, as well as to correct the density.

The Chapter 3 includes the results presented in Rojo-Francàs et al. (2024a) and presents new original results. This Chapter explores systems trapped in a harmonic oscillator potential with contact interaction. First, we explain the symmetric case, where all the particles interact with the same strength, known as $SU(N)$. There, we explore the energy spectrum and the ground state density as a function of the interaction strength for different amounts of particles. Then, we explore systems with broken symmetry by vanishing interactions between some pairs of particles. There, we study the structure of the ground state by analyzing the density and the pair correlation function in the large interacting limit. We also explore the energy spectrum as a function of the interaction strength when transitioning from one structure to another. Finally, we explore the case of a single impurity in the system, also known as the polaron problem (Grusdt et al., 2024). In this situation, we study this system by computing the low-energy spectrum and the density as a function of the interaction strength. We use support methods, a mean-field approach, and an ansatz in the infinite interacting limit to interpret the system.

The Chapter 4 includes the results presented in Rojo-Francàs et al. (2024c), where we also include new original results. In this Chapter, we explore the properties of a fractal lattice, specifically, we consider the Sierpiński gasket of finite generation. We also consider briefly the Sierpiński carpet to have a more general overview of the effect of fractality on the system. We focus on the transport properties, analyzing the mean square displacement of a single particle. We compare the behavior of a particle in a regular lattice with well-known results. We relate the time-dependent behavior to a static property such as the integrated level spacing. We examine perturbations on the fractal system by introducing a random potential and an interpolation between the fractal and the regular lattice. In addition, we explore the entanglement creation in a

two-particle system and how the interaction affects the entropy production. We consider contact and long-range interactions, and we use two definitions of entanglement entropy, first, by considering bipartite entanglement, and then we compute the entanglement between both particles.

The Chapter 5 includes the results presented in Rojo-Francàs et al. (2024b), where we extended the explanations and included new results. In this Chapter, we present a three-site lattice system where we propose a time-dependent tunneling ratio to use this system as a quantum battery. We use the Spatial Adiabatic Passage protocol (Eckert et al., 2004), originally designed for one particle, and we apply it to systems of a few interacting particles, a situation for which the protocol was not designed. We explore the success of the protocol as a function of the interaction strength, allowing us to interpret and obtain an effective description by using a two-level model. Due to the interactions, the protocol is no longer adiabatic, but we demonstrate that we can achieve the desired results under the appropriate conditions. We also study the occupation of each site and the one-body density matrix eigenvalues as a function of time.

Finally, in Chapter 6, we summarize the results obtained throughout the Thesis, present the main conclusions and discuss possible extensions of our work.

2

Few particle systems and numerical tools

For systems in low dimensions and especially with few particles, correlations play an important role (Zöllner et al., 2006). In these conditions, some techniques used in many-body systems, such as mean-field theory (Dalfovo et al., 1999) are not appropriate. In our case, to take into account the correlations we use exact diagonalization techniques. In broad terms, they consist of diagonalizing numerically the Hamiltonian, previously written as a matrix (Raventós et al., 2017). In this context, it is useful to use the second quantization formalism, allowing us to work with an appropriate basis (Weiße and Fehske, 2008). Using exact diagonalization, we can obtain the energy spectrum as well as the eigenstates of the system, thus we are not restricted to ground state properties as when one uses other numerical techniques, e.g. Monte-Carlo (Luo et al., 2016) or tensor networks (Verstraete et al., 2008). As a consequence, with this technique, we are able to compute ground state properties, excited state properties, and even time evolution (Rojo-Francàs et al., 2020). However, it has an important limitation when we start to enlarge the size of the system. As we increase the number of particles or the single-particle states, the many-body basis increases exponentially, making it impossible to handle (Chrostowski and Sowiński, 2019). This fact limits our systems to a small number of particles and also to a small number of single-particle states, whether they are internal states or lattice sites.

In the case of an infinite single-particle basis, as in principle occurs in most continuous systems, e.g. a harmonic trap, we need to truncate the basis (Płodzień et al., 2018). Truncating the basis implies that the Hamiltonian matrix computed is an approximation, and it does not have the same energies as the complete Hamiltonian. Due to the variational principle, see a derivation in Rosenbrock (1985), the energies obtained when we truncate the basis are an upper bound of the real ones. For this reason, it might be useful to have a way to systematically improve the results. There have been previous proposals to correct the results using exact diagonalization in a harmonic oscillator, such as extrapolating the results (Grining et al., 2015a), using well-known behavior of the system (Ernst et al., 2011; Jeszenszki et al., 2018), or using an effective interaction (Rammelmüller et al., 2023; Rotureau, 2013). We developed a method that renormalizes the interaction using the analytical solution of the two-particle system (Rojo-Francàs et al., 2022).

In this Chapter, we focus on presenting the technical concepts as well as numerical techniques used in the thesis. In Section 2.1, we introduce the second quantization formalism, including the representation of the operators in that formalism. Then, in Section 2.3, we explain how we managed to do the time evolution. In Section 2.4, we introduce the different Hamiltonians used in the thesis, with the corresponding definitions. In Section 2.5, we present a method to improve the results obtained for the few-particle harmonic potential, explaining the method and including calculations to benchmark its validity. Finally, in Section 2.6, we summarize the contents and present the conclusions of the Chapter.

2.1 Second quantization formalism

In this thesis, we have extensively used the second quantization formalism. The second quantization is useful in the context of many particles, providing a compact convenient description of systems and their Hamiltonians when one considers the statistics of the particles, such as the symmetry of identical bosons or the antisymmetry of the fermions.

This formalism makes use of the Fock states to describe the system. Fock states include information on which states are populated and what the occupation of each state is. For this reason, it is fundamental to choose an appropriate single-particle basis when one works in second quantization. One clear example appears when working in a lattice system, where a good choice is to have the occupation of the lattice sites as basis states. Even though it is still possible to choose states of circulation (or other states) as a single-particle basis, the best choice depends on the system and the calculations that one wants to do.

2.1.1 Fock states

The standard representation of a Fock state is given by

$$|\Phi\rangle = |n_0, n_1, ..., n_M\rangle \,, \tag{2.1}$$

where n_i is the occupation of the single-particle state i. These occupation numbers indicate the number of particles that populate a quantum single-particle state, which are integer numbers. So, a Fock state is an eigenvector of the total number of particles operator with eigenvalue given by $N = \sum_{i=0}^{M} n_i$. The way that one can modify the Fock states is via the creation $\hat{a}_i^\dagger$ and annihilation $\hat{a}_i$ operators. These operators create and destroy a particle in the single-particle state i, respectively. The benefit of this formalism relies on this point because the creation and annihilation operators include the statistics of the particles. In addition, the number operator is defined as $\hat{n}_i = \hat{a}_i^\dagger \hat{a}_i$ and counts the occupation of the single-particle state i. For the specific case of dealing with bosons, we use b_i and $b_i^\dagger$, for fermions c_i and $c_i^\dagger$, and for the general case a_i and $a_i^\dagger$.

For the bosonic case, we use the bosonic operators $\hat{b}_i$ and $\hat{b}_i^\dagger$; and these operators commute as

$$\left[\hat{b}_i^\dagger, \hat{b}_j^\dagger\right] = \left[\hat{b}_i, \hat{b}_j\right] = 0\,, \quad \left[\hat{b}_i, \hat{b}_j^\dagger\right] = \delta_{i,j}\,, \tag{2.2}$$

where $\delta_{i,j}$ is the Kronecker delta. In addition, when these operators act on a Fock state, they act like

$$\hat{b}_i^\dagger|n_0, \ldots, n_i, \ldots, n_M\rangle = \sqrt{n_i + 1}|n_0, \ldots, n_i + 1, \ldots, n_M\rangle \tag{2.3}$$

$$\hat{b}_i|n_0, \ldots, n_i, \ldots, n_M\rangle = \sqrt{n_i}|n_0, \ldots, n_i - 1, \ldots, n_M\rangle\,. \tag{2.4}$$

For bosons, there are no restrictions on how many particles can occupy a quantum state, making it possible to have all the particles in the same single-particle state.

On the other hand, for fermions, the fermionic creation $\hat{c}_i^\dagger$ and annihilation $\hat{c}_i$ operators anti-commute

$$\left\{\hat{c}_i^\dagger, \hat{c}_j^\dagger\right\} = \{\hat{c}_i, \hat{c}_j\} = 0\,, \quad \left\{\hat{c}_i, \hat{c}_j^\dagger\right\} = \delta_{i,j}\,, \tag{2.5}$$

which induces the antisymmetry of the wavefunction. The action of the fermionic operators on a Fock state reads,

$$\hat{c}_i^\dagger|n_0, \ldots, n_i, \ldots, n_M\rangle = (-1)^\phi\sqrt{1 - n_i}|n_0, \ldots, n_i + 1, \ldots, n_M\rangle \tag{2.6}$$

$$\hat{c}_i|n_0, \ldots, n_i, \ldots, n_M\rangle = (-1)^\phi\sqrt{n_i}|n_0, \ldots, n_i - 1, \ldots, n_M\rangle\,. \tag{2.7}$$

where $\phi \equiv \sum_{k=0}^{i-1} n_k$ counts the sum of the occupation numbers of the single-particle states with a lower index than the operator index. Due to the Pauli exclusion principle, a quantum state can only have a maximum of one fermion. For this reason, the occupations for fermions can only be 0 or 1.

From now on, we use $\hat{a}^\dagger$ and $\hat{a}$ for creation and annihilation operators, indicating that they are valid for a general case, or the one that we specify in each case.

In the second quantization, the operators can be described in terms of the creation and annihilation operators. The one-body operators, e.g., kinetic or potential energy, and single-site energy (among others), are written by

$$\hat{U} = \sum_{i,j} u_{i,j}\hat{a}_i^\dagger\hat{a}_j\,, \tag{2.8}$$

where the matrix elements of the interaction are defined as

$$u_{i,j} = \int \Phi_i^*(x)U(x)\Phi_j(x)dx\,. \tag{2.9}$$

$\Phi_i(x)$ is the single-particle wavefunction in the space representation of the quantum state i, and $U(x)$ is the operator in the first quantization.

The two-body operators, e.g., contact interaction, long-range interaction, and so on, are described as

$$\hat{V} = \frac{1}{2} \sum_{i,j,k,l} v_{ij,kl} \hat{a}_i^\dagger \hat{a}_j^\dagger \hat{a}_l \hat{a}_k \,, \tag{2.10}$$

where we need the $\frac{1}{2}$ factor to avoid double-counting, and the matrix elements are defined as

$$v_{ij,kl} = \int \Phi_i^*(x_1) \Phi_j^*(x_2) V\left(x_1, x_2\right) \Phi_k(x_1) \Phi_l(x_2) dx_1 dx_2 \,. \tag{2.11}$$

Note the importance of the ordering of the indices in Eq. (2.10).

Knowing how the operators act on a Fock state, we can descrive the system using the second quantization formalism. The Hilbert space of our system depends on the number of single-particle quantum states, the number of particles, and their statistics. The many-body basis is by using all the different Fock states that can be created. Of course, to have a finite many-body basis states, we need a finite number of particles and a finite number of single-particle states. If the particles are not finite or there are infinite single-particle states, then the many-body basis becomes infinite. In this case, in order to compute numerically properties of the system, one need to truncate the many-body basis with an appropriate criteria. However, truncate the basis results in an approximate Hamiltonian, and the results obtained are not the exact ones.

With the many-body basis, it is possible to write the Hamiltonian in a matrix representation, allowing us to diagonalize it and obtain its eigenvalues and eigenvectors, corresponding to the energies and eigenstates of the system. Of course, with this information, one is able to compute any observable, such as density, correlations, and time evolution.

2.2 Exact diagonalization method

When the analytical approach is not possible, as the equations cannot be solved with a known function, then one must use a numerical approach. Different techniques are used in quantum mechanics, such as exact diagonalization (Deuretzbacher et al., 2007; Raventós et al., 2017), mean-field approaches (Dalfovo et al., 1999), Monte Carlo (Rammelmüller et al., 2017), tensor networks (Krcmar et al., 2018), Density Matrix Renormalization Group (DMRG) (Bellotti et al., 2017), multi-configuration time-dependent Hartree (Meyer et al., 1990), neural networks (Carleo and Troyer, 2017), machine learning (Keeble et al., 2023), coupled-cluster method (Grining et al., 2015b), analytical approaches by using the Bethe ansatz (Bethe, 1931), among others, where each one has its benefits and limitations.

We use the exact diagonalization method, which consists of diagonalizing the matrix Hamiltonian obtaining the exact eigenvalues and eigenvectors of the matrix, with an error in the order of the machine precision, in almost any case, is negligible. Thus,

this method requires writing the Hamiltonian in matrix representation, requiring the use of a discretized basis. This implies that, for example, in the case of lattice systems, it is direct to write the Hamiltonian in matrix form, while for continuous systems, such as the harmonic oscillator, some approximations are needed, for example by discretizing the space, or using second quantization, which is more useful when one deals with more than one particle compared with the space discretization.

To perform the numerical diagonalization, one can obtain all the eigenvalues, i.e., all the energy spectrum and eigenstates, but this is only feasible if the Hilbert dimension is relatively small. When one deals with a large system it is extremely time-consuming to obtain the complete spectrum, and in most cases, it is not necessary if we are not interested in large excitations. Thus, it is common to use an algorithm to obtain the low-energy spectrum, yielding the eigenvalues with the same precision, and it is much faster than obtaining all the states. At the same time, in the systems we are analyzing, the majority of the Hamiltonian matrix elements are zero, implying that the matrices can be treated as sparse, which reduces RAM usage as well as diagonalization time.

The most common algorithm used to diagonalize the low-energy spectrum is ARPACK (Lehoucq et al., 1998), implemented in FORTRAN, and it is used in the built-in eigensolvers of high-level coding languages, for example in Python and Julia. The ARPACK procedure is based on the Lanczos method, which consists of the iterative multiplication of the matrix and a vector by using a random state as the initial vector that has a non-zero overlap with the state with more energy. On each iteration, each component is multiplied with its corresponding energy, and after normalization, the state increases its overlap with the larger energy state. By including convergence criteria, such as the variation of the state or the expected value of the state energy, the method ends with the largest energy eigenstate. Of course, it can be adapted to drive the state to the lowest energy state instead of the largest, being more interesting for our purpose. See variant of the method described with more detail in Wu and Simon (2000).

The exact diagonalization method has some limitations, especially regarding the size of the system. As the dimensions of the Hilbert space grow exponentially with the number of particles and the single-particle basis states, it results in an extremely large many-body basis for a large number of particles and a single-particle basis states. Creating the matrix Hamiltonian, or at least a function that returns the effect of the Hamiltonian operator on a state can require substantial memory and time to be efficient or even feasible. In these situations, other numerical methods are more practical, such as DMRG or, in continuum space with a significant number of particles the Monte Carlo method is a good option. But for relatively small systems, with exact diagonalization, we have access to the excited states, unlike these other methods. With the energy spectrum and the excited states, it is possible to compute time evolution, representing an advantage over other methods. In addition, if we deal with finite single-particle basis systems, as lattices, we ensure that our results are exact, with a negligible error.

2.3 Dynamics in quantum mechanics

Eve thought the study of the static properties of quantum systems is inherently interesting, it is also important to consider the dynamics. The time evolution can be induced, for example, if the system is prepared in a non-eigenstate of the system, or if the Hamiltonian is time-dependent. In these cases, the properties of the system change over time, and so, the observables also depend on the time of measurement.

2.3.1 Representations in quantum mechanics

In quantum mechanics, there are several pictures, namely the Schrödinger, Heisenberg, and Interaction pictures, depending on how the evolution of the system is performed. The first one, the Schrödinger representation, considers that the object that changes with time is the wavefunction, whereas the operators remain constant in time. On the other hand, the Heisenberg representation considers that the wavefunction is not affected by the time evolution, but the operators change with time. Of course, both representations give the same values of the observables, and it does not matter which one you use because they yield the same predictions. Most of the time, one uses the representation in which the calculations become simpler. The third representation, the Interaction one, behaves as an intermediate point between the other two.

The Schrödinger representation considers the operators as time-independent and constant, with all the time evolution information encoded in the wavefunction. The state evolves following the Schrödinger equation,

$$i\hbar\frac{\partial}{\partial t}|\Psi_S(t)\rangle = H|\Psi_S(t)\rangle\,. \tag{2.12}$$

In the case where the Hamiltonian is time independent, we can write the state

$$|\Psi_S(t)\rangle = \mathrm{e}^{-iHt/\hbar}|\Psi_S(0)\rangle\,. \tag{2.13}$$

On the other hand, the Heisenberg representation keeps the state time-independent, implying that the time evolution is encoded in the observables. However, the expectation values of the observables must be independent on the representation we consider,

$$\langle\Psi_S(t)|\hat{O}_S|\Psi_S(t)\rangle = \langle\Psi_H|\hat{O}_H(t)|\Psi_H\rangle\,, \tag{2.14}$$

considering $|\Psi_H\rangle = |\Psi_S(0)\rangle$,

$$\begin{aligned}\langle\Psi_S(t)|\hat{O}_S|\Psi_S(t)\rangle =& \langle\Psi_S(0)|\mathrm{e}^{iHt/\hbar}\hat{O}_S\mathrm{e}^{-iHt/\hbar}|\Psi_S(0)\rangle \\ =& \langle\Psi_H|\mathrm{e}^{iHt/\hbar}\hat{O}_S\mathrm{e}^{-iHt/\hbar}|\Psi_H\rangle\,.\end{aligned} \tag{2.15}$$

Obtaining the operators in the Heisenberg representation as a function of the operators in the Schrödinger representation,

$$\hat{O}_H(t) = \mathrm{e}^{iHt/\hbar}\hat{O}_s\mathrm{e}^{-iHt/\hbar}\,. \tag{2.16}$$

Finally, in the Interaction representation, the state and the operators evolve with time. This representation has parts of both previous representations but requires a two-part Hamiltonian: $\hat{H} = \hat{H}_0 + \hat{H}_1$. Now, we apply the transformation

$$|\Psi_I(t)\rangle = \mathrm{e}^{iH_0t/\hbar}|\Psi_S(t)\rangle\,. \tag{2.17}$$

Note that in the interaction representation, we use a part of the original Hamiltonian in the transformation. In the case of the Heisenberg representation, we also use a similar transformation, but we use the complete Hamiltonian. Using the same arguments as in the previous case, we obtain the expression for the operators in the interaction representation

$$\hat{O}_I = \mathrm{e}^{iH_0t/\hbar}\hat{O}_S\mathrm{e}^{-iH_0t/\hbar}\,. \tag{2.18}$$

It can be proven using the relations we have obtained previously that the evolution of the wavefunction in this representation is

$$i\hbar\frac{\partial}{\partial t}|\Psi_I(t)\rangle = \hat{H}_{1\,I}|\Psi_I(t)\rangle\,, \tag{2.19}$$

where $\hat{H}_{1\,I}$ is the Hamiltonian $\hat{H}_1$ in the interaction representation.

Assuming that our Hamiltonian has the following structure, similar as the system proposed in Chapter 5,

$$\hat{H} = \sum \epsilon_i\hat{a}_i^\dagger\hat{a}_i + \hat{H}_1\,, \tag{2.20}$$

where the first term is treated as the $\hat{H}_0$ part. In that case, using the interaction representation, the creation and annihilation operators are modified as

$$\hat{a}_{i\,I} = \mathrm{e}^{i\hat{H}_0t/\hbar}\hat{a}_i\mathrm{e}^{-i\hat{H}_0t/\hbar}\,. \tag{2.21}$$

It can be demonstrated that, by expanding the expressions and applying the commutation (or anticommutation) relations for bosons (fermions), we obtain

$$\hat{a}_{i\,I} = \hat{a}_i\mathrm{e}^{-i\epsilon_it/\hbar}\,, \tag{2.22}$$

and

$$\hat{a}_{i\,I}^\dagger = \hat{a}_i^\dagger\mathrm{e}^{i\epsilon_it/\hbar}\,. \tag{2.23}$$

2.3.2 Numerical time evolution techniques

To study the dynamical properties of a system, the most straightforward approach is to obtain the time evolution of the system and then evaluate the expectation values of the desired observables. Nevertheless, there are other ways to access dynamical information of the system, for example, sum rules (Bohigas et al., 1979) can be used to derive some dynamical properties using only the ground state of the system.

In the scope of this thesis, the dynamical properties are obtained through the time evolution of the system, and thus, by solving the time-dependent Schrödinger equation

$$i\hbar\frac{d|\Psi\rangle}{dt} = \hat{H}|\Psi\rangle\,, \tag{2.24}$$

where in general, the Hamiltonian $\hat{H}$ can depend on time. In the case of a time-independent Hamiltonian, if the initial state is an eigenstate of the system, the state does not evolve, except for a global phase. This implies that the dynamical properties arise when the system begins in a non-eigenstate of the Hamiltonian.

Technically, we solve the time-dependent Schrödinger equation Eq. (2.24) numerically with standard methods. We can distinguish two possibilities: one where the Hamiltonian is time independent, and another where the Hamiltonian depends on time. The first case is the simplest one, both numerically and conceptually. One standard way to solve these situations is simply to expand the initial state on the eigenstate basis and then the state evolves with each coefficient gaining its respective phase. So, the time-evolved state is

$$|\Psi(t)\rangle = \sum_i c_i(0)\mathrm{e}^{-iE_it/\hbar}|\phi_i\rangle\,, \tag{2.25}$$

where $|\phi_i\rangle$ is the i-th eigenstate, E_i is its corresponding energy, and $c_i(0)$ is the projection of the initial state onto the eigenstate $|\phi_i\rangle$ at $t = 0$. This time-evolution method gives exact results for any time, but it requires the entire diagonalized basis including the energies and eigenstates. Of course, for systems with an infinite number of states, such as the harmonic oscillator, this method cannot be applied exactly and must be truncated, which prevents obtaining an exact solution. Another limitation is that this method only works when the Hamiltonian is static, and in some situations, this is not the case. Then, to solve Eq. (2.24) we need to adapt our tools and use another numerical approach. In our case, as the systems we deal with in these situations are on the order of a few tens of basis states, it is possible to compute $|\Psi(t)\rangle$ using matrix exponentiation. This method is based on time discretization and solving the differential equation recursively,

$$|\Psi(t+\delta t)\rangle = \mathrm{e}^{-iH(t)\delta t}|\Psi(t)\rangle + \mathcal{O}(\delta t^{\alpha})\,, \tag{2.26}$$

where δt is the time step and α is an exponent that depends on the time dependence of the Hamiltonian. Unlike the previous case, here there is an error due to the discretization of the time in each step. So, for a long time, there is an error accumulated in each step, and it is necessary to ensure that the results have converged to mitigate this type of error. The precision of this method goes as δt^{α}, indicating that, if one wants to improve the precision must decrease the value of the time step. A valid convergence criterion can be as simple as computing the time evolution for a second smaller δt and computing the disagreement between both calculations.

2.4 System Hamiltonians considered in the thesis

In this thesis, we explore several systems, all of them related to the topic of a few interacting particles, but in fact, with different geometries, types of interaction, and also distinct particle statistics.

In this Section we introduce and summarize the different Hamiltonians used, even though they are also introduced in their respective Chapters.

2.4.1 Hubbard model

The Hubbard model was introduced in the 1960s to describe the motion of electrons in the solid state (Hubbard, 1963). After that, the Bose Hubbard model was introduced to deal with bosonic systems. Even thought the model appears as an approximation of more complicated systems, in ultracold atoms laboratories it is possible to create lattice systems, where the Hubbard model becomes the exact Hamiltonian of the systems. In this context, the study of the model becomes interesting because of the experimental realizations.The system is widely studied, where there are identified the Mott and the superfluid phases (de Hond et al., 2022).

The model assumes the particles are localized in sites, as in a lattice, with a certain probability of tunneling between nearest-neighbor sites. This tunneling is related to the kinetic energy in the continuum limit. Additionally, it includes an interaction modeled by an on-site potential, adding energy for each pair of particles occupying the same site. The Hamiltonian of this model is usually expressed in the second quantization formalism, for identical bosons

$$\hat{H} = -J \sum_i \left(\hat{a}_i^\dagger \hat{a}_{i+1} + \text{H.c.} \right) + \frac{1}{2} U \sum_i \hat{n}_i (\hat{n}_i - 1) \,, \tag{2.27}$$

and for two-component fermions,

$$\hat{H} = -J \sum_i \left(\hat{a}_i^\dagger \hat{a}_{i+1} + \text{H.c.} \right) + \frac{1}{2} U \sum_i \hat{n}_{i,\uparrow} \hat{n}_{i,\downarrow} \,, \tag{2.28}$$

where J is the tunneling ratio between nearest-neighbor sites and U is the on-site interaction strength. For bosons, the interaction counts the pairs of identical particles in the same site, and for two-component fermions, the interaction counts the pairs of different component in the same site. In this formulation, this Hamiltonian is written in one dimension. In addition, there are two possibilities: having open boundary conditions, where the first and the last sites are only connected to the second and the second-to-last, respectively. The other possibility is to have periodic boundary conditions, where the first and the last sites are connected to each other, apart from the rest of the connections.

We deal with this Hamiltonian in Chapter 4, where we generalize this one-dimensional

Hamiltonian to a two-dimensional one, but with a singular geometry, creating an effective fractal system.

Technically, this Hamiltonian is straightforward to implement in a system with a finite number of sites and also a fixed number of particles. A good single-particle basis is to choose the site occupations, and then, the many-body basis is created with all the combinations. The dimension of the Hilbert space of a lattice with M sites and N identical bosons, D_b, can be computed, as well as the corresponding case of N identical fermions, D_f, as

$$D_b = \frac{(M+N-1)!}{N!(M-1)!} \quad D_f = \frac{M!}{N!(M-N)!}\,. \tag{2.29}$$

If one has a multi-component system, the total Hilbert space can be computed by the tensor product of the Hilbert space of each component in the total number of sites.

The physics we study with this system are dynamics governed by a time-independent Hamiltonian. This allows us to use the exponentiation of the matrix which requires all the energies and eigenstates of the system. This implies that we can deal with systems for which we can diagonalize the entire spectrum. With our resources, we can deal with systems with a Hilbert space of up to a few hundred thousand many-body states, e.g., 10 bosons in 12 single-particle states or 10 fermions in 21 single-particle states.

2.4.2 Three states with time-dependent coupling

In Chapter 5 we introduce a variation of the model a three-site lattice with open boundary conditions. In addition, we added on-site single-particle energy terms, and we modified the tunneling to have a time-dependent tunneling ratio.

With these modifications, one can reproduce the Spatial Adiabatic Passage (SAP) protocol, or if it is treated as internal levels instead of lattice well, it can correspond to the Stimulated Raman Adiabatic Passage (STIRAP) protocol. In Chapter 5 we use this protocol to implement a quantum battery and study the charge as a function of parameters such as the interaction strength and coupling strength.

The Hamiltonian that models this situation reads

$$\hat{H} = \sum_{i=1}^{3} \hat{n}_i \epsilon_i + \left(\Omega_{12}(t)\hat{a}_1^\dagger \hat{a}_2 + \Omega_{23}(t)\hat{a}_2^\dagger \hat{a}_3 + \text{H.c.}\right) + \frac{1}{2}U \sum_{i=1}^{3} \hat{n}_i(\hat{n}_i - 1)\,. \tag{2.30}$$

In our case, we decided to have the level energies ordered, as if the system is tilted, and for convenience, we chose $\epsilon_1 = 0$. In addition, we deal with systems of indistinguishable bosons.

Technically, this system is relatively easy to simulate, as the Hilbert space for N bosons is

$$D_b = \frac{(N+2)!}{N!2!} = \frac{(N+2)(N+1)}{2}\,, \tag{2.31}$$

so, the system scales as the square of the number of particles. In that sense, one can argue that it is easy to compute up to a relatively large number of particles, as the dimension of the system remains at a reasonable value. However, in that case, the Hamiltonian is time-dependent, implying the need to use a more resource-consuming method. It is still necessary to diagonalize the whole Hamiltonian to compute the matrix exponential at each time step. Although it is possible to do this for systems with dimensions up to a few thousand, it could take too much time; realistically, it is better to keep smaller systems below a hundred Hilbert dimensions.

2.4.3 Harmonic confinement

In Chapter 3, we study systems with few particles and the effects of the interaction on the system. A realistic platform to study these systems is ultracold atoms, where a common trap can be approximated as a harmonic potential confinement. For this reason, we decided to study these particular systems: a few particles trapped in a harmonic potential with a realistic interaction modeled by a contact potential. As example of studies with these conditions, see Budewig et al. (2019); Pęcak et al. (2017); Pyzh et al. (2018); Sowiński et al. (2010).

The Hamiltonian of this system includes the kinetic energy, the potential energy, both one-body operators and the contact potential, which is a two-body term. In the first quantization, the contact interaction is approximated by a delta function, resulting in

$$H = \sum_{i}^{N} \left(-\frac{\hbar^2}{2m}\frac{\partial^2}{\partial x_i^2} + \frac{m\omega^2}{2}x_i^2 \right) + \sum_{i<k} g_{i,k}\delta(x_i - x_k)\,, \tag{2.32}$$

where $g_{i,k}$ is the strength of the contact interaction between the particles i and k, and we have assumed that all the particles have the same mass m and the external confinement has the same frequency ω, however, the interaction can be different between each pair of particles. This can make sense if we deal with distinguishable particles, or if we have different species.

We can use the second quantization formalism, where the Hamiltonian is written independently of the nature of the particles. In that case, we use as single-particle basis the eigenfunctions of the single-particle harmonic oscillator wavefunctions $\varphi_i(x)$ with energy $\epsilon_n = \hbar\omega(n + \frac{1}{2})$. The Hamiltonian reads

$$\hat{H} = \sum_{i} \epsilon_i \hat{n}_i + \frac{1}{2}\sum_{i,j,k,l} g_{\alpha,\beta} v_{ij,kl} \hat{a}_i^\dagger \hat{a}_j^\dagger \hat{a}_l \hat{a}_k\,, \tag{2.33}$$

where α and β depend on the species associated with the indices i, k and j, l, respectively. The interaction matrix elements can be obtained analytically (Rojo-Francàs et al., 2020) using Hermite polynomial integrals properties (Titchmarsh, 1948).

In these systems, we do not deal with time evolution, and we only compute static

properties. This allows us to study larger systems because we do not need to diagonalize the entire Hamiltonian. As we are interested in the lower part of the spectrum increases the time of the calculation, because obtain a reduced number of eigenvalues is more efficient than compute all the eigenvalues. Our capabilities allow us to study systems with up to six particles with reasonable precision by using 20 single-particle modes, resulting in 177 100 many-body states, or eight particles with 15 single-particle modes, resulting in 319 770 many-body states.

In contrast to the lattice systems, the single-particle basis is not finite, as there are infinite levels of the harmonic oscillator. Therefore, when we study the harmonic oscillator system we need to truncate our basis, which induces an error in our calculations. The truncation allows us to create the Hamiltonian matrix and diagonalize at least the lower energy part. The truncation is an approximation; thus, the more states we include, the better results we obtain.

Performing this type of calculation, one is largely limited by the number of particles, because a large number of single-particle states are needed to achieve convergence. Thus, one needs to sacrifice precision as the number of particles increases, obtaining reasonable results for fewer than ten particles, with our resources.

2.5 Correction method for the harmonic oscillator

Unfortunately, the single-particle basis is inherently infinite, as a consequence the many-body basis is also infinite. The numerical treatment of this system involves truncating the basis to have a finite many-body basis, but it introduces an error. According to the variational principle, using a larger basis yields better results, and the values obtained correspond to an upper bound of the correct energy (Hill, 1985). Naturally, this issue arises for other systems with an infinite basis.

We want to have the most accurate results possible, so, we aim to reduce the error in the calculations. To achieve this, the first thing one can do is increase the basis, but it has a limit due to the exponential growth of the many-body basis. In addition, as interactions become stronger, more discrepancies appear compared with the exact solution. For this reason, we need an additional method to manage the error. Another strategy is to control the error and develop a way to correct the results. One possibility is to extrapolate the values obtained with an increasing basis to the infinite basis limit. However, the extrapolation is highly sensitive to the fit function used and it needs multiple calculations and a final fitting, adding complexity.

Our approach differs significantly. We develop a correction for the interaction strength using analytical procedures. With this method, we can correct the low-energy spectrum and obtain results that are nearly exact with a single calculation and without relying on a fit.

2.5.1 Renormalization of the interaction

Our goal is to develop a procedure to correct the energies obtained with a truncated basis for a system trapped in a harmonic oscillator. Our approach involves renormalizing the interaction, but this requires an analytical argument.

We apply some ideas proposed in Ernst et al. (2011); Jeszenszki et al. (2018), deriving a correction using the two-body solution.

2.5.1.1 Two-particle case

The case of two particles trapped in a harmonic oscillator with contact interaction is a well-known problem that has an analytical solution (Busch et al., 1998). Here we follow the same procedure as in the original article, which we then use to derive the correction. The truncation method of the single-particle basis naturally arises in this derivation. We also restrict our case to one dimension for simplicity.

The Hamiltonian of two particles in a harmonic oscillator, in first quantization and using the harmonic oscillator units can be derived from Eq. (2.32), being explicitly,

$$H = -\frac{1}{2}\frac{\partial^2}{\partial x_1^2} - \frac{1}{2}\frac{\partial^2}{\partial x_2^2} + \frac{x_1^2}{2} + \frac{x_2^2}{2} + g\,\delta(x_1 - x_2)\,. \tag{2.34}$$

We use the properties that the harmonic potential can be separated into center-of-mass (c.m.) and relative coordinates. Using the modified variables $X_{\text{c.m.}} \equiv (x_1 + x_2)/\sqrt{2}$ and $x \equiv (x_1 - x_2)/\sqrt{2}$ for symmetry reasons, we obtain the Hamiltonian separated into relative and center-of-mass components. The center-of-mass Hamiltonian is a single-particle harmonic oscillator Hamiltonian, with energies $E_{\text{c.m.}} = \hbar\omega(n_{\text{c.m.}} + 1/2)$. So, all the physics we want to solve is contained within the relative coordinate system, where the relative coordinate Schrödinger equation reads

$$\left(H_{\text{HO}} + \frac{g}{\sqrt{2}}\delta(x)\right)\Psi(x) = E_{\text{r}}\Psi(x)\,, \tag{2.35}$$

where H_{HO} is the harmonic oscillator Hamiltonian for the relative coordinate.

To solve the Schrödinger equation, we expand the wavefunction in the eigenstates of the harmonic oscillator $\Phi_m(x)$,

$$\Psi(x) = \sum_m c_m \Phi_m(x)\,, \tag{2.36}$$

applying it to the Schrödinger equation and projecting the state $\Phi_n(x)$,

$$\begin{aligned}&\int \left(\Phi_n(x)\sum_m c_m E_m \Phi_m(x) + \frac{g}{\sqrt{2}}\Phi_n(x)\delta(x)\sum_m c_m \Phi_m(x)\right) dx \\ &= \int \left(\Phi_n(x) E_r \sum_m c_m \Phi_m(x)\right) dx\,,\end{aligned} \tag{2.37}$$

using the orthogonality of the eigenstates $\int \Psi_n(x)\Psi_m(x)dx = \delta_{n,m}$, we obtain

$$c_n(E_n - E_r) + \frac{g}{\sqrt{2}}\Phi_n(0)\sum_m c_m\Phi_m(0) = 0\,, \tag{2.38}$$

and we can obtain the coefficients as,

$$c_n = A\frac{\Phi_n(0)}{E_n - E_{\rm r}}\,, \tag{2.39}$$

where $A = -\frac{g}{\sqrt{2}}\sum c_m\Phi_m(0)$ is a constant.

Using the definition of Eq. (2.39) in Eq. (2.38), we obtain

$$A\frac{\Phi_n(0)}{E_n - E_r}(E_n - E_r) + \frac{g}{\sqrt{2}}\Phi_n(0)\sum_m A\frac{\Phi_m(0)}{E_m - E_r}\Phi_m(0)\,, \tag{2.40}$$

and dividing the entire expression by the common factor $A\Phi_n(0)$, we obtain,

$$1 + \frac{g}{\sqrt{2}}\sum_{n=0}^{\infty}\frac{\Phi_n(0)\Phi_n(0)}{E_n - E_{\rm r}} = 0\,. \tag{2.41}$$

Using the explicit value of the eigenstates of the harmonic oscillator at the center of the trap,

$$\Phi_n(0) = (-1)^{-n/2}\frac{\sqrt{n!}}{\pi^{1/4}\sqrt{2^n}(n/2)!}\,, \tag{2.42}$$

for even n and $\Phi_n(0) = 0$ for odd n. Moreover, the energy of the eigenstates is $E_n = \hbar\omega(n+1/2)$, and for convenience, we define the relative energy as $E_r = \hbar\omega(2\nu+1/2)$. As the only contributions in the sum are the even terms, we make the change $n = 2n'$, and we rewrite Eq. (2.41) with the explicit dependence on n' as

$$-\frac{1}{g} = \sum_{n'=0}^{\infty}\frac{1}{2\sqrt{2\pi}}\frac{(2n')!}{4^{n'}(n'!)^2(n'-\nu)}\,. \tag{2.43}$$

So, we can relate the interaction strength g with a sum of the number of the (even) harmonic oscillator level functions that include the exact energy,

$$-\frac{1}{g} = \sum_{n'=0}^{\infty} f(n',\nu)\,, \tag{2.44}$$

where the function $f(n',\nu)$ is

$$f(n',\nu) = \frac{1}{2\sqrt{2\pi}}\frac{(2n')!}{4^{n'}(n'!)^2(n'-\nu)}\,. \tag{2.45}$$

The sum in Eq. (2.43) can be solved in closed form (Busch et al., 1998), resulting in

$$\frac{\Gamma(-\nu)}{\Gamma(1/2-\nu)} = -\frac{2^{3/2}}{g}\,, \tag{2.46}$$

obtaining an expression that relates the energy of the relative system $E_r = (2\nu + 1/2)$ with the interaction strength g. One can obtain the complete energy of the state by combining it with the center-of-mass energy $E_{\text{c.m.}}$.

Now, with the solution of the two-particle case, we want to relate or find a connection with a truncated calculation. In this situation, a simple truncation of the calculation could consist in using a finite number of terms in the sum of Eq. (2.43). So, if we use M harmonic oscillator modes, we consider only the first $\mathcal{M} = \lfloor (M-1)/2 \rfloor$, where $\lfloor x \rfloor$ is the floor function. Note that the M mode corresponds to the mode $n+1$ and in the sum we made the transformation $n = 2n'$, and only the even n contribute.

The finite sum can be expressed as an analytical expression and would correspond to a truncated calculation; thus, the interaction strength is also a truncated result,

$$\begin{aligned} -\frac{1}{g'} \equiv & \sum_{n'=0}^{\mathcal{M}} f(n', \nu) \\ = & \frac{\Gamma(-\nu)}{2^{3/2}\Gamma\left(\frac{1}{2} - \nu\right)} - \Gamma\left(\mathcal{M} + \frac{3}{2}\right)\Gamma(\mathcal{M} - \nu + 1) \\ & \times \frac{{}_3\tilde{F}_2\left(1, \mathcal{M} + \frac{3}{2}, \mathcal{M} - \nu + 1; \mathcal{M} + 2, \mathcal{M} - \nu + 2; 1\right)}{2\pi\sqrt{2}}, \end{aligned} \tag{2.47}$$

where ${}_3\tilde{F}_2$ is a hypergeometric regularized function. In the limit of the full basis $\mathcal{M} \to \infty$, Eq. (2.47) recovers Eq. (2.46).

The truncated calculation Eq. (2.47) relates the truncated interaction strength g' with the relative energy E_r obtained with this method when using M modes on the relative part. Our goal is to relate this truncated result with the exact one. Instead of correcting the energy value, it is easier to correct the value of the interaction strength associated with a certain energy E_r using this formulation.

For a certain value of the interaction, we can split the sum of Eq. (2.43), into two parts. The first one is up to $\mathcal{M}$ and the second is the rest,

$$-\frac{1}{g(\nu)} = \sum_{n'=0}^{\mathcal{M}} f(n', \nu) + \sum_{n'=\mathcal{M}+1}^{\infty} f(n', \nu)\,. \tag{2.48}$$

Note that the first term on the right-hand side corresponds to the sum in Eq. (2.47) and can be defined as $1/g'$. Analogously, we define an interaction strength correction g_c as $\sum_{n'=\mathcal{M}+1}^{\infty} f(n', \nu) = 1/g_c$. We can express the value of the interaction corresponding to an energy E_r as

$$\frac{1}{g(\nu)} = \frac{1}{g'(\mathcal{M}, \nu)} - \frac{1}{g_c(\mathcal{M}, \nu)}\,, \tag{2.49}$$

that connects the exact interaction strength g for a given energy of the relative system with the truncated value g' at the same energy. This correction equation has a structure

similar to the ones used to regularize two-body interactions in quantum gases (Stoof et al., 2009).

One can obtain the analytical value of the interaction correction g_c for a given number of modes M and energy of the relative system E_r using both Eq. (2.46) and Eq. (2.47),

$$\begin{aligned}\frac{1}{g_c} =&\Gamma\left(\mathcal{M}+\frac{3}{2}\right)\Gamma(\mathcal{M}-\nu+1)\\ &\times\frac{{}_3\tilde{F}_2\left(1,\mathcal{M}+\frac{3}{2},\mathcal{M}-\nu+1;\mathcal{M}+2,\mathcal{M}-\nu+2;1\right)}{2\pi\sqrt{2}}\,,\end{aligned} \tag{2.50}$$

where $\mathcal{M}=\lfloor(M-1)/2\rfloor$ and $\nu=(E_r-1/2)/2$. With this analytical expression, we have the exact dependency on both parameters, namely, the energy and modes used. It can be proved that for a large number of modes, the term $\mathcal{M}$ becomes dominant over ν, indicating that the energy used in the correction has a minor impact. Therefore, we need to control the parameter M and know exactly how we perform our calculations to match this development.

We have obtained a closed expression to correct the truncated results, specifically g_c of Eq. (2.50). However, the numerical evaluation is very time-consuming because of the hypergeometric functions. For this reason, we introduce an approximation that yields sufficiently good results but is faster to compute and can be useful in some situations where the time of calculation matters.

The first step is using the Stirling asymptotic approximation formula in Eq. (2.43), but summing starting from $\mathcal{M}+1$,

$$\begin{aligned}\frac{1}{g_c(\mathcal{M},\nu)} &= \frac{1}{2\sqrt{2\pi}}\sum_{n'=\mathcal{M}+1}^{\infty}\frac{(2n')!}{2^{2n'}(n'!)^2(n'-\nu)}\\ &\simeq \frac{1}{2\sqrt{2\pi}}\sum_{n'=\mathcal{M}+1}^{\infty}\frac{1}{\sqrt{n'\pi}(n'-\nu)}\,.\end{aligned} \tag{2.51}$$

Now, to solve the sum, we transform it to an integral by using the Euler-MacLaurin formula, obtaining

$$\begin{aligned}\frac{2\pi\sqrt{2}}{g_c} \simeq&\frac{1}{\sqrt{\nu}}\ln\left(\frac{\sqrt{\mathcal{M}+1}+\sqrt{\nu}}{\sqrt{\mathcal{M}+1}-\sqrt{\nu}}\right)\\ &+\frac{1}{2\sqrt{\mathcal{M}+1}(\mathcal{M}+1-\nu)}\\ &\times\left(1+\frac{1}{12(\mathcal{M}+1)}+\frac{1}{6(\mathcal{M}+1-\nu)}\right)\,.\end{aligned} \tag{2.52}$$

Using this approximation for g_c we obtain errors of less than a 1% with its exact value of Eq. (2.50) but being up to $\sim 10^6$ times faster to evaluate. To obtain this approximation

that works with the described precision, one needs to ensure $\nu < \mathcal{M}$. Note that all the terms in the sum of Eq. (2.51), are positive if $\mathcal{M} + 1 > \nu$, corresponding to the region where the approximation works. If the energy is too large for the number of modes used it is necessary to include in the formula a term with a negative sign, creating problems when we approximate.

In particular, for $\mathcal{M} + 1 = \nu$ the expressions have a pole. In addition, for larger values of the energy ν, as we mentioned before, the original sum contains negative signs, and as a consequence, the value of the correction g_c obtained with Eq. (2.50) varies from $-\infty$ to ∞, depending on the precise value used. But the approximation of Eq. (2.52) yields imaginary values for the correction g_c. For this reason, one has to ensure that the state that is correcting fulfills the condition $\nu \leq \mathcal{M} + 1$, or translated to energies and modes used, $\Delta E/\hbar\omega \leq M + 1$, where ΔE is the energy difference between the energy E of the state and the non-interacting ground state energy E_0, that depends on the number of particles as $E_0 = N/2\hbar\omega$. These conditions imply that, to correct a state with energy E, one needs to include in the basis all the states with non-interacting energy below or equal to E.

2.5.1.2 Truncation of the many-body basis

Up to now, we developed a method using the two-body problem and reduced it to the relative coordinate Schrödinger equation. But our goal is to translate this correction of a truncation on the relative coordinate modes to a many-body system. A usual truncation on a many-body basis is to use M single-particle modes and consider all the states that can be created with these modes. However, there exists a more efficient truncation method, which does it in the non-interacting many-body energy. In this situation, one only considers the many-body states with a non-interacting energy below a threshold, with a maximum energy $E_{\max}(M)$. This energy truncation allows us to obtain better results compared with the ones with a standard truncation when the many-body basis has a similar Hilbert space. Or, in other words, it allows us to reduce the basis, and so, the complexity of the system without losing precision (Chrostowski and Sowiński, 2019; Płodzień et al., 2018).

There is a relation between the maximum energy and the highest mode M used in the truncation. The optimal value of the maximum energy for a boson system is (Płodzień et al., 2018)

$$E_{\max}(M)/\hbar\omega = M - 1 + N/2\,, \tag{2.53}$$

where N is the number of particles. On the other hand, in fermionic systems with different components, the optimal maximum energy is

$$E_{\max}(M)/\hbar\omega = M + E_F/\hbar\omega - \max\left(N_\alpha\right)\,, \tag{2.54}$$

where E_F is the Fermi energy and N_α is the number of particles in the internal component state α.

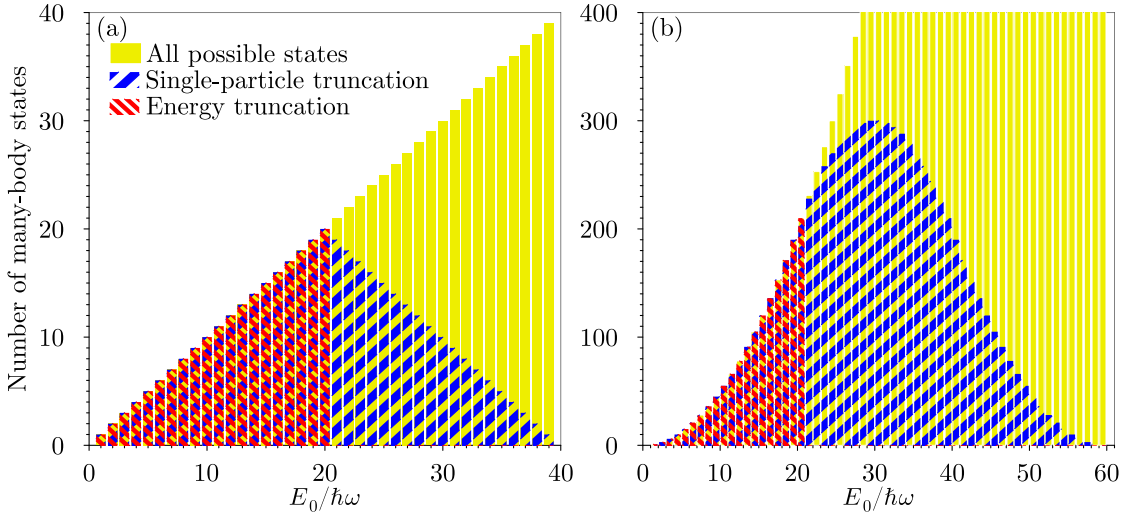

Figure 2.1: Number of basis states for each value of the non-interacting energy. Panel (a) correspond to the case with $N = 2$ and panel (b) to $N = 3$, using 20 single-particle modes for both cases. The yellow solid region represents the number of states with less energy than $E = 40\ \hbar\omega$ and $E = 60\ \hbar\omega$ for two and three particles, respectively. The blue-thick-hatched region represents the number of states that can be created with 20 single-particle states. The red thin-hatched region represents the number of states created with 20 single-particle states and with an energy truncation at $E = E_{\text{max}}$.

Note that this maximum energy for both the bosons and fermions corresponds to the minimum energy one can create populating the mode M once. For bosons, it is basically one particle in the M mode and the rest in the ground state. Whereas for fermions, from the ground state, with Fermi energy, it takes the fermion in the highest mode and moves it to the M one.

In Fig. 2.1 we show the number of the many-body states as a function of their non-interacting energy. There we compare the basis used with a standard truncation, the energy truncation, and the complete system without truncation for two and three particles. Both truncation methods use the same value of M. Note that using the energy truncation, represented by the red thin-hatched region, one uses significantly fewer states in the basis than those corresponding to a standard truncation, represented by the blue thick-hatched region. Note that the energy truncation includes fewer states, but they create a complete basis up to E_{max}. In contrast, the standard truncation includes non-complete many-body basis for energies larger than E_{max}

Having a complete basis up to E_{max}, allows us to change the basis to another equivalent one. So, all the center-of-mass and relative states are included in that complete basis, meaning that, if a system is in the center-of-mass ground state, the energy truncated basis includes the first M relative excitations, as in our analytical truncation developed. This fact means that the energy truncation can be mapped to our correction method. This is not the case for the standard truncation, where there are more states, which

Particles and modes	Standard truncation	Energy truncation
$N = 2$, $M = 20$	400	210
$N = 3$, $M = 20$	8 000	1 540
$N = 3$, $M = 90$	729 000	125 580
$N = 4$, $M = 20$	160 000	8 855
$N = 4$, $M = 45$	4 100 625	194 580
$N = 5$, $M = 20$	3 200 000	42 504
$N = 6$, $M = 20$	64 000 000	177 100

Table 2.1: Many-body Hilbert space corresponding to systems with N distinguishable particles and considering M harmonic oscillator modes. We compare the dimensions of the systems if we use a standard truncation and if we incorporate the energy restriction of Eq. (2.53).

prevents relating the truncation of the many-body basis with a truncation of the relative system.

In Tab. 2.1 we present some examples of how the number of the many-body basis grows with the number of particles and modes and at the same time, compare with the reduction when we use the energy truncation. In that case, for simplicity, the values reported corresponds to N distinguishable particles. As can be observed, as the number of particles increases, the reduction on the many-body basis due to the energy truncation is larger in relative terms. Of course, with the same number of modes, as the number of particles increases, the basis dimension increases exponentially, even in the energy truncation method.

So, having an energy truncated basis, we can create the Hamiltonian matrix corresponding to an interaction strength g', diagonalize it, and obtain the lower part of the energy spectrum. The results follow as we used a truncated basis in analogy with the truncated relative system of Eq. (2.47). So, we can relate the truncated result obtained numerically with the exact value as in Eq. (2.49), using as a correction the value of Eq. (2.50), obtaining the value of the exact interaction strength g for which its energy we obtained using g'.

Even though this procedure is derived from the two-particle case, where it is exact by construction, we are encouraged to use it for a larger number of particles, as the contact potential is a two-body interaction, where most of the physics occurs in the relative wavefunctions of two particles. There is a systematic procedure to correct the result for an arbitrary number of particles and an arbitrary number of components of the system, allowing each pair of components to interact with different strengths.

The first step is to create the many-body basis with the N particles and using M modes of the harmonic oscillator. The many-body basis must be created following the energy restriction, where all the elements of the basis must have an energy less than

or equal to $E_{\max}$ of Eq. (2.53) or Eq. (2.54). According to our discussions at the end of Section 2.5.1.1, with this correction, we can correct states up to an energy $E_{\max}$.

Then, with the many-body basis defined, we can create the Hamiltonian matrix, with interaction strengths $g'_{\alpha,\beta}$, where α and β are the internal components of the system. With the matrix, we can diagonalize it, obtaining the eigenvalues. For each eigenvalue E, we use $\nu = (E/\hbar\omega - N/2)/2$, and compute the correction g_c using Eq. (2.50) or Eq. (2.52) depending on whether we want the extra precision or the time efficiency.

The last step is to correct each interaction strength associated with the state with energy E as $g_{\alpha,\beta} = g'_{\alpha,\beta}/(1 - g'_{\alpha,\beta}/g_c)$, where $g_{\alpha,\beta}$ is the exact value of the interaction between the internal components α and β corresponding to an energy E.

2.5.2 Results for two particles

As a direct example of how the results can be improved using the correction, here we show the results for two particles. In Fig. 2.2 we show the ground state and the first excited state of two particles as a function of the interaction and their correction. We also compare it with the exact analytical energies of Eq. (2.46) We used a small number of modes of the harmonic oscillator to enhance the effect of the correction method. We refer to the energies obtained by diagonalizing the Hamiltonian as the truncated results, whereas the ones obtained using these last ones and the correction, we refer to as the corrected results.

We obtain a perfect agreement between the corrected results and the exact energies for the ground state. With the correction, we obtain the analytical value for the energy in the Tonks limit, $E_\infty = 2\hbar\omega$ at exactly $1/g = 0$. On the other hand, for the truncated results, we obtain this energy at a finite value of the interaction strength. In addition, the truncated calculation shows deviations for any interaction, becoming larger for larger interactions. This method allows correcting, not only the ground state energy but also the excited states with the same precision.

An interesting feature is that, as we mentioned, for the truncated calculations, we reach the energy of the Tonks limit at a finite interaction strength g'_t. This implies that for larger values, $g' > g'_t$, we obtain energies for the ground state above the value it has in the infinite interacting limit (Rojo-Francàs et al., 2022). Once the correction is done, these states go to a large attractive interaction strength and correspond to an excited state of the attractive branch (Ernst et al., 2011). So, it is possible to map the whole repulsive interaction regime $g > 0$ with a finite truncated repulsion $0 < g' < g'_t$. However, it is not possible to map the attractive regime $g < 0$ with a finite range of the truncated interaction strength. One can correct weak interactions using $g' < 0$, and large attractive interactions using $g' > g'_t \gg 0$. But in this last case, this results in obtaining excited states.

Although our correction method is derived from the two-particle energy, we found

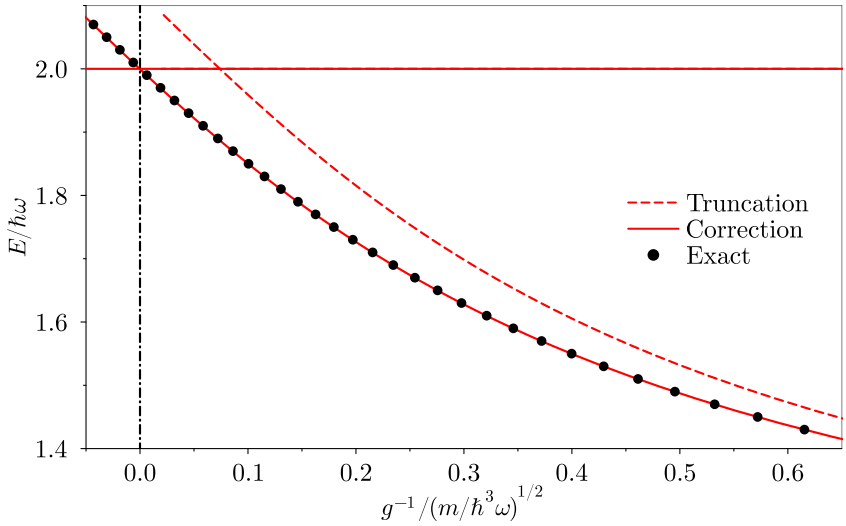

Figure 2.2: Ground state energy of the two-particle system with SU(2) symmetry. The dotted line corresponds to the truncated results obtained with direct diagonalization using a basis of 20 single-particle modes, whereas the solid line corresponds to the corrected results using Eq. (2.52). The black circles correspond to the exact values of Eq. (2.46). The vertical dotted line indicates $1/g = 0$. The horizontal line shows the Tonks energy for two particles.

that it can also correct other properties, such as the density profile. In the same way as the energy, the densities do not change; the correction only acts on the associated interaction strength. In Fig. 2.3, we show the density profile of the ground state of a two-particle system for different values of the interaction strength. We also include a first relative excitation in the large attractive branch. All the values reported for the interaction strength g are the ones corrected, computed with a g' given by Eq. (2.49).

We compare our results with the exact density profiles obtained by integrating the exact wavefunction (Busch et al., 1998)

$$\Psi(x_1, x_2) = Ae^{-(x_1^2+x_2^2)/2} U\left(-\nu, \frac{1}{2}, \frac{1}{2}(x_1 - x_2)^2\right) , \tag{2.55}$$

where A is a normalization constant and $U(a, b, z)$ is the Tricomi confluent hypergeometric function. All the parameters in Eq. (2.55) are in harmonic oscillator units.

We obtained an almost perfect agreement between our numerical calculations by correcting the truncated basis and the exact density profiles. Note that, as we commented before, the method is developed only to correct the energy, but it also can be used to correct the densities. More interestingly, the state in the attractive branch is also well reproduced, but it was computed using a repulsive interaction g'.

In order to have some quantification of how good the agreement between the density

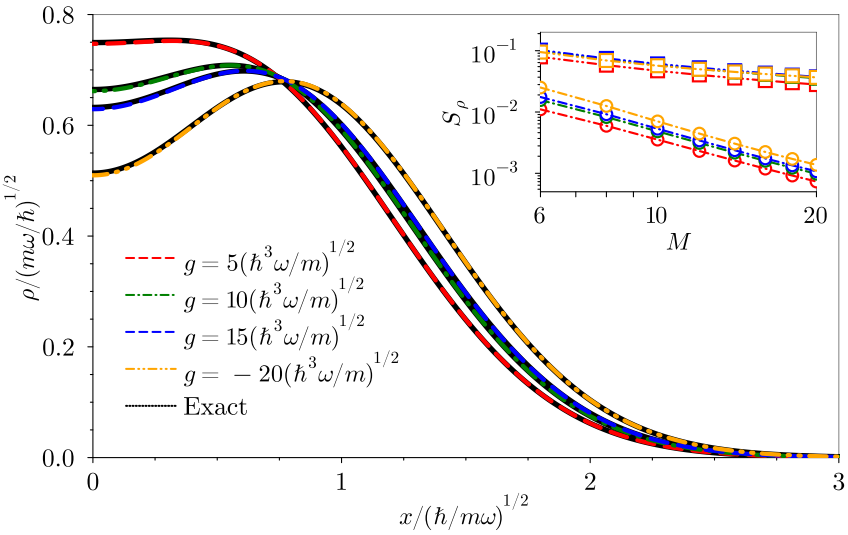

Figure 2.3: Density profiles of two particles for different choices of interaction strengths. The thick lines correspond to profiles obtained with the corrected direct diagonalization calculations with 20 single-particle modes, whereas the black thin lines are exact results given by Eq. (2.55). The inset shows a correlation parameter S_ρ between the exact profiles Eq. (2.55) and the profiles obtained with the truncated diagonalizations (squares with thin lines) and the corrected ones (circles with thick lines) as a function of the number of single-particle modes M.

profile obtained numerically and the exact one, we propose the correlation metric

$$S_\rho(\rho_1, \rho_2) = \frac{\int_{-\infty}^{\infty} |\rho_1(x) - \rho_2(x)| dx}{2N}, \tag{2.56}$$

that computes the difference between two densities, in our case, between the numerical and the exact ones. It is normalized to be in the range $0 \leq S_\rho \leq 1$, being zero when both densities are identical and one when they do not overlap at all. In the inset of Fig. 2.3 we show this parameter for different interaction strengths and different numbers of modes used in the calculation. We find that the corrected densities are not identical to the analytical ones, as we expected. However, as we increase the number of modes, the parameter S_ρ decreases, indicating that the results are more accurate. We also compared the truncated results with the corrected ones, obtaining not only less error in the corrected calculations than in the truncated calculations but also that the error reduction with the number of modes is much faster for the corrected than the truncated results. This indicates that using our correction method, one can correct efficiently the density profile with high accuracy.

2.5.3 Extrapolation to many particles

At this point, we have developed a method to correct the two-particle energy analytically and also demonstrated that the correction procedure can improve the density profile

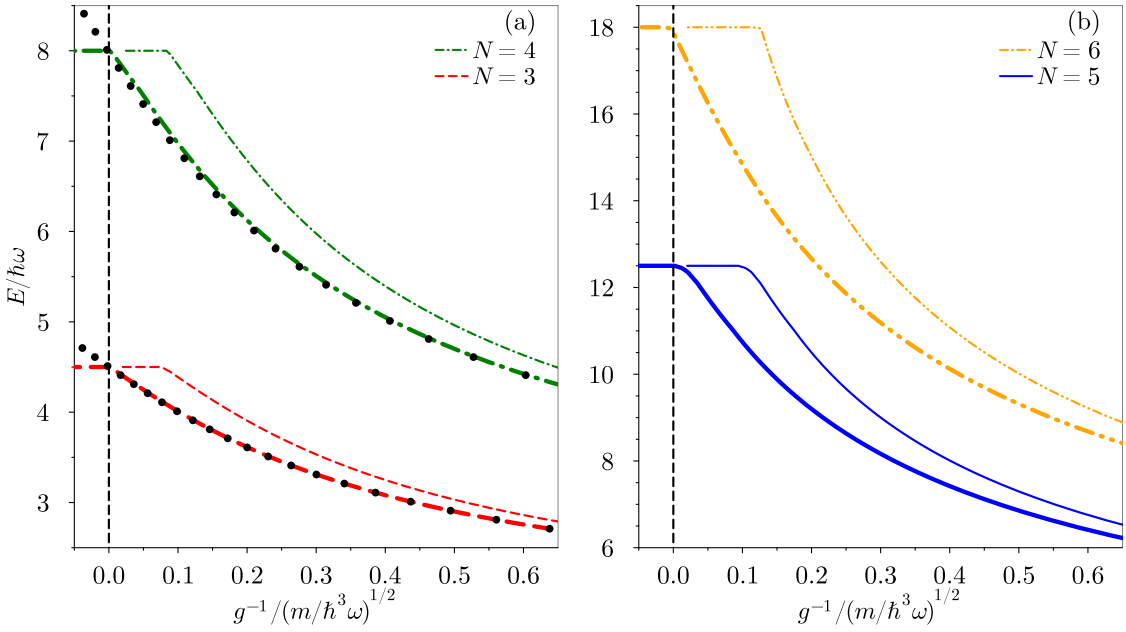

Figure 2.4: Ground state energies for three to six distinguishable particles. Panel (a) includes the results for three and four particles whereas panel (b) includes the five and six particle cases. All the systems are computed using 20 single-particle modes. The thin lines correspond to the truncated calculations, whereas the thick lines correspond to the corrected energies obtained using Eq. (2.52). The black circles correspond to the exact values for $N = 3$ and $N = 4$ (Laird et al., 2017). The horizontal lines correspond to states with the Tonks energy for N particles.

calculations. Although this method is not exact for a larger number of particles, we show that it is still useful, being more efficient and feasible than merely increasing the number of modes. The key point here is that we use the two-particle solution, with a slight modification in the definition of ν, to correct systems with a small number of particles.

In Fig. 2.4 we show the ground state energy as a function of the interaction for $N = 3$, 4, 5, and 6 distinguishable particles. We use a $SU(N)$ system, where all the interactions between the different particles are identical, $g_{\alpha,\beta} = g$. We compare the results obtained numerically with the truncated basis and its correction, noticing an appreciable difference. For $N = 3$ and $N = 4$, we also compare our results with the exact solutions of Laird et al. (2017). In both cases, we find good agreement with our numerical results after applying the correction, and we expect that for larger particles our protocol still works.

For the $SU(N)$ case, there is an analytical solution for the limit of infinite repulsive interaction, known as the Tonks-Girardeau gas. In this limit, the system of N identical bosons (or distinguishable particles) is mapped to N polarized fermions, whose ground state energy is $E_\infty/\hbar\omega = N^2/2$. This solution can be used to crosscheck our numerical

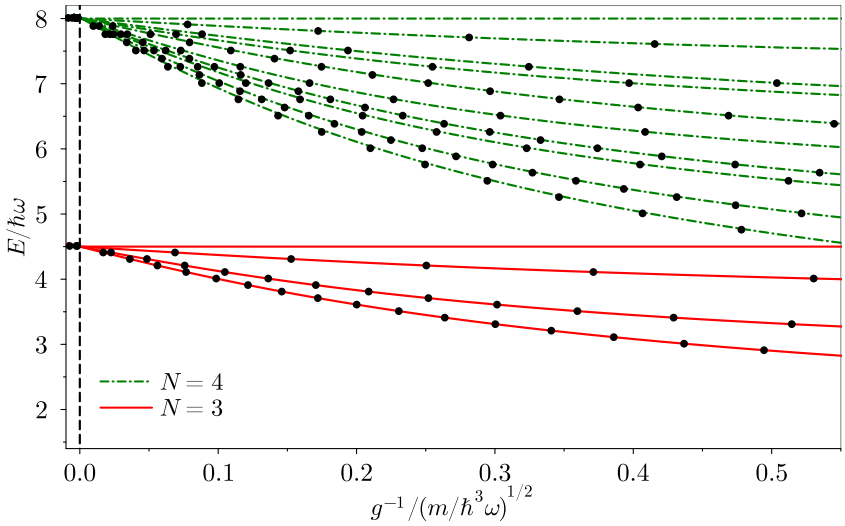

Figure 2.5: Low-energy spectra for three and four particles. The systems of three and four particles are computed with 90 and 45 harmonic oscillator modes, respectively. The lines correspond to the corrected computations, and the black circles represent the exact results of Laird et al. (2017).

results, by computing the interaction strength at which the ground state reaches the Tonks energy E_∞.

We obtained that the Tonks energy is reached for $N \leq 5$ at $1/g \sim 10^{-3}$, whereas the $N = 6$ case reaches this limit at $1/g \sim 10^{-2}$. This error can be reduced by increasing the number of modes in the calculations but is extremely close to the analytical value if one compares with the non-corrected results, reaching the limit at $1/g' \sim 10^{-1}$. The lesser precision of the $N = 6$ case may be caused by the lack of modes in the calculation. We have used 20 modes, and at the same time, the Tonks energy for this system is $E_\infty = 18\hbar\omega$. As we have explained, in order to obtain reasonable results, we need to use more single-particle modes than the energy of the energy E of the corrected state, and in this case, it is close to this limit and may cause it to work a bit worse than in other cases. Another possibility is that the correction protocol is developed using a two-particle system, and we try to correct a six-particle one, which includes much more complexity.

Even though small discrepanciesremain, the results obtained show an important improvement compared to the truncated ones, encouraging us to use this correction. But before that, we have done some more tests.

In Fig. 2.5 we show the low-energy spectra of three and four $SU(N)$ particles. We compare the results obtained with the truncation and the exact ones from Laird et al. (2017). We obtain an excellent agreement with their results, not only in the ground state energy as shown before, but also in the excited states. In terms of accuracy, the four-particle system shows greater disagreement than the three-particle one. The larger

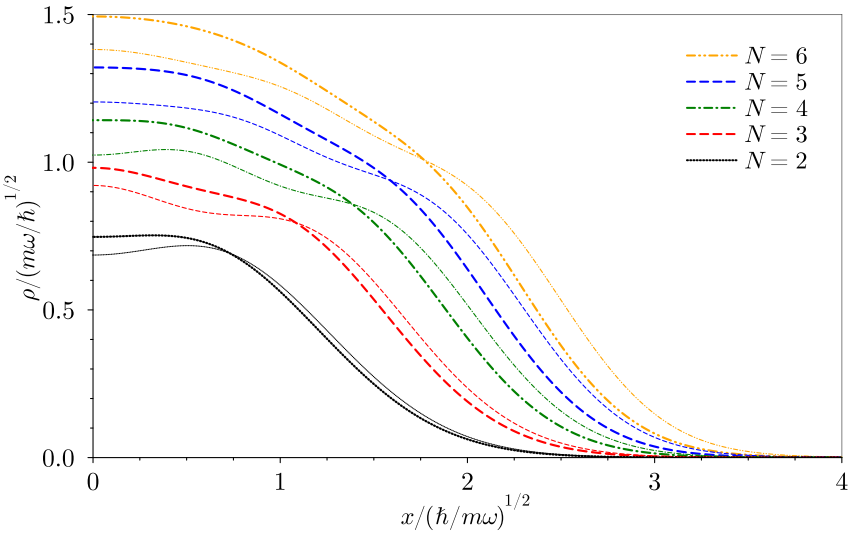

Figure 2.6: Ground state density for two to six particles. The thin lines are the results of the truncated calculations at $g'/(\hbar^3\omega/m)^{1/2} = 5$ and the thick lines are the corrected results at $g/(\hbar^3\omega/m)^{1/2} = 5$.

accuracy for the smaller system can be caused by two effects at the same time, using more modes and having a less complex system. However, the differences between our reported calculations and the exact values are almost impossible to appreciate in the figure, being less than 1% for three particles and about 1% for four particles, of the corresponding energy.

Following a similar line as in the two-particle case, here we analyze the density profile of the ground state and how the correction affects it. In Fig. 2.6 we show the ground state density profile for several particles at a fixed value of the interaction, specifically $g/(\omega\hbar^3/m)^{1/2} = 5$. We compare these results with the truncated density at $g'/(\omega\hbar^3/m)^{1/2} = 5$, obtaining some differences. The corrected densities are larger in the center of the trap than their truncated counterpart. At the same time, the truncated densities have a larger tail. In addition, the truncated densities are closer to having N peaks than the corrected ones. A characteristic of the Tonks-Girardeau limit is that the density has N peaks. This result indicates that the truncated results are closer to the Tonks limit than the corrected ones when we compare them for $g = g'$.

Another feature we appreciate in our calculations is that as the number of particles increases, more differences between the truncated density and the corrected one are observed. We use the same parameter as in the two-particle case, the correlator of Eq. (2.56) to compare the truncated density ρ_t with the corrected one ρ_c. We obtain that in general, S_ρ increases with the number of particles. Specifically, the values are $S_\rho(\rho_t, \rho_c) = 0.027, 0.041, 0.052, 0.053$, and 0.050 for two, three, four, five, and six particles, respectively. So, we can argue that as we add more particles, the effect of the correction becomes more significant. But it could be an effect also of the number of modes used

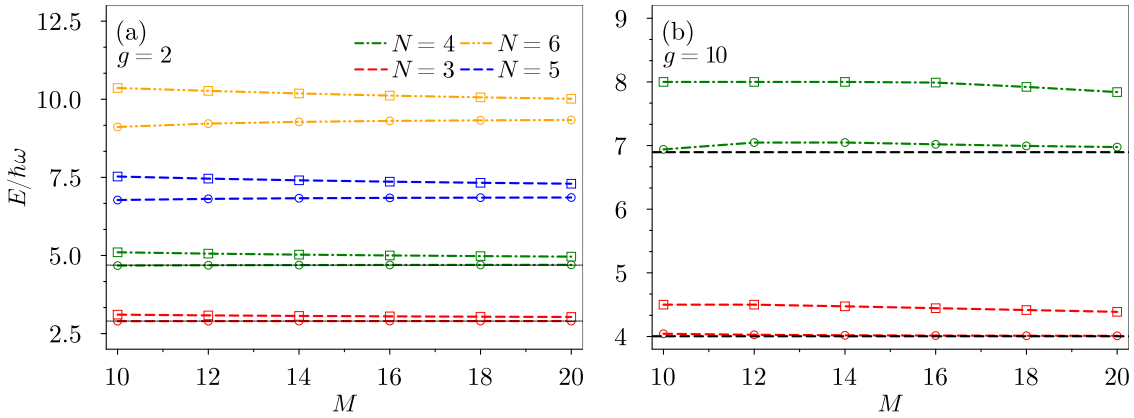

Figure 2.7: Ground state energy as a function of the number of modes used for different numbers of particles. We include the value obtained with the correction in circles and the truncated results with squares. For $N = 3$ and $N = 4$, we have included a line with the results of Laird et al. (2017). Panel (a) corresponds to a weakly interacting regime whereas panel (b) corresponds to a strong interaction.

because for more particles we used fewer modes.

An important aspect of numerical methods is the convergence. For the two-particle case, we studied the convergence of the density because we knew the analytical expression. Here, we are more limited and we only can compare how the energies depend on the size of the basis. In Fig. 2.7 we show the convergence of the energies for $N = 3$, 4, 5, and 6 particles for a weakly interacting regime and $N = 3$ and 4 for a strong interaction. We compare the energies as a function of the harmonic oscillator modes used for both the truncated and the correction calculations.

We appreciate that by using the correction we always obtain lower energies. This is not necessarily good, because even though the truncated results are an upper bound of the energy due to the variational principle, nothing guarantees that the correction gives still an upper bound. But as a general behavior, we observe that the truncated results are more stable in their dependency on the number of modes. This can indicate that they are closer to convergence, and so, we obtain good results even using a few modes. Precisely, we observe that when we use too less modes, we obtain that using the correction method, the energy obtained increases with the number of modes. This indicates that these calculations do not correspond to a variational system, where when we increases the basis we reduces the energy. For a larger number of modes, we observe that as one increases the modes in the calculations, the energies decrease, as one expects and desires, indicating a good convergence. This increase in the energy for the fewer modes could indicate that one needs a minimum number of modes to start including more many-body effects that are not included in the correction.

2.6 Conclusions

In this Chapter, we have presented the technical tools we used in this thesis, presenting the formalism to understand the Hamiltonian expressions and the second quantization. Also, we have introduced the method we employed to perform time evolution depending on whether the Hamiltonian changes with time or not. We also explained how we obtain the energy and eigenstates through exact diagonalization. Overall, we introduced the different Hamiltonians we deal with in the following Chapters. One of these Hamiltonians is the one corresponding to a few particles in a one-dimensional harmonic oscillator with contact interaction, used in Chapter 3. Another one is the Hubbard model using the two-dimensional version but considering fractal geometry in the tunneling, analyzed in Chapter 4. The third one corresponds to the model used in our proposal of a quantum battery, three sites with time-depending tunneling, discussed in Chapter 5.

In addition, we have presented a method to correct the error in the harmonic oscillator calculations. Since the harmonic oscillator has an infinite basis, one needs to truncate it, which induces an error. To overcome this problem we have introduced a method to correct the energy spectrum, which is analytic for two particles. We have derived this method using the analytical solution of the two-body problem and we checked that it also gives excellent results for systems with more particles.

3

Few particles in a harmonic trap

During the last decades, the improvements in ultracold atoms laboratories have opened the door to the study of strongly correlated systems (Zürn et al., 2012), or systems with a controllable number of particles (Wenz et al., 2013). Most studies use a lattice configuration (Bonnes et al., 2012; Raventós et al., 2017; Roux et al., 2009; Trefzger et al., 2011; Venegas-Gomez et al., 2020) or a harmonic oscillator trap potential (Deuretzbacher et al., 2010; Ebert et al., 2016; Gharashi et al., 2012; Harshman, 2014; Sowiński et al., 2013). These spatial traps are also realizable in ultracold atoms laboratories, where neutral atoms can be trapped using light, creating harmonic oscillator potentials or lattice structures, depending on the experimental setup.

Motivated by the ultracold atom experiments, where they control systems with huge precision regarding the number of particles, interaction strength, and the trapping potential (Serwane et al., 2011), the few- and many-body theoretical physics have also explored these systems (Blume, 2012; Lindgren et al., 2014; Liu et al., 2008; Xu et al., 2017a; Zöllner et al., 2006). Moreover, it is possible to control experimentally atoms with well-defined spin projection (Bloch et al., 2008). Using systems with atoms in different spin projections allows for the production of multi-component systems with all particles having the same mass. These multi-component systems have symmetric interactions by construction because the scattering length does not depend on the spin projection. The configuration with all the interactions equal is known as the $SU(N)$ symmetry (Gordillo et al., 2019; Laird et al., 2017), where N is the number of components of the system. From a theoretical point of view, it is interesting to break the symmetry and explore how the system is affected.

Another case that has captured attention is the study of impurities. The impurity problem has relevance in different branches of physics, such as in ^{3}He in liquid Helium (Fabrocini and Polls, 1998; Girardeau, 1961), electrons coupled to ionic crystals (Landau and Pekar, 1948) or nucleon impurities in neutron matter (Kutschera and Wójcik, 1993). In ultracold atoms, systems with an impurity in a Bose bath (Hu et al., 2016; Jørgensen et al., 2016) and also in a Fermi bath (Nascimbène et al., 2009; Schirotzek et al., 2009) have already been produced. At the same time, the theoretical study of systems with impurities has extensive literature, existing for different statistics (Brauneis et al., 2023; Christensen

et al., 2015; Massignan et al., 2014; Vlietinck et al., 2013), or dimensions (Ardila et al., 2020; Hryhorchak et al., 2020; Koschorreck et al., 2012; Volosniev and Hammer, 2017). Because of the strong correlations between the impurity and the bath, the calculation requires sophisticated techniques.

In this Chapter, we present a study of a few interacting particles trapped in a harmonic oscillator potential. In Section 3.1, we introduce and show results corresponding to the $SU(N)$ case, i.e., where all the interactions are equal, obtaining the energy and densities as a function of the interaction strength. Then in Section 3.2, we analyze different non-symmetric interaction configurations, examining the ground state energy and density as well as the energy spectrum of the system. We also take a closer look at the correlations in the system, which helps us to better understand how the systems are structured. In Section 3.3, we consider the specific case of having an impurity in our system. There, we consider one particle that interacts with all the rest, while the other particles do not interact between them. In this situation, we explore the energies and densities as a function of the interaction using different techniques. Finally, in Section 3.4, we present the main results of the Chapter, as well as the conclusions.

3.1 $SU(N)$ fermions

In this Chapter, we deal with systems of distinguishable particles, that can be modeled by multi-component systems with only one particle per internal state. In practice, this kind of system could be modeled in ultracold atom laboratories by high spin atoms (Cazalilla and Rey, 2014; He et al., 2020; Taie et al., 2012), with at least the same number of spin projections as the number of particles, e.g., with spin-$9/2$ fermions, such as ^{87}Sr (Zhang et al., 2014), we can have up to 10 distinguishable particles if we neglect the spin wavefunction.

In ultracold atom laboratories, the particles are confined in a trap potential. A common potential is a harmonic oscillator, due to the methods used to confine the particles (Serwane et al., 2011). For this reason, we turn our attention to this confining potential. Under these conditions, exists previous studies, for example in Choudhury et al. (2020); Gordillo (2019), and also it is studied the system trapped in lattices as in Liang et al. (2019); Zhang et al. (2018, 2019). By using different strengths in each direction, it is possible to change the dimensionality of the system. With a much larger oscillator frequency, ω_z, on one axis than the other two, then the particles remain in the ground state of the z direction and the physics takes place on the xy plane, creating an effective two-dimensional system. In the case where there are two directions with much larger frequency than the third one, $\omega_z = \omega_y \gg \omega_x$, the particles remain in the ground state of the harmonic oscillator of the z and y directions, restricting the movement to the third dimension, x. This kind of potential creates an effective one-dimensional system.

As the particles confined are neutral atoms, the interactions can be modeled, in the first

approximation, as s-wave scattering. To represent this interaction, it is common to use a pseudopotential modeled by a delta function, indicating that two particles interact when they are in the same position. The strength of this interaction can be controlled via Feshbach resonance (Chin et al., 2010), relating the interaction strength to the atom-atom scattering length. In addition, for the one-dimensional case, it is possible to control the effective one-dimensional scattering length by controlling the ratio of the frequencies $\omega/\omega_\perp$ allowing access to any value of interaction strength (Olshanii, 1998),

$$a_{1\mathrm{d}} = -\frac{a_\perp^2}{2a}\left(1 - C\frac{a}{a_\perp}\right), \tag{3.1}$$

where a is the three-dimensional scattering length, $a_\perp = \sqrt{\hbar/\mu\omega_\perp}$ is the perpendicular trapping length, μ is the reduced mass and $C = |\zeta(1/2)|/\sqrt{2}$, where $\zeta(x)$ is the Riemann-zeta function. The pseudopotential is given by $U(x) = g_{1\mathrm{d}}\delta(x)$, where the strength can be obtained from the one-dimensional scattering length,

$$g_{1\mathrm{d}} = -\frac{\hbar^2}{\mu a_{1\mathrm{d}}} = \frac{\hbar^2 a}{\mu a_\perp}\left(1 - |\zeta(1/2)|\frac{a}{\sqrt{2}a_\perp}\right)^{-1}. \tag{3.2}$$

The Hamiltonian that describes this system reads,

$$\hat{H} = \sum_{i=1}^{N}\left[-\frac{\hbar^2}{2m}\frac{\partial^2}{\partial x_i^2} + \frac{m\omega^2}{2}x_i^2\right] + \sum_{a<b}^{N} g_{ab}\delta(x_a - x_b), \tag{3.3}$$

where g_{ab} is the interaction between particles a and b. Even though this Hamiltonian is general, here we examine the $SU(N)$ case, where all the interactions are equal, $g_{ab} = g$. The $SU(N)$ case was previously examined (Capponi et al., 2016; Matveeva and Astrakharchik, 2016), with well-known limits, the non-interacting and the infinitely interacting limit, as represented in Fig. 3.1.

In the non-interacting limit, the ground state is formed by all the particles populating the lowest single-particle state of the harmonic oscillator, with energy $E_0 = \hbar\omega N/2$. On the other hand, in the infinite interacting limit, the system reaches the Tonks-Girardeau limit, where due to the interaction, two particles cannot be at the same position, resulting in fermionization, which makes the particles behave as non-interacting indistinguishable fermions (Girardeau, 1960; Tonks, 1936). The ground state energy in this limit is

$$E_0(g \to \infty) = \hbar\omega\sum_{n=0}^{N-1}\left(n + \frac{1}{2}\right) = \frac{\hbar\omega}{2}N^2, \tag{3.4}$$

whereas excited states add $\hbar\omega$ to the energy. Unlike the fermionic case, the Tonks limit has additional degeneracies in the states. In particular, the ground state has a degeneracy of $D = N!$. This limit is broadly studied, find some examples in Deuretzbacher et al. (2007); Girardeau (2011); Paredes et al. (2004); Yin et al. (2011).

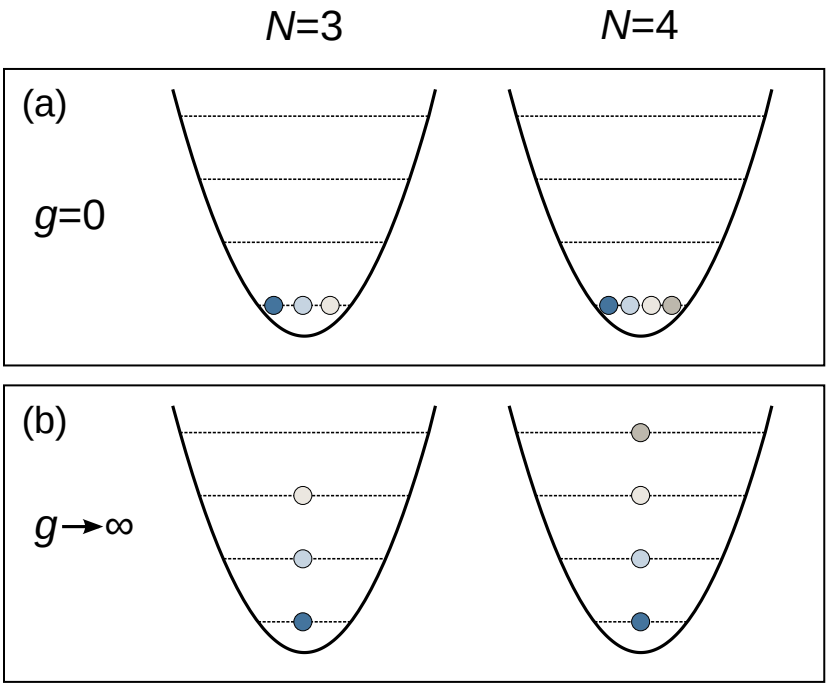

Figure 3.1: Scheme of the ground state of three and four SU(N) fermions in a one-dimensional harmonic trap. Panel (a) corresponds to the non-interacting limit and panel (b) to the Tonks-Girardeau limit.

3.1.1 Low lying properties

We examine the $SU(N)$ system for three and four particles. First, we explore the energy spectra, analyzing the energy of the ground state and the excited states as a function of the interaction strength. We only show the low-energy spectra, representing the lowest 50 states in Fig. 3.2, where we have used the correction method developed in Rojo-Francàs et al. (2022) and explained in Section 2.5. We also compare our results with the exact solution for the three- and four-body problem from Laird et al. (2017). We obtain perfect agreement, with an error below 1% for the three-particle case and about 1% as a maximum discrepancy in the four-particle system.

We reproduce the Tonks limit, but it is reached for larger interactions than $g = 20\sqrt{\hbar^3\omega/m}$, and the maximum interaction strength is shown. We have access to the infinite interacting limit after the correction using a finite value of the interaction, as explained in García-March et al. (2015); Rojo-Francàs et al. (2020). We obtain the exact energy in the Tonks limit, as well as the energies of the excitations. We have identified center-of-mass excitations in our calculations. The center-of-mass excitations can be identified because they add an extra $\hbar\omega$ energy to the previous state. For example, the first manifold in the large interaction regime is a center-of-mass excitation of the ground state manifold.

Besides the energy spectrum, we have access to additional system properties. One

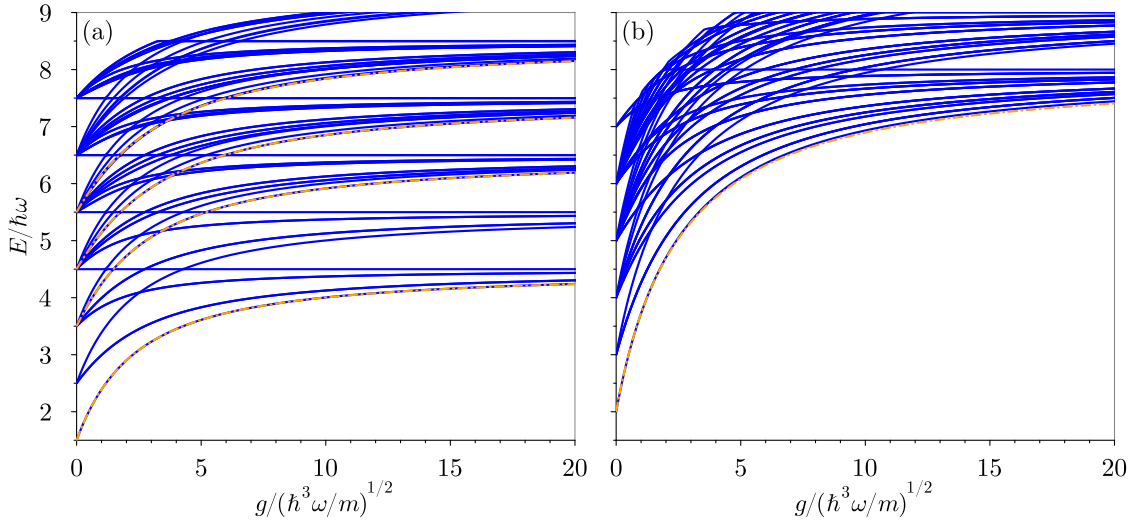

Figure 3.2: Energy spectrum of SU(N) fermions as a function of the interaction strength. Panel (a) corresponds to the three-particle case and panel (b) to four particles. The blue curves correspond to results from exact diagonalization using the correction m protocol, whereas the dashed orange curves correspond to exact calculations from Laird et al. (2017).

interesting property to explore is the ground state density. In Fig. 3.3, we show the ground state density for three- and four-particle systems for several interaction strengths. We have obtained the densities after the correction of the interaction strengths. The densities shown are normalized to one.

In the non-interacting limit, we obtain the analytical result, with all the particles occupying the lowest single-particle state of the harmonic oscillator, $n = 0$. The density of this system is a normalized Gaussian, as we have obtained. On the other hand, in the Tonks limit, the density can be analytically computed, obtaining an N-peak behavior. In our case, we obtain this limit for $g = 100\sqrt{\hbar^3\omega/m}$, with a density almost identical to the analytical one in the infinite limit. For intermediate interactions, we obtain that the system transitions from the Gaussian to the Tonks N peak structure, reaching almost the infinite interacting limit for $g = 10\sqrt{\hbar^3\omega/m}$. Additional examples have been obtained for more particles in Decamp et al. (2016).

3.2 Breaking the $SU(N)$ symmetry

Despite experimentally having access only to study the $SU(N)$ fermionic case, from a theoretical point of view it is interesting to study what would happen in a non-symmetric case. Nowadays it is not trivial to break the symmetry, because the scattering length, which governs the interaction strength depends on the atom, but not on the spin projection. To break the symmetry one needs to engineer a complex configuration of the states, as proposed in Ferraretto et al. (2023).

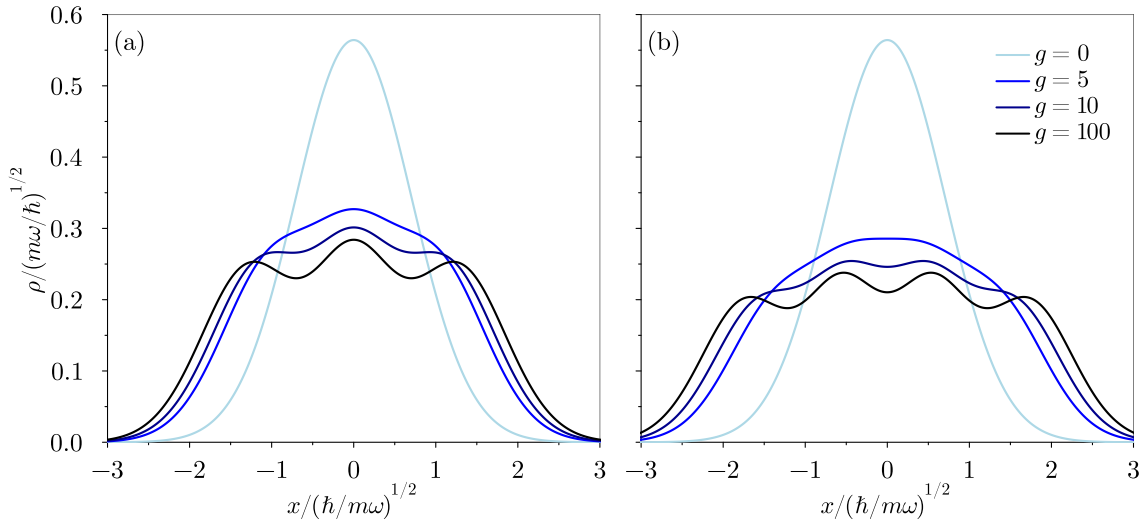

Figure 3.3: Density of the ground states of SU(N) fermions. Panel (a) corresponds to the three-particle case and panel (b) to four particles. We show profiles for different interaction strengths g. These are indicated in the legend in units of $(\hbar^3\omega/m)^{1/2}$. Note that all fermions have the same densities.

Even though we explore hypothetical systems with symmetry completely broken, where each interaction between any pair of particles can be tuned independently, but the general case depends on a large number of parameters. Therefore, we restrict our study to specific interaction constrains.

In particular, we consider systems where each pair of particles has two possibilities: they either interact with strength g or do not interact. In Fig. 3.4, we show the configurations we consider, where the lines between each particle indicate an interaction with strength g between those particles. We represent the three and four-particle cases, but this can be generalized to a larger number of particles. In that case, the number of configurations and the calculations become more complicated, leading to a loss of precision in our results.

In addition, we focus our analysis on the four-particle case. Note that for three particles, three out of the four configurations have already been studied: three non-interacting particles (0), two interacting particles (I), and the $SU(3)$ case (III). On the other hand, the case of configuration II is studied in Section 3.3.

The four-particle case has a total of eleven configurations, some of which are trivial or already studied, but others present a novel situation. The configurations 0, I, II, and V correspond to the three-particle case with an additional non-interacting particle. Configuration III is a system of two pairs of two interacting particles, and configuration X is the $SU(4)$ case. In addition, similar to the three-particle system, configuration IV is

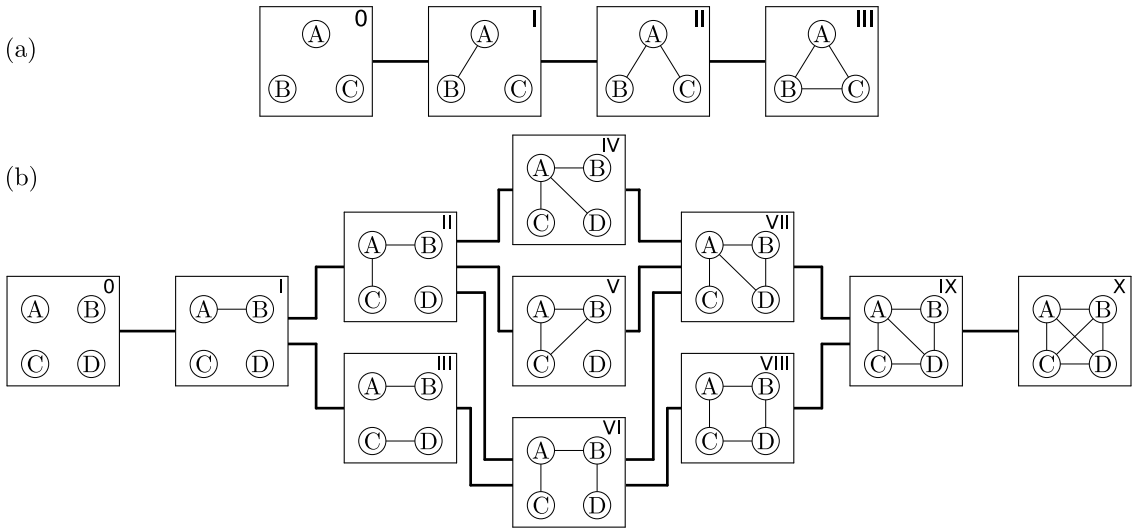

Figure 3.4: Illustrations of the different interaction configurations for three and four SU(N) fermions. Panel (a) corresponds to the three-particle case and panel (b) to four particles. Each circle represents a different fermion and the lines inside the diagrams indicate that these two components interact with strength g. The lines between diagrams indicate the possible connections by adding (or removing) only one inter-component interaction.

studied in Section 3.3, as its corresponding analogous case to the three-particle case.

We focus our study on the large interaction limit by analyzing the previously unexplored configurations using the density and pair correlation. Then, we study the transition through different configurations by progressively turning on the interactions in distinct steps.

3.2.1 Densities of non-standard configurations

Here, we analyze the density for the configurations VI, VII, VIII, and IX in the large repulsive limit, specifically with an interaction strength of $g \approx 55\sqrt{\hbar^3\omega/m}$. With this interaction strength, the system is close to the convergence that the system reaches in the infinite interaction limit. We obtain a wavefunction that closely resembles that of the infinite interaction limit, and therefore, the corresponding density on that limit.

In Fig. 3.5, we show the density for each particle in the system for the four configurations studied in this Section. In each configuration, some particles share the same density. This can be explained by the symmetry in the system between these particles. In these cases, we specify in the legend which particles correspond to each line.

When one wants to explore a state, it is usual to measure single-particle observables, such as density. In terms of computing, it is much more efficient to compute one-body observables, as they involve fewer operators. In most cases, the analysis with

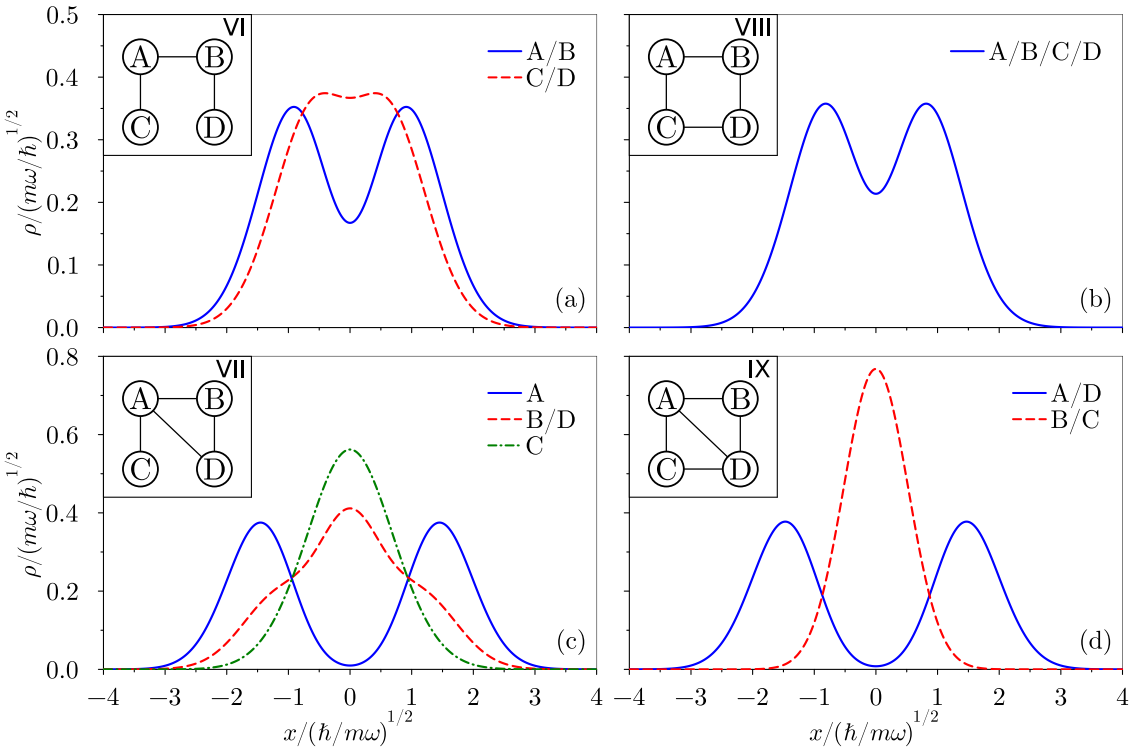

Figure 3.5: Densities of the ground states in the large interacting limit for the non-trivial configurations. Panel (a) corresponds to the densities of configuration VI, panel (b) to configuration VIII, panel (c) to configuration VII, and panel (d) to configuration IX of the diagram Fig. 3.4. All the results are obtained with an interaction strength $g \approx 55$. The density of each particle is indicated in the legend of each corresponding panel.

these one-body operators is useful and gives important information about the state, but with this approach, one cannot directly see the correlations of the system. With the description in the densities from of this Section, one can argue that there are some correlations and how the state is created using the density and the knowledge of the interactions. However, we do not have any direct proof of these correlations since the density does not provide this information. We further explain each configuration and interpret how the ground state in the infinite interacting limit behaves. The present explanations are supported by the calculations presented in Section 3.2.2.

3.2.1.1 Density of configuration VI

Configuration VI, whose densities are presented in Fig. 3.5(a), can be identified as an interacting chain. On one hand, we have the central particles, A and B, and on the other hand, the extreme particles, C and D, according to our diagram. In the density, we can identify this symmetry, obtaining the same profiles for the A-B and C-D particles, respectively. As we are in the large repulsive limit, none of the particles can be in the same position as any of their neighbors in the interaction chain. This means that particle A cannot be at the same position as B or C, creating a correlation and a separation in

space between their densities, with no restriction regarding particle D. On the other hand, particle C only has the restriction with particle A. The same restrictions apply to particles B and D maintaining the corresponding symmetry.

We appreciate a separation between the central and the extreme particles in the interacting chain, which could indicate the separation we have described that may occur. However, particles A and B have the same density but must be correlated, avoiding being in the same position, and this should create a separation between their densities. This can be explained by considering correlations, and given that there are two peaks, it is appropriate to think that one particle is on the left and the other on the right part of the trap. Due to the symmetry of the system, the state is a superposition of the two possibilities, A at left and B at right, or vice versa, creating the same density for both particles.

We can argue a similar behavior for particles C and D, where there are two peaks. In that case, the correlation is created by the interactions that these particles have with the other two. For example, as particle C cannot be in the same position as A, if A is on the left, C is pushed to the right, and at the same time, B is also on the right pushing D to the left. Since C and D do not interact, their wavefunctions can overlap, and it is energetically more favorable to be closer to the center of the trap. From our analysis, we conclude that the system in this situation has the particle creating the chain A-D-C-B, where particle A is at left border, particle D is at center left, particle C at center right and particle B at right border. The ground state is in superposition between the described state and its symmetric case, with particle B, then particle C, particle D and particle A from left to right.

3.2.1.2 Density of configuration VII

Configuration VII, whose densities are presented in Fig. 3.5(c), is analyzed from the perspective of having three $SU(N)$ particles, but one of them also interacts with a fourth particle. Here, we observe three distinct behaviors, as the symmetries only affect the interchange of particles B and D. Since the interaction is largely repulsive, it prevents any two interacting particles from occupying the same position. As a result, none of the particles A, B, and D particles can share the same position, and the same applies to particles A and C.

Starting from the $SU(N)$ case, in the infinite interacting limit, the system reaches the Tonks-Girardeau limit, where the particles behave like non-interacting fermions. The density of these systems consists of a N-peak structure, and in a simplified view, each peak corresponds to one particle, with the corresponding antisymmetrization. For three particles, we would expect one particle to be on the left, another in the center, and the third one on the right of the trap. However, by adding a fourth particle that interacts with only one of the original particles, the system is altered.

By adding particle C to the system, as it does not interact with particles B and D,

it prefers to be in the center of the trap. Moreover, since the other three particles still must adhere to the Tonks-Girardeau structure described earlier, the alteration arises from particle A, which cannot occupy the center due to particle C being there. As a result, particle A becomes localized at the edges of the trap, while the other two particles (B and D) are localized, one at the center and the other to the other side of the trap.

In summary, one of the possible configurations of the particles is A-(B/C)-D, meaning that particle A is on the left, B and C in the center, and D on the right. Of course, this configuration must be symmetrized by interchanging particles B and D, and also by symmetrizing the state with particle A on the right.

Note that the transition from configuration VI to VII modifies the system considerably. Because now A and D interact, the system experiments a transition from A and D, which is close to a case where they are separated. Also, in the procedure, particle A goes outside the trap, and particle C localizes in the center of the trap. In addition, the structure of particle B is also altered.

3.2.1.3 Density of configuration VIII

Configuration VIII, whose densities are presented in Fig. 3.5(b), can be identified as a closed interaction chain. In this case, all the particles are equivalent, in a manner similar to how a ring lattice exhibits translational invariance. Due to the strong repulsive interaction, each particle cannot be in the same position as the other two particles with which it interacts.

An easy way to explain this system is by describing the addition of each particle step by step. We start with particles A and B, which cannot occupy the same position, so the system develops a two-peak structure, wherein at each peak there is a particle, with the corresponding symmetrization. Next, we add particle C, which also cannot be in the same position as A. However, it is free to occupy the same peak as particle B in the position opposite to particle A. Finally, with the addition of particle D, which cannot be in the same position as B or C, it pairs with particle A at the same peak. Thus, the system forms a two-peak structure, with two particles at each peak, resulting in the spatial distribution (A/D)-(B/C), where A and D are on the left and B and C are on the right, again with necessary symmetrization. Note that particles A and D (and also B and C) become correlated even though they do not interact between them.

In this case, the transition from configuration VI to VIII is relatively smooth, as it simply enhances the correlations in configuration VI. The added repulsion between the outermost particles of the interaction chain prevents them from occupying the center of the trap, repelling each other. However, the overall structure remains largely unchanged, without significant alterations.

3.2.1.4 Density of configuration IX

Configuration IX, whose densities are presented in Fig. 3.5(d), can be interpreted as a $SU(3)$ interacting system where two particles share the same internal state. This system resembles an $SU(4)$ system, lacking only the interaction between the particles B and C. However, this configuration is more akin to the three-particle Tonks-Girardeau gas than the four-particle case.

For large interactions, particles A, B, and D cannot occupy the same position, and neither can particles A, C, and D. In this case, each group of three particles forms a three-peak structure. However, as two particles are shared in these groups, it follows that the particles B and C must occupy the same peak. Naturally, it is energetically more efficient to have these two particles in the center of the trap and two particles at the edges rather than one particle in the middle and three at the edge. Thus, particles B and C remain in the central position of the three-peak structure whereas particles A and D are localized on the edges, each one on a different side. Therefore, particles are distributed as A-(B/C)-D and the symmetric configuration, with particles A and D on the edges and B and C in the center.

Note that this configuration consists of two states present in the ground state of configuration VII, collapsing to the wavefunction where particle B is in the center. This indicates that the transition from VII to IX changes the system but in fact, the second configuration is created by half of the states that form the ground state of the first configuration. On the other hand, the transition from VIII to IX is achieved by adding an interaction between particles A and D, which significantly modifies the state. This transition comes from a state where A and D are correlated to a system in which these particles are anti-correlated.

3.2.2 Correlations

The study of correlations is important since they provide more information about the system than the one that can be extracted from single-particle observables. There are a large studies where the correlations are considered, see examples in García-March et al. (2014); Kinoshita et al. (2005); Mistakidis et al. (2020); Mujal et al. (2017); Olshanii and Dunjko (2003).

Once examined the densities in Section 3.2.1, now we go beyond by studying the pair correlation function, a two-body operator that takes into account the two-body correlations in the system. The definition of the operator is

$$\eta(x,x') = \int |\Psi(x,x',x_3,x_4,...x_N)|^2 dx_3 dx_4 ... dx_N \,, \tag{3.5}$$

and indicates the probability of finding particle 1 at position x and particle 2 at x'. This definition gives the pair-correlation function between particles 1 and 2, but it can be generalized for the rest of the pairs by integrating over the other particles except the

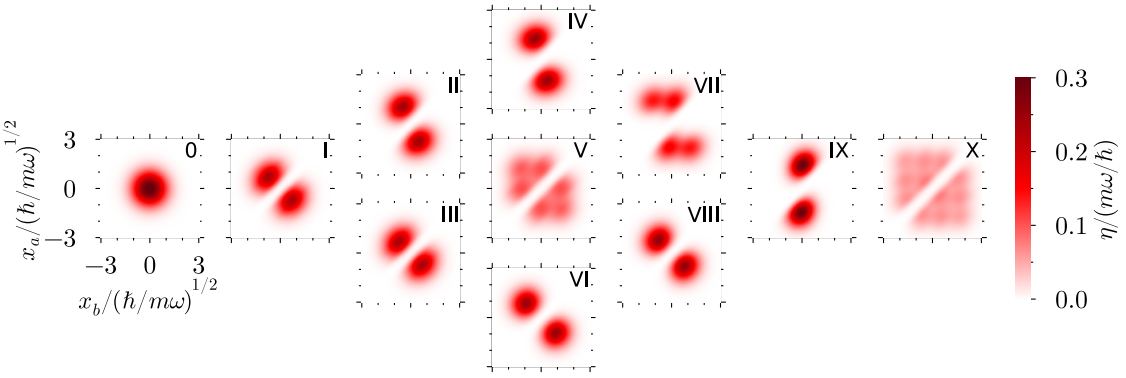

Figure 3.6: Pair correlations corresponding to all the interaction configurations. The correlations shown correspond to the pair of particles A and B, according to the diagrams of Fig. 3.4 sampled in the same position of the corresponding diagram. All the axes are equal for all the cases. The color legend is also common to all the cases.

ones for which you want to compute the function. In the case of non-correlated systems, this operator gives the tensor product of the densities of particles i and j. For this reason, sometimes it is represented as the difference $\eta(x, x') - \rho(x) \otimes \rho(x')$ to eliminate the non-correlated effects. However, doing this subtraction loses the interpretation of $\eta(x, x')$ as the probability of finding one particle at x and the other at x', making it more difficult to interpret the results. For this reason, we show the correlations $\eta(x, x')$ and not $\eta(x, x') - \rho(x) \otimes \rho(x')$. Due to the large repulsive interactions analyzed the correlations becomes important and we do not need to eliminate the density effects to describe the quantum correlation in the system. The cases without intrinsic quantum correlations corresponds to cases with $\eta(x, x') = \rho(x) \otimes \rho(x')$, which we denominate a density-density function.

3.2.2.1 Pair correlations diagram

We start with an overview of the correlation for all the configurations. In Fig. 3.6, we show the pair correlation function between particles A and B for each configuration in the large interacting limit. As in all the configurations, except the 0 one, particles A and B interact, so they are anti-correlated in all the diagrams shown and cannot be in the same position.

In Fig. 3.6, we identify some known results, such as the 0 case, corresponding to two non-interacting particles, where there are no correlations. This case corresponds to a density-density function, with both particles in the harmonic oscillator ground state. Then, the configurations I, V, and X correspond to the Tonks-Girardeau gas of two, three, and four particles, respectively. In the case of configuration III, particles A and B are correlated like a Tonks-Girardeau gas of two particles, similar to configuration I. Note that the Tonks-Girardeau pair correlation function has a regular structure of an NxN peak structure without the peaks on the diagonal $x = x'$.

According to configurations II and IV, we can consider these systems as an impurity (particle A) and two and three bath particles, respectively. By analyzing the pair correlation function, we appreciate that the impurity is localized at the edges of the trap while the bath particles remain in the center. We see that as we add a particle, from II to IV, the pair correlations become more similar to a density-density function, i.e., it is more symmetric and centered. This can be caused by the correlations becoming less important as more particles are in the system. This impurity system is explored intensively in Section 3.3.

In the cases of configurations VI and VIII, we obtain that particles A and B are completely anti-correlated, in accordance with the description we gave in Section 3.2.1.1 and Section 3.2.1.3, with a two-peak structure and each of these particles occupying one of those peaks. The interpretation of the pair correlation in that case indicates that if particle A is to the left, i.e., $x_a < 0$, then particle B is to the right $x_b > 0$, and vice versa. Of course, this pair correlation function is not a density-density function, as in that case, there would be four peaks in the diagram, indicating that the system is correlated.

In configuration VII, we obtain a different structure, with a total of four peaks. As we interpreted in Section 3.2.1.2, this system can be understood as a three-particle Tonks-Girardeau gas where one particle (A) interacts with an additional particle. Here, we can appreciate that this distribution is quite similar to the three-particle Tonks-Girardeau gas of configuration V, but the peaks are missing at $x_a = 0$. This result indicates that the system creates a structure similar to a Tonks-Girardeau for three particles, while there is an additional particle in the center of the trap, and particle A, which forms part of the Tonks-Girardeau, cannot be at the center of the trap, avoiding the occupation of these corresponding peaks.

Finally, for configuration IX, we obtain a two-peak structure, which indicates that particle B is in the center of the trap while particle A is on the edge of the trap. However, this information was available from the density, which does not show a clear correlation between these particles. Note that even though this system has almost the same interactions as the Tonks-Girardeau gas of four particles, where it only needs an extra interaction between particles B and C, the structure has not been created yet, at least in terms of the correlations between particles.

3.2.2.2 Pair correlations of extreme cases

Up to now, we have only shown examples of correlated particles that have large repulsive interactions. Of course, these particles must be at least partially correlated, as the interaction avoids having both particles at the same position. But we question what happens with the particles that do not interact. Having correlations between non-interacting particles is not a trivial thing, but it is possible via the interactions of a third particle. Here we show two cases: one where the particles are correlated and another where they

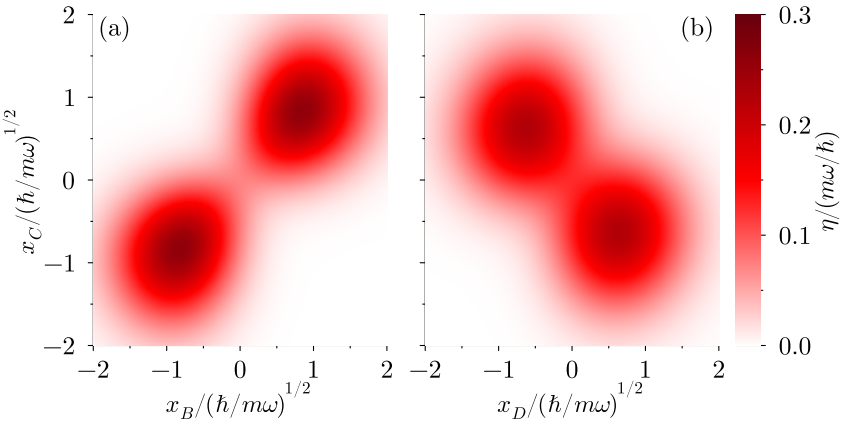

Figure 3.7: Pair correlation function of the ground state of non-trivial configurations. Panel (a) corresponds to particles C and B for configuration VIII and panel (b) corresponds to the particles C and D for configuration VI.

are anti-correlated, even though they do not interact with one another.

In Fig. 3.7, we show the pair correlation for these two extreme cases: non-interacting particles that are correlated and anti-correlated. We choose to show the case of particles B and C for configuration VIII in Fig. 3.7(a) and the case of particles C and D for configuration VI in Fig. 3.7(b). None of these particles interact, but they present a clear correlation that does not correspond to a density-density function.

For configuration VIII, we obtain results compatible with our interpretation from 3.2.1.3. This system is endowed with a two-peak structure, wherein at each peak there are two particles: one containing A and D, and the other containing B and C. Here, we have evidence that, in effect, particles B and C can be on the left or the right of the trap, but they are always in the same peak. When particle B is on the left side ($x_b < 0$), then particle C is also on the left ($x_c < 0$), and the same applies to the right side. It is interesting that even if the particles do not interact, they correlate due to the effect of the rest of the repulsive interactions in the system.

In the other case, configuration VI, the pair correlation also agrees with our interpretation in 3.2.1.1. Here, particles C and D form the ends of a chain of interactions. As we argued, in this configuration, the particles become aligned, creating a separation between C and D due to the repulsive interaction present in the system. Due to these interactions, both particles are close to the center of the trap, but at the same time, each particle is a bit pushed away to opposite sides of the trap. This effect can be observed in the pair correlation function, where both particles are anti-correlated; when particle C is on the left ($x_c < 0$), then particle D is on the right ($x_d > 0$) and vice versa. In contrast to other cases where both particles have repulsive interaction, here both particles can be found in the same position, but most of the time, they are on different sides.

3.2.3 Energy spectrum transitions

Now, we focus on how the system transitions continuously from the non-interacting case, configuration 0, to the $SU(N)$ case, configuration X, by analyzing the energy spectrum. Our procedure is to increase one interaction (or several simultaneously) from zero to a large value, close to the infinite interaction limit. Then, we turn on another interaction (or some of them) from zero to the large interaction limit, and we do this until we turn on all the interactions and create the Tonks-Girardeau gas for four particles.

We do this in two different methods. First, we examine the transitions from a Tonks-Girardeau gas of n particles to the one with $n+1$, i.e., from the non-interacting system to the two-particle, three-particle, and four-particle Tonks-Girardeau gas. Then, we study a more gradual transition, where we turn on the interactions one by one, with a total of six transitions to create the final state.

3.2.3.1 From n-particle Tonks to $(n+1)$-particle Tonks

Here we analyze the transition from the non-interacting limit to the four-particle Tonks-Girardeau gas passing through the two- and three-particle Tonks-Girardeau gases, through the energy spectrum. In doing so, we separate the transition into three different steps.

In Fig. 3.8, we show the three-step transitions as well as schemes illustrating which interactions are tuned. In the first step, we start from the non-interacting case and turn on one interaction between a couple of particles. We tune this interaction from zero to the infinite limit, where at the end of this step, we reach the two-particle Tonks gas. Then, we include an additional particle that interacts with the two previous ones; thus, we turn on these two interactions. Here, we start with a system with two particles with infinite interaction and we progressively add interaction with a third particle until we reach a $SU(3)$ system with infinite interaction, forming a three-particle Tonks gas. Finally, we add a fourth particle that interacts with all three interacting particles, turning on the three remaining interactions in the system. In that case, we go from the three-particle Tonks to the four-particle Tonks.

Note that we show the energy spectrum in each step up to a finite value of the interaction. Even considering that $g = 20\sqrt{\hbar^3\omega/m}$ is a large value, the system is close to the infinite limit wavefunction but has not converged yet. Of course, in the next steps, we use a different value of the interaction, almost in the infinite interaction limit, $g \approx 1000\sqrt{\hbar^3\omega/m}$. In this sense, we can argue that we create a gap in the interaction strength between each panel, by increasing the interaction from a large value to the infinite limit. This gap can be appreciated, as at the end of each step some states are close to being degenerate, whereas, at the beginning of the next step, these states are completely degenerate.

The first step, Fig. 3.8(a), corresponds to the two-particle system in a harmonic trap,

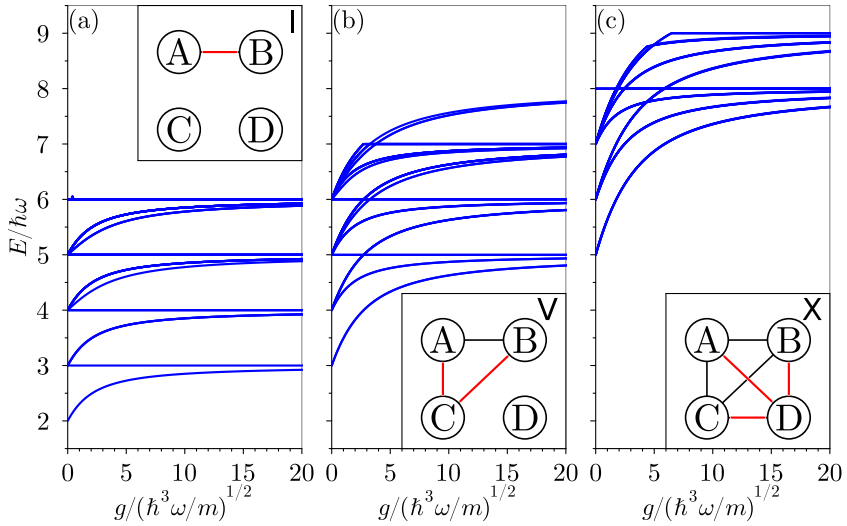

Figure 3.8: Energy spectrum of four fermions for the transition from the non-interacting to the Tonks limit. The value of the red lines of the inset diagrams correspond to the value of g on the x-axis value and the black lines are fixed at a large repulsive limit of $g/(\hbar^3\omega/m)^{1/2} \approx 1000$. Panel (a) corresponds to the transition from the non-interacting to the Tonks-Girardeau of two particles, panel (b) corresponds to the transition from two to three particles Tonks-Girardeau limit, and panel (c) corresponds to the transition from three to four particles Tonks-Girardeau gas.

with an analytical solution (Busch et al., 1998). We obtain the same spectrum as the analytical results but with some additions due to the two additional particles in the system. The ground state and the first excitation are not degenerate but in the infinite interacting limit, both states achieve the same energy. Note that the first excitation, i.e., the constant energy state as a function of the interaction strength, is not possible to find if the particles are identical bosons, as it is an antisymmetric state under the exchange of particles A and B. The second manifold has a constant gap of $\hbar\omega$ to the first manifold. Also, each of these states is three times degenerate. One of these states is a center-of-mass excitation of the ground state manifold. The other two excitations are created by the non-interacting particles, maintaining the two-interacting particles in the ground state, but one of the extra particles is in the first excited state. All the excitation with a $\hbar\omega$ gap can be created either by a center-of-mass excitation or by an excitation of one of the non-interacting particles. The intrinsic excitations, such as the one in the third manifold, are not degenerate. At infinite interaction, the system reaches the same energy spectrum as two identical fermions, where the ground state has $E_\infty = (1/2 + 3/2)\hbar\omega = 2\hbar\omega$ and all the excitations have a gap of $n\hbar\omega$. But here we need to add the energy of two non-interacting particles, so the ground state energy is $E = (1/2 + 3/2 + 1/2 + 1/2)\hbar\omega = 3\hbar\omega$, and the excitations remain with the same gaps. There is another difference with the Fermi gas because here we have a different degeneracy distribution, where the ground state is double degenerate, for example.

In the second step, Fig. 3.8(b), we create the three-particle Tonks-Girardeau gas, but

unlike the $SU(3)$ case, here we ramp up two of the three interactions while the third one is from the beginning with an infinite interaction strength. Here, the ground state is double degenerate, coming from both states from the previous step. In addition, all the states in the ground state manifold are double degenerate, with a total of six states reaching the same energy at the infinite interacting limit. The first excited state in this step, the one that goes from $E = 4\hbar\omega$ to $E = 5\hbar\omega$, comes from a six-times degenerate state from the previous step. As this state is only two times degenerate, it indicates that the degeneracy can be broken from one step to the next. Of course, the other state that is degenerate at the end of the previous step has a degeneracy of four and has a constant gap with the ground state of $\hbar\omega$. This excitation is created by a center-of-mass excitation or an excitation of the fourth non-interacting particle, resulting in four states because the ground state is already degenerated.

Finally, in the last step, Fig. 3.8, we create the four-particle Tonks-Girardeau gas. In this case, all the ground state manifolds are six times degenerate, reaching the expected 24-fold degeneracy at the end of the step. Now, the energy gain is much larger than before, as the energy increases from $E = 5\hbar\omega$ to $E = 8\hbar\omega$, corresponding to the excitation of the fourth particle from the ground state to the third excited state. We also observe the degeneracy breaking, as in the previous step, when we turn on the new interactions.

A common property found in all the steps is that the ground state manifold does not experiment any crossing. This implies that the ground state at the end of one state becomes degenerated with more states and correspond to the ground state at the beginning of the next step. While the degeneracy of the ground state only increases as the interactions are added, this not happens for the excited states. Some excited states at the beginning of the step are degenerated, but once the interaction is turned on the degeneracy is broken. This is caused because these excitations can be created by a center-of-mass, a non-interacting particle or be an intrinsic excitation of the interacting system. Due to these differences, the new interactions introduced affects different to the different kinds of excitations.

3.2.3.2 Add interactions one by one

Now, we use a different approach and study the energy spectrum as a function of the interaction strength turning on the interactions one by one, from the non-interacting to the infinite interacting regimes. Following this procedure, there are six different possible paths, as can be seen in Fig. 3.4(b). Even though there are six different paths, in some cases, they share most of the different steps. For this reason, we only examine two of them, being two of the paths which presents more differences, as some of them only differs in one intermediate state. In Fig. 3.9 we show the energy spectrum as a function of the interaction for each one of the steps to create the Tonks-Girardeau gas, tuning the interactions one by one from zero to infinity.

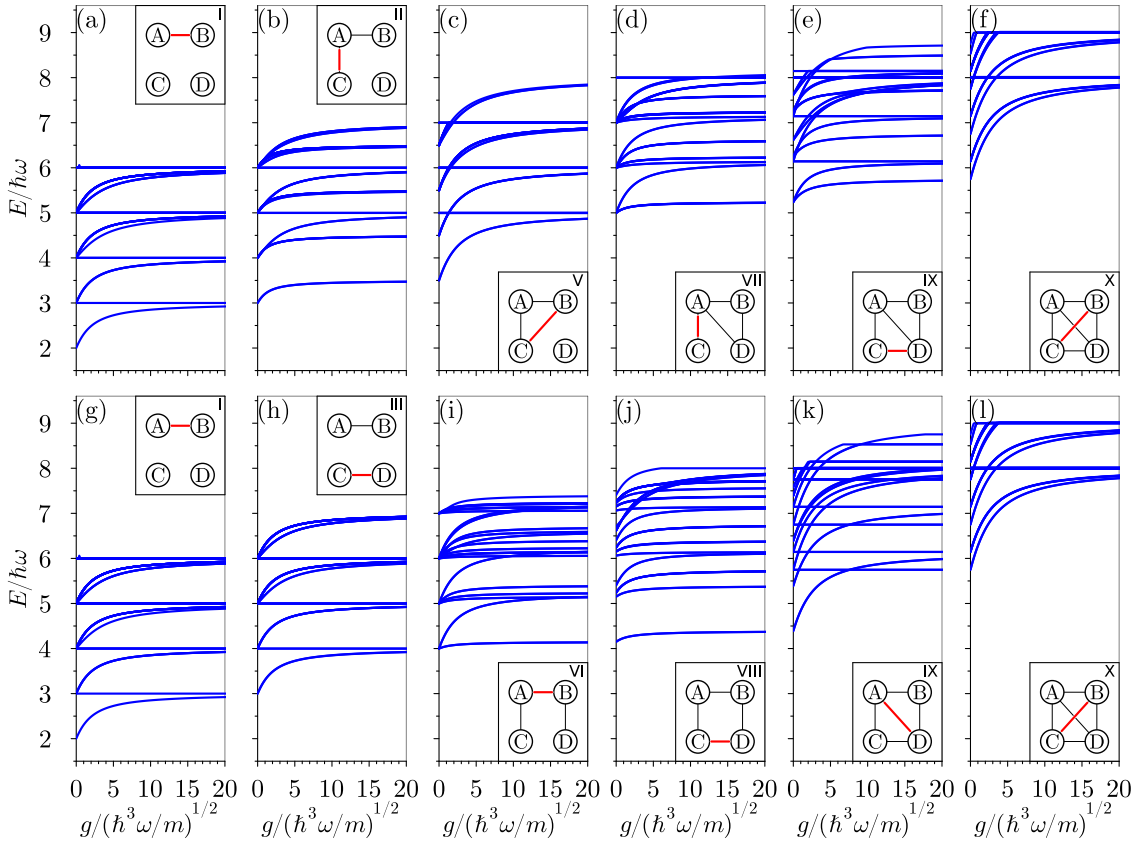

Figure 3.9: Energy spectrum of four fermions following two different paths from the non-interacting to the Tonks limit. Panels (a-f) correspond to the path through 0-I-II-V-VII-IX-X diagrams and panels (g-l) correspond to the path through 0-I-III-VI-VIII-IX-X diagrams. The black lines between the components correspond to a fixed interaction strength $g \approx 1000\sqrt{\hbar^3\omega/m}$ and the red ones correspond to the value g on the x-axis.

The first transition considered is the path 0-I-II-V-VII-IX-X, represented in Fig. 3.9(a-f), where we also find the Tonks gas for two and three particles at some point of the path. The first step, Fig. 3.9(a), is exactly the same as in the case of 3.2.3.1, being basically the two-particle (A and B) problem with two additional non-interacting particles (C and D).

The next step, Fig. 3.9(b), is to add interaction with another particle, C, that interacts only with one of the previous particles, A. We observe that the ground state energy increases only marginally, indicating that energetically, the ground state without this new interaction is nearly equivalent to the state when the interaction is infinite. During this step, the ground state of the system transitions from particle C in the center of the trap and particles A and B correlated one on each side, to a system where particles B and C are in the center of the trap and particle A on the edges. Thus, the structure of the system changed localizing particle B in the middle and spreading particle A, but without major alterations. Looking at the excited states, we find that the degeneracy obtained at the end of the previous step is partially broken. In general, in the infinite interacting

limit, we obtain energies that do not correspond to a harmonic oscillator eigenvalue and neither the gaps are integers of $\hbar\omega$, except for the center-of-mass excitations.

The next step, Fig. 3.9(c), involves adding interaction between particles B and C, obtaining the $SU(3)$ case when this interaction becomes infinite. In that case, the ground state energy experiments a significant increase, driven by the substantial change in the configuration of the system. We transition from having two correlated particles, B and C, in the center of the trap to a system where all three particles are anti-correlated. Notably, we observe that some states at the end of the previous step are eigenstates of the three-particle Tonks, as their energy remains constant despite changes in the interaction strength.

Now we add a fourth particle interacting with one particle of the system, Fig. 3.9(d). In this case, we redefine the interaction particles to align with the diagram of Fig. 3.4. We find that the ground state energy remains nearly constant, indicating that the configuration of the system does not change significantly. As we explained in Section 3.2.1.2, the ground state of configuration VII is particle C in the center of the trap while the other three particles form a Tonks-Girardeau-like gas. Here, particle A cannot occupy the central peak, and B and D adjust accordingly. This configuration is spatially similar to the three-particle Tonks gas with the non-interacting particle but it incorporates additional correlations. Moreover, the ground state degeneracy is broken when we add the interaction of this step. In fact, the ground state is four-fold degenerate, while the state that has the same energy when interaction A-C is zero is two-fold degenerate. This observation aligns with the spatial distribution, as the distribution of three particles can occupy three peaks, allowing for two possibilities of having particle A in the middle. Thus, when the interaction is turned on, the system experiments a significant transformation. The remaining four possibilities correspond closely to the four solutions of the system when interactions become infinite.

Then, we turn on the interaction between particles C and D, Fig. 3.9(e), where the ground state splits into two distinct states, with each state being two-fold degenerate. In this case, we can argue something similar to before, having the ground state in the infinite interacting limit correspond to two superpositions of the non-interacting case.

Finally, in the last step, Fig. 3.9(f), we turn on the remaining interaction in the system. In this case, the ground state has a two-fold degeneracy, and there is another state with a small gap that becomes degenerates with the ground state in the infinite interacting limit. At this stage, the ground state experiments a large increase in the energy due to the large difference in the system configuration between the non-interacting and infinite interacting regimes. It goes from a system with particles B and C in the center of the trap, to a system where all four particles are distributed across the trap.

On the other hand, we report the transition 0-I-III-VI-VIII-IX-X in Fig. 3.9(g-l). The first and last steps of both paths are the same, so we focus here on the description of the

intermediate steps. The second part of this path, Fig. 3.9(h), is equivalent to the first one, the two-particle system, but with an additional two-particle Tonks gas, which does not interact with the system being analyzed. Therefore, its physics is already explained.

The case where we introduce an interaction between these two two-particle Tonks-Girardeau gases, Fig. 3.9(i), breaks a significant amount of degeneracy. In fact, the ground state maintains almost the same energy. At the same time, part of the degenerate ground state at the non-interaction limit increases its energy as the interaction is turned on. This happens for a similar reason as the transition from Fig. 3.9(d), where the ground state at the end of this step is created by one part of the system at the non-interacting regime. In this case, at infinite interaction, the system is correlated with particles A and D on one side and particles B and C on the other. Initially, the ground state consists of particles A and C each one on one side, and the same for B and D, but uncorrelated between them. Then, we can expand the original wavefunction in terms of the correlated and anti-correlated systems, where one remains in the ground state and the others increase their energy with the interaction.

Adding interaction to complete the interaction circle, Fig. 3.9(j), does not significantly increase the ground state energy. This is because, as we exposed in Fig. 3.7(b), particles C and D are already anti-correlated, and the effect of the interaction enhances this correlation, but the system experiments only minor changes. Regarding the excitations, introducing this interaction widens some of the gaps but generally does not create additional degeneracies.

The next step of this transition, Fig. 3.9(k), is to introduce an additional interaction. At this point, the ground state energy experiments a significant increase, because, as we explained in Fig. 3.7(a), particles A and D (or B and C), are correlated, and when we turn on the interaction between them, it drastically alters the system, completely changing its configuration. Furthermore, we observe a ground state crossing, the only instance of this phenomenon along any path. This crossing occurs between the previous ground state and a previous excited state that does not feel the interaction, e.g., it has particles A and D anti-correlated from the beginning. After the crossing, the constant energy state becomes the ground state of the system.

As we explained, there is a direct relation between the configurations before turning on the interaction and the ground state energy increase. If the interaction is turned on between anti-correlated particles, the energy almost does not increase, as the state remains largely unaffected by the interaction. Conversely, if the initial system features correlated particles for which the interaction is turned on, the energy increases significantly. In the case where the particles are uncorrelated, the impact of the interaction varies depending on each specific case.

3.3 One impurity

Here we turn our attention to a specific case of the ones specified in the diagram of Fig. 3.4, the II for the three-particle case and the V configuration for the four-particles. These configurations have in common that there is one particle (A) that interacts with all the others, whereas the rest of the particles do not interact with each other. We refer to this situation as an impurity immersed in a bath of non-interacting particles. Of course, this situation can be extrapolated to larger systems, basically adding bath particles, with one impurity and N_b bath particles.

The study of this system can be related to the polaron problem (Dehkharghani et al., 2018; Grusdt et al., 2017; Will and Fleischhauer, 2023). We focus on the study of the energy and the density, by examining the ground state and also some spectral properties. We compare the results obtained with exact diagonalization, applying the corresponding correction with alternative models, allowing us to better understand the system.

In particular, we use a mean-field approach that reproduces well the weak-interacting regime, and we use an ansatz for the infinite interacting limit. With these comparisons, we can interpret the physics beyond the impurity problem and describe the effects we observe.

3.3.1 Alternative methods

Besides exact diagonalization, we have used two additional tools. We have used them as a support calculation, to better understand the behavior and how the state is created. First, to compare the results in the weakly interacting regime, we used a mean-field approach. On the other hand, in the infinite interacting limit, we propose an ansatz. In both cases, we can calculate the ground state energy and density. In addition, using the mean-field approach, we can access some excited states.

3.3.1.1 Mean field approach

Using a mean-field approximation gives us the possibility to cross-check the weakly interacting regime as well as to access calculations with more particles than the ones we can simulate using exact diagonalization. The mean-field wavefunction we have used is given by

$$\Psi(x, x_1, ..., x_N) = \phi(x) \prod_{i=1}^{N_b} \varphi^i(x_i)\,, \tag{3.6}$$

where $\phi(x)$ is the impurity wavefunction and $\varphi^i(x_i)$ is the i-th bath particle wavefunction. Using this wavefunction, we obtain the mean-field Schrödinger equations,

$$\left(-\frac{\hbar^2}{2m}\frac{d^2}{dx^2}+\frac{m\omega^2}{2}x^2+g\sum_i|\varphi^i(x)|^2\right)\phi(x)=\epsilon_I\phi(x) \tag{3.7}$$

$$\left(-\frac{\hbar^2}{2m}\frac{d^2}{dx^2}+\frac{m\omega^2}{2}x^2+g|\phi(x)|^2\right)\varphi^i(x)=\epsilon_b\varphi^i(x)\quad i=1,..,N_b\,, \tag{3.8}$$

for the impurity and the bath particles respectively. We solve the problem in a self-consistent procedure; using the result of one of the equations, we solve for the other and vice versa until the system converges. We use the eigenvalues ϵ_I and ϵ_b as convergence parameters. Numerically, we solve these equations by discretizing in space and diagonalizing. With that, we have the ground state and the excited states, so we can obtain the many-body ground state and also excitations.

To obtain the ground state in the iterative calculation, we take for all the bath particles the single-particle ground state and the same for the impurity. As all the bath particles are equal, the interacting term in Eq. (3.7) becomes $gN_b|\varphi_0(x)|^2$. On the other hand, we can obtain an excitation by considering the first-excited state of the impurity during the iterative solution. Doing that, the wavefunction of the bath is also affected. Another possibility is to excite a bath particle. Then we need to obtain the ground state and the first excitation for the bath equation. Then, we consider N_b-1 bath particles in the $\varphi_0(x)$ and one in the first excited $\varphi_1(x)$, resulting in an interacting term $g\,(N_b-1)\,|\varphi_0(x)|^2+g|\varphi_1(x)|^2$. It is possible to consider higher excitations using an analogous procedure.

With the converged solutions, we can compute the energy using the functional

$$\begin{aligned}E_{\mathrm{MF}}=&\int\phi^*(x)\left(-\frac{\hbar^2}{2m}\frac{\mathrm{d}^2}{\mathrm{d}x^2}+\frac{m\omega^2}{2}x^2\right)\phi(x)dx\\&+\sum_{i=1}^{N_b}\int\varphi^{i*}(x)\left(-\frac{\hbar^2}{2m}\frac{\mathrm{d}^2}{\mathrm{d}x^2}+\frac{m\omega^2}{2}x^2\right)\varphi^i(x)dx\\&+g\sum_{i=1}^{N_b}\int|\varphi^i(x)|^2|\phi(x)|^2dx\,.\end{aligned} \tag{3.9}$$

where we perform the derivatives and integrals numerically in discretized space.

The densities are also a straightforward calculation at this point, being simply $\rho_I=|\Phi(x)|^2$ for the impurity and $\rho_b=\sum_i|\varphi^i(x)|^2$ for the bath.

3.3.1.2 Ansatz in the infinite interaction limit

The impurity problem does not have an analytically known solution for the infinite interacting limit. For this reason, this limit cannot be used as a benchmark, unlike

in the symmetric case. For that, we propose an ansatz for the wavefunction in the limit of $g \to \infty$. In this limit, the impurity cannot be in the same position as any of the bath particles, and to fulfill this condition, we write our ansatz with Jastrow-like correlations (Jastrow, 1955)

$$\Psi_N(x_I, x_i) = \alpha_N \mathrm{e}^{-x_I^2/2\sigma_I^2} \sum_{N_a=0}^{\lfloor N_b/2 \rfloor} \sum_P \prod_{i\neq j}^{2N_a} |x_I - x_i||x_I - x_j| \mathrm{e}^{-(x_i^2+x_j^2)/2\sigma_b^2} \prod_{k\neq i,j}^{N_b-2N_a} (x_I - x_k) \mathrm{e}^{-x_k^2/2\sigma_b^2}, \tag{3.10}$$

where x_I is the position of the impurity, x_b are the positions of the N_b bath particles, α_N is the normalization constant that depends on the number of particles N, and σ_I and σ_b are variational parameters that are adjusted numerically. In the sums, N_a denotes the number of pairs of absolute values, P denotes the permutations of the index i, j and k, and $\lfloor x \rfloor$ is the floor function.

The ansatz includes an exponential for each particle due to the harmonic confinement. The factors $(x_I - x_a)$ avoid having the impurity at the same position as any bath particle. The ansatz includes only an even number of absolute values for parity conservation. We also add the variational parameters σ to minimize the energy. The Eq. (3.10) improves upon a similar ansatz proposed in García-March et al. (2016) by adding complexity with the inclusion of the superposition of the absolute value terms and the σ parameters.

The reason for including the linear combination of the absolute values is because the simple ansatz without absolute values,

$$\psi(x_I, x_i) = \alpha(x_I - x_A)(x_I - x_B)\mathrm{e}^{-(x_I^2+x_A^2+x_B^2)/2}, \tag{3.11}$$

and including absolute values,

$$\psi(x_I, x_i) = \alpha|x_I - x_A||x_I - x_B|\mathrm{e}^{-(x_I^2+x_A^2+x_B^2)/2}, \tag{3.12}$$

is because they result in the same energy. However, these wavefunctions are not orthogonal; thus, a linear combination of them gives a better variational solution. We have found that the minimum energy is obtained when all the functions have the same weight (see Appendix A for more details).

As an example, the ansatz for three particles ($N_b = 2$) reads

$$\Psi_3(x_I, x_A, x_B) = \alpha_3 \left((x_I - x_A)(x_I - x_B) + |x_I - x_A||x_I - x_B|\right) \mathrm{e}^{-x_I^2/2\sigma_I^2 - \left(x_A^2+x_B^2\right)/2\sigma_b^2}, \tag{3.13}$$

where A and B denote the two particles in the bath. In this example, the first term has $N_a = 0$, i.e., without absolute values, while the second term has $N_a = 1$, i.e., a pair of absolute values. For a larger number of particles, the ansatz becomes more complex but with an analogous construction. We provide some examples in Appendix A.

We want to optimize our wavefunction to obtain the minimum energy possible. For that, we obtain the optimal values of σ_I and σ_b numerically for each number of particles N. We report the obtained σ values in Appendix A. We also obtain better results than the previous ansatz from García-March et al. (2016). However, the prediction of our ansatz becomes less accurate for a large number of particles N.

3.3.2 Energy dependence on the interaction

We start by studying the energy of the impurity system as a function of the interaction strength. We explore both the ground state for several numbers of particles and also the low-energy spectrum, where we can identify a common pattern across different particle numbers. With all of that, we use the results obtained with exact diagonalization to cross-check the ansatz results and we use the mean-field results to interpret and give a qualitative explanation of the states.

An interesting feature of this system is that the ground state is the same whether the bath is composed of identical bosons or distinguishable particles. The differences appear in the excited states, where the distinguishable bath has additional states compared to the identical boson bath.

3.3.2.1 Ground state energy for strong interactions

Here, we focus on studying the ground state energy as a function of the interaction strength. As we deal with systems with different numbers of bath particles, we define the energy increase due to the impurity-bath interaction

$$\mu(g, N) \equiv E(g, N) - E(g = 0, N)\,, \tag{3.14}$$

where g is the interaction strength and N is the number of particles. In similar studies, μ is referred to as the polaron or binding energy of the impurity (Jørgensen et al., 2016). This quantity can be interpreted as the energy required to add the interacting impurity into the system. Using this definition, we can compare results for different numbers of particles, because in the non-interacting limit the systems with different number of particles have the same polaron energy, $\mu = 0$.

The system of three particles, i.e., an impurity and two bath bosons has already been studied (Zinner et al., 2014), where an analytical result for the infinite interacting limit, $\mu = 3/2\hbar\omega$, was obtained. Even though there is an exact solution for the three-particle case, there is no known solution for larger particle numbers. Here, we obtain the values numerically in the infinite interacting limit, and we also compare them with the ansatz of Eq. (3.10) in Tab. 3.1. We also compare the ansatz predictions with the one previously proposed in García-March et al. (2016), where we obtain smaller energies with our ansatz, indicating that we have improved the function that describes the system.

The result obtained using exact diagonalization with the correction differs only by

N	3	4	5	6	7	8
μ_{ED}	1.499	1.826	2.064	2.253	2.415	2.549
μ_{ansatz} Eq. (3.10)	1.537	1.948	2.298	2.608	2.891	3.152
$\mu_{\text{prev.}}$ (Ref. García-March et al. (2016))	1.667	2.143	2.596	3.068	3.552	4.043
K	1.145	1.379	1.538	1.678	1.834	1.933

Table 3.1: Binding energies and derivatives computed at the infinite interacting limit for different numbers of particles. The binding energies μ are in units of $\hbar\omega$ and the derivatives K in units of $(\hbar^5\omega^3/m)^{1/2}$. The exact diagonalization (ED) results (first and fourth rows) are obtained for $g = 1000(m/\hbar^3\omega)^{1/2}$. The second row shows the energies at $g^{-1} = 0$ obtained from ansatz Eq. (3.10), while the third row shows the energies obtained with the ansatz proposed in García-March et al. (2016).

a 0.07% from the exact result for three particles. Also, according to our ansatz, we obtain a similar energy, indicating that the function gives a good description of the state. For a larger number of particles, the discrepancies increase, reaching a 24% of discrepancy, for the largest system computed, $N = 8$, which is 9% of the total energy. However, it is an important improvement compared with the simpler and previous ansatz from (García-March et al., 2016), which has a discrepancy of 59% for $N = 8$ when compared with our exact diagonalization result. Nevertheless, these discrepancies indicate that to describe the impurity system in a few-body system we cannot rely on simple analytical approaches.

Another analytical property derived in Zinner et al. (2014) for $N = 3$ is the derivative in the infinite interacting limit of the energy,

$$K = -\left[\frac{d\mu}{dg^{-1}}\right]_{g^{-1}=0}. \tag{3.15}$$

This magnitude is related to Tan's contact (Barth and Zwerger, 2011), which can be used to compute the interaction energy as $E_{\text{int}} = g^{-1}K$ as dictated by the Hellmann-Feynman theorem (Feynman, 1939). They obtain the exact result $K = \frac{9}{\sqrt{2\pi^3}} \approx 1.143$ for $N = 3$. For this reason, in Tab. 3.1, we show the numerical calculation of K using exact diagonalization results. For the three-particle case, we obtain almost the exact result, indicating that our numerics are robust. We obtain that K increases with the number of particles, indicating that as we have more particles, the interacting energy increases faster as we approach the infinite interacting limit.

In Fig. 3.10, we show the ground state energy increase μ as a function of the interaction strength in the large-interacting limit, $g^{-1} \approx 0$, for several numbers of particles up to $N = 8$ ($N_b = 7$). We also compare our calculation with the exact results for $N = 3$ obtained in Zinner et al. (2014), achieving perfect agreement over the entire range.

As expected, the energy increases with the interaction, and it reaches non-trivial values for the infinite interacting limit. We also find that by increasing the number of

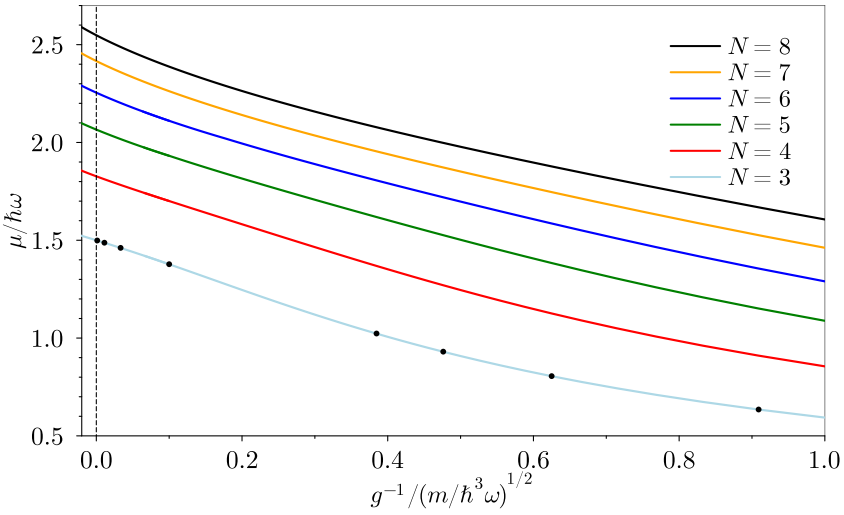

Figure 3.10: Ground state binding energy as a function of the inverse of the interaction strength. We show results for three to eight particles, as indicated in the labels. The solid lines correspond to results from exact diagonalization, while the black circles correspond to the results reported in Zinner et al. (2014). We have employed 90, 45, 30, 20, 15, and 15 HO modes for three, four, five, six, seven, and eight particles, respectively.

particles, the energy μ also increases. These features mean that it requires more energy to add the interacting particle into a system with a larger repulsive interaction or more bath particles, as expected.

An interesting behavior we have observed in the range of particles we computed is that in the infinite interacting limit, $g^{-1} = 0$, the energies increase with the number of particles, but this increase is smaller for larger baths. To be precise, we observe

$$\mu(\infty, N+1) - \mu(\infty, N) > \mu(\infty, N+2) - \mu(\infty, N+1)\,, \tag{3.16}$$

which can be observed in both Fig. 3.10 and Tab. 3.1. Using the values we have obtained in this limit, with the objective of estimating the energy for larger systems, we extrapolate our results by fitting a function

$$\mu(\infty, N) = \Delta E \left(1 - \frac{1}{N^b}\right)\,, \tag{3.17}$$

where ΔE and b are parameters to be determined. The best fit for our numerical results gives $\Delta E = (6.7 \pm 0.2)\,\hbar\omega$ and $b = 0.228 \pm 0.009$. This function fits well with our results, but it is not clear if for larger N the fit still works.

In the function Eq. (3.17), the parameter ΔE is the theoretical energy μ that the system reaches in the infinite interaction limit with an infinite number of particles N. As we have obtained a finite value for ΔE, it implies that the system saturates for large N. However, the total energy E in that case diverges as can be seen in the

non-interacting energy ($E = N/2\hbar\omega$), that also diverges. As we mentioned earlier, this result comes from an extrapolation fitting a function to a few particle results and we cannot ensure that it is still valid for large particle systems. However, this saturation can be understood in terms of the wavefunction properties. In the infinite interacting limit, the impurity cannot be at the same position as a bath particle. For a few particles, this implies that correlations appear in the system, preventing the system from having interacting energy. However, in the many-body limit, the impurity wavefunction cannot overlap with the bath wavefunction, which also has zero interacting energy. Under these conditions, and assuming that for an additional particle, the shape of the bath remains unchanged, adding an extra particle does not increase the energy, as the single-particle wavefunction remains equal and there is no interaction energy. We have assumed that the bath particles remain in the harmonic oscillator ground state, and with all of this, the binding energy μ saturates for large N.

3.3.2.2 Low energy spectra

The results of the ground state energy, where we found non-trivial energies at the infinite interacting limit, prompt us to study in more detail the impurity system. To do this, we study the low-energy spectrum, where the excited states can be used to gain insight into the ground state structure.

In Fig. 3.11, we show the low-energy spectrum for the impurity system from $N = 3$ to $N = 8$ as a function of the interaction strength, obtained with exact diagonalization. We distinguish the center-of-mass excitations from the intrinsic ones. The center-of-mass excitations arise from the separability of the center-of-mass Hamiltonian (Busch et al., 1998), which has an energy gap of $n\hbar\omega$ with another state, where n is an integer number. As we mentioned before, the ground state is the same regardless of whether the bath is formed by identical bosons or distinguishable particles. However, the spectrum presents differences because the distinguishable bath includes more excitations than the boson bath. Nevertheless, all the states that exist in a boson bath also exist in the distinguishable bath. We have differentiated in the figure both types of excitations that exist only if the bath is distinguishable or if they are boson bath state. We also compare the $N = 3$ results with the exact results from Zinner et al. (2014), obtaining a perfect agreement.

In the non-interacting limit $g = 0$, the energies correspond to the harmonic oscillator eigenvalues, $E = \hbar\omega \sum_i^N (n_i + 1/2)$, where n_i are the occupation numbers of the particles. Note that in this limit, the states are degenerate, and the degeneracy depends on the nature of the bath. This degeneracy is partially broken when the interaction is turned on, as we can see in all the panels of Fig. 3.11. On the other hand, in the infinite interacting limit $g \to \infty$, the energies saturate to non-trivial values, no longer being harmonic oscillator eigenvalues. In addition, the states become degenerate again, but with a different distribution of degeneracies.

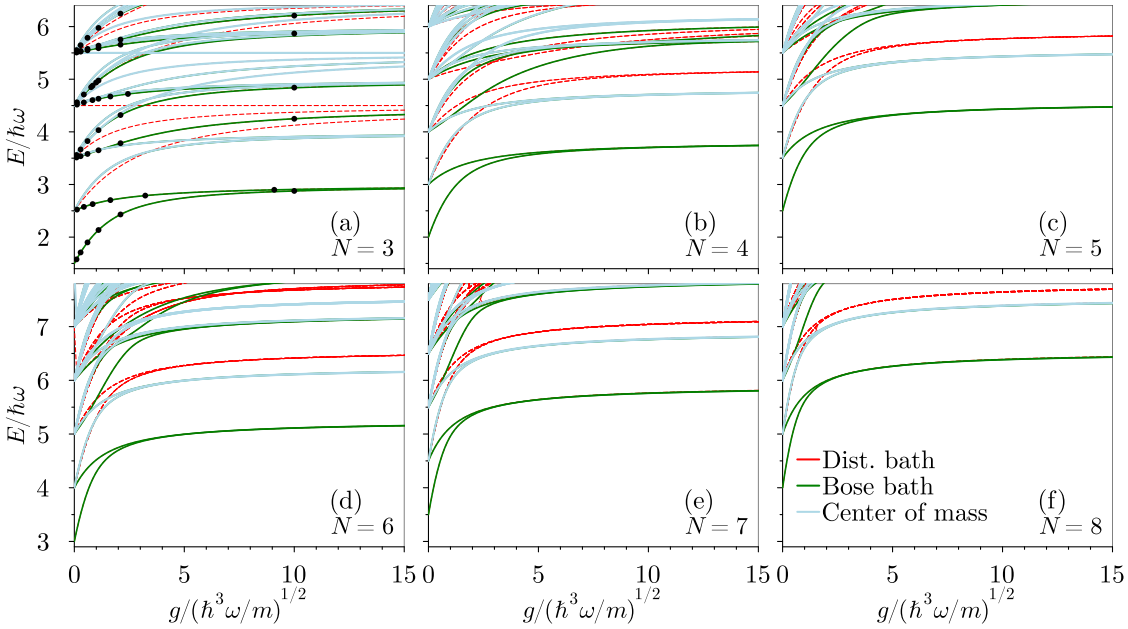

Figure 3.11: Low-energy spectrum for an impurity with a different number of bath particles as a function of the interaction strength. Panels (a-f) correspond to each one to a different number of particles, from three to eight particles as indicated in each panel, respectively. The lines correspond to results from exact diagonalization while the black circles correspond to the results from Zinner et al. (2014). We use 90, 45, 30, 20, 15, and 15 HO modes for the three, four, five, six, seven, and eight particles, respectively. The green lines correspond to the ground state and the intrinsic excitations of a system with either a bosonic or a distinguishable bath, while the red ones correspond to the states that are present only with a distinguishable bath. Finally, the cyan lines correspond to the center-of-mass excitations.

Analyzing the strongly interacting regime, and focusing on the infinite limit, we observe that the ground state becomes degenerates with one odd-parity state, for any number of particles. Note that the ground state is an even-parity state for any N. The first excitation of this doublet is a center-of-mass excitation, also with the same degeneracy. For $N = 3$ the second excitation manifold reaches an energy of $E = 9/2\hbar\omega$, corresponding to the Tonks-Girardeau energy for three particles. For larger systems ($N > 3$), the second excited manifold consists of states that only exist for a distinguishable bath, having energies below the corresponding Tonks-Girardeau limit. These manifolds are slightly more energetic than the center-of-mass excitation, and in a similar way as the ground state, they are characterized by a doublet structure. However, each line of the excited doublet is degenerate $N - 2$ times.

Due to the similarities between the ground state doublet and the excited one, we suggest that they can be created by a similar phenomenon. For this reason, we analyze these states in more detail. In Fig. 3.12, we show the ground state and excited doublets energies μ, obtained using exact diagonalization and also using the mean-field approach

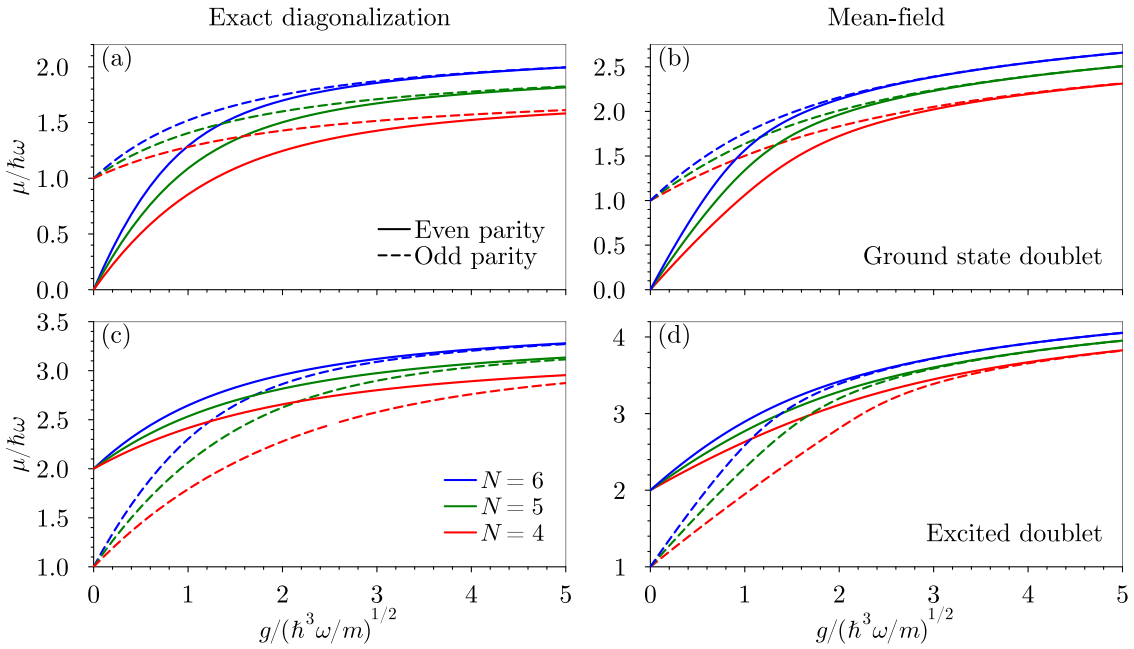

Figure 3.12: Binding energy structure for the two lowest doublets as a function of the interaction strength. Panels (a) and (c) correspond to results obtained with exact diagonalization, whereas panels (b) and (d) correspond to mean-field solutions. Panels (a) and (b) show the ground state doublet, while panels (c) and (d) show the first excited doublet. Solid lines correspond to states with even parity and the dashed lines correspond to states with odd parity.

with the corresponding excitations. Note that the behavior obtained with the mean-field technique is in qualitative agreement with the exact diagonalization results, even though the values differ.

As we discussed in Section 3.3.2.1, the ground state manifold energy μ in the infinite interacting limit increases with the number of particles. In addition, as the number of particles increases, we observe that the gap closes for a weaker interaction strength. On the other hand, the excited doublet presents similarities, as it is created by a pair of curves, with $N-2$ degenerate states each. All the states in each curve have the same parity, and one curve has the opposite parity compared to the other. Also, the energy in the infinite interacting limit increases with the number of particles, and the gap closes for weaker interactions as the number of particles increases. We obtained all of these features for both exact diagonalization and the mean-field approach calculations.

As a difference, the excited doublet closes the gap for larger interactions than the ground state doublet. Also, as we have reported in the energy spectrum analysis, the excited doublet reaches a higher energy than the center-of-mass excitation of the ground state whereas in the non-interacting regime, it has the same energy. This means that the excited doublet gains more energy from the non-interacting to the infinite interacting limits compared to the ground state.

The behavior of having a doublet that closes for large interactions is also present in a single particle immersed in a double-well system. In the double-well, we obtain also that the ground state doublet consists of an odd and an even parity state. We can map our system to one particle (the impurity) in a double well, created by the harmonic confinement and the N_b bath particles acting as a central barrier, adopting a mean-field approach with interaction strength g. The Hamiltonian that describes this effective model is

$$\hat{H} = -\frac{\hbar^2}{2m}\frac{d^2}{dx^2} + \frac{m\omega^2}{2}x^2 + gN_b|\varphi(x)|^2\,, \tag{3.18}$$

where one can take $\varphi(x)$ as the ground state harmonic oscillator wavefunction, representing that the bath remains in the ground state as a first approximation. Note that our mean-field approach is an improvement over this simple model in that we can adapt the bath wavefunction. However, this simpler model is much easier to interpret and provides us with the intuition to interpret the few-body system. Some similar examples with a double-well potential with a few particles can be found in Chen et al. (2022); Erdmann et al. (2019).

The solution of the double well shows that the ground state and the first excitation, each one having opposite parity, become degenerate when the barrier becomes infinite. This can be interpreted as the first excitation is, in fact, an impurity excitation. This is in agreement with our mean-field approach, where we computed the ground state doublet as one state with all the particles in the ground state, and the other by taking the first excitation of the impurity.

For the excited doublet, it is also possible to map it into the double-well model. In that case, we consider a different, barrier, which is now wider. If we excite one of the particles of the central barrier, we add $\hbar\omega$ to the energy due to the harmonic oscillator confinement. Also, the effect of a wider barrier is to increase the energy of the particle in the double-well for large interactions and also to close the gap for larger interactions compared with the narrow central barrier. All of these effects are in accordance with the results we have obtained using our numerical techniques. In addition, in our mean-field approach, we computed the excited doublet by using one state with $N_b - 1$ bath particles in the ground state $\varphi_0(x)$ and one on the first excited $\varphi_1(x)$ with the impurity on the ground state, and the other state with the same bath configuration, but the impurity in the first excitation.

In conclusion, the ground state of this system can be interpreted as the impurity in an effective double well, created by the bath particles. Also, there are excited states associated with the excitations of the bath. Note that the excited doublet is only present if the bath is created by distinguishable particles. We have used this interpretation in our mean-field approach, obtaining results that are compatible with those from exact diagonalization. However, for the mean-field approach, the energy diverges for large interactions, whereas in the exact diagonalization, we obtain saturation. But for weak

interactions, where the mean field makes sense, we obtain results that are closer to the exact diagonalization ones.

3.3.3 Ground state densities

Now, to gain more insight into the system, we explore the density as a function of the interaction strength. We compute both the impurity and the bath densities, which we use to visualize and crosscheck the assumption that the impurity is in an effective double-well potential. This allows us to appreciate the regime of validity of the mean-field approach, as well as how the ansatz fits with our numerical wavefunction.

In Fig. 3.13, we show the ground state density for three, four, five, and six particles for weak, intermediate, and strong interactions. We show the impurity and bath densities obtained with exact diagonalization and mean-field calculations. It is noteworthy that in the ground state, all the bath particles have the same density; therefore here we only show the density of one of them, which allows for a good comparison across the number of particles and also being of the same order as the impurity density. For large interactions, as we approach to the infinite interacting limit, we also compare with the densities derived from the ansatz. For $N = 3$, we compare our numerics with the exact results from Zinner et al. (2014), obtaining a perfect agreement with the exact diagonalization results. It is important to note that the densities expand over all the space, but as they are symmetric, we only show results for positive x.

In the non-interacting limit $g = 0$, the ground state of the system is configured with all the particles in the harmonic oscillator ground state, resulting in a Gaussian density function for each particle. When the interaction is turned on $g > 0$, the impurity starts to spread to minimize the energy, eventually developing a two-peak structure with a minimum at the center of the trap. In contrast, the bath particles exhibit the opposite behavior, becoming more concentrated in the center of the trap. However, this effect on the bath particles is much less significant than the changes observed in the impurity. Thus, the bath remains in the middle of the trap, creating an effective barrier for the impurity as the interaction grows, repelling the impurity outward from the trap, in accordance with the double-well interpretation.

The results for different numbers of particles share the general behavior, with small discrepancies. First, as the number of particles in the system increases, the perturbation on the bath is less important for a fixed interaction g. This is the expected behavior, as the effect of a single particle (the impurity) becomes less pronounced in a large system (bath) than in a small one. In parallel, for a fixed interaction g, the effect on the impurity is more significant as the number of bath particles increases. To be more precise, the impurity is repelled from the center of the trap for weaker interactions as N_b increases. This behavior is in accordance with the mean-field interpretation and the effective single-particle model, as the interacting term depends on the product gN_b.

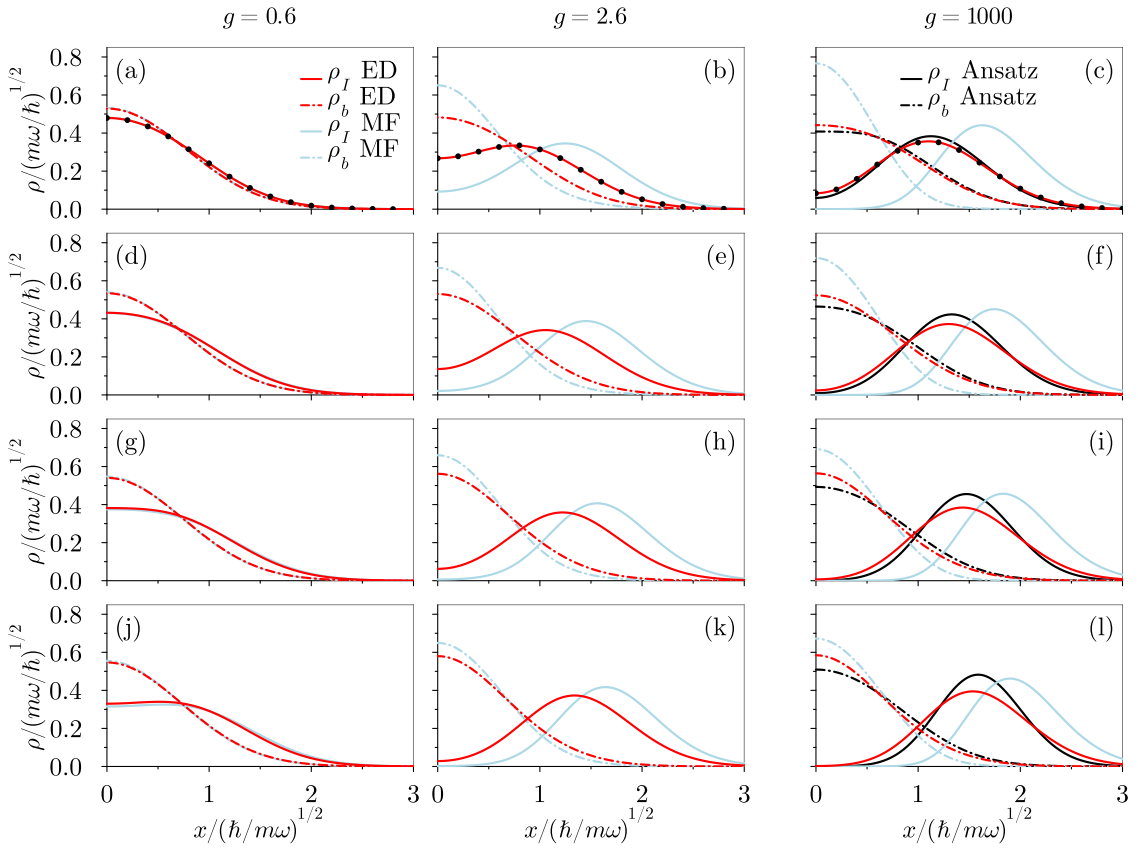

Figure 3.13: Ground state densities for three, four, five, and six particles for a selection of interaction strengths. Panels (a-c) correspond to three particles, panels (d-f) correspond to four particles, panels (g-i) to five particles, and panels (j-l) to six particles. Each column corresponds to results for a chosen interaction strength, as indicated at the top of the figure, with g in units of $(\hbar^3\omega/m)^{1/2}$. The solid lines correspond to the density of the impurity (ρ_I), whereas the dash-dotted lines correspond to the density of one of the bath particles (ρ_b). The red lines correspond to ED calculations, the cyan lines correspond to MF solutions, and the black lines in the right panels correspond to the densities predicted by ansatz Eq. (3.10) for infinite repulsion. Additionally, the black circles in the top panels correspond to the impurity's density reported in Zinner et al. (2014) for $N = 3$. Note that for small interactions ($g/(\hbar^3\omega/m)^{1/2} = 0.6$) the MF results are almost indistinguishable from the ED results.

For weak interactions, we obtained almost perfect agreement between the exact diagonalization and mean-field calculations, as we expected. However, when the interaction becomes stronger and we are in an intermediate interacting regime, both calculations start to disagree. The mean-field calculations seem to work fine since the impurity develops the two-peak structure. However, for large interactions, the mean-field approach gives poor results, especially for the three-particle case. The main difference is in the overlap between the densities of the impurity and the bath, where we observed a much larger overlap with the exact diagonalization method. This shows that the system is largely correlated, but the mean field cannot capture this physics. Nevertheless, the

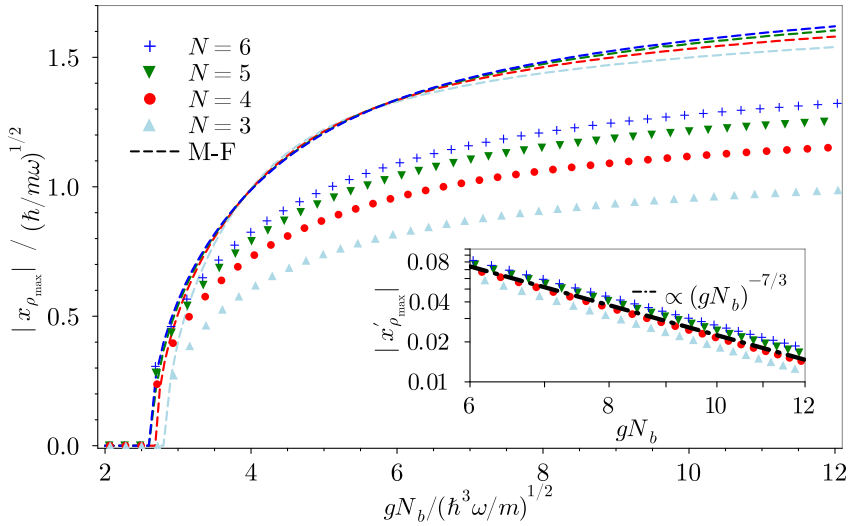

Figure 3.14: Position of the maximum impurity density as a function of gN_b. The markers correspond to numerical results obtained with ED, whereas the dashed lines correspond to MF solutions. The inset shows the derivative of $x_{\rho_{\max}}$ with respect to gN_b in a double logarithmic scale. The dash-dotted line in the inset is an eye guide that shows the power law of the derivatives.

mean-field provides a qualitatively correct description of the state, where the bath remains in the center and the impurity goes at the edges of the trap.

In the infinite interacting limit, the densities derived from the ansatz show a qualitative agreement with our numerical results. The bath remains in the center of the trap and the impurity is pushed outside while maintaining a significant density overlap. We also observe that the ansatz works better for a small number of particles, with almost identical densities for $N = 3$.

As we explained, the impurity for weak interactions has the maximum density at the center of the trap, but at a finite interaction, it develops a two-peak structure, where the maximum is in a finite position. In Fig. 3.14, we show the position of the impurity density maxima as a function of the interaction strength for different numbers of particles. Because of the universality of the single-particle model, expressed through gN_b, we use this effective interaction to compare the different values of N. As the density is symmetric, we only rely on the absolute value of the maximum position, but take care to note that there exists another peak. To ensure completeness, we add the results obtained with the exact diagonalization and compare them with the mean-field approach calculations.

We obtain two different regimes, when the maximum impurity density is at the center of the trap and when there are two peaks. As we described, the first regime corresponds to the weak interaction regime, and the second one appears for an intermediate interaction

strength and continues up to the infinite interacting limit. We refer to the first case as the miscible phase whereas the second one corresponds to the immiscible phase. We obtain a sudden transition from the miscible to the immiscible phases at a given interaction strength g^*, where $x_{\rho_{\max}}$ shows a discontinuity in the derivative.

The critical point g^*N_b shows a weak dependence on the number of particles N, but it seems to converge as the number of particles increases. For the largest baths we have computed using exact diagonalization, we obtain a critical point $g^*N_b \approx 2.5\sqrt{\hbar^3\omega/m}$. Therefore, the impurity exhibits a universal transition between the miscible and the immiscible phases.

With the mean-field approach, we captured the transition, obtaining a compatible value of the critical interaction g^*N_b. Using our self-consistent approach, we also obtained the dependence on the number of particles, which is impossible to obtain using the effective single-particle model. Here we also can observe how in the miscible phase the mean-field approach works, and once we transition into the immiscible phase, the mean-field model fails, giving inaccurate values. We can argue that the miscible phase does not have large correlations, and therefore, the mean field is a good model; however, in the immiscible phase, the correlations must be considered, needing to consider a more robust method, such as the exact diagonalization. Specifically, the strong repulsive limit has a particular interest in the study of one-dimensional Bose polarons (Will and Fleischhauer, 2023; Will et al., 2021).

This transition can be understood as a mean-field phase separation between two species (Ho and Shenoy, 1996; Pu and Bigelow, 1998), which provides the reason why our mean-field approach captures the transition point. From an energetic point of view, this transition can be understood as a balance between the interaction and the harmonic oscillator potential. For weak interactions, the ground state has the minimum energy by having all the particles in the minimum of the potential, increasing the energy from the non-interacting case by almost only interaction energy. But at some interaction strength value, it becomes energetically favorable to separate the impurity and the bath to avoid as much as possible the interaction even if it requires increasing the potential energy. Since moving a single particle is less energetic than moving the whole bath, the impurity goes outwards.

As a crosscheck, in the inset of Fig. 3.14, we show the derivative of the position of the impurity density maximum for the immiscible phase. We find a power law decay of the derivative, with exponent $\sim 1/(gN_b)^{7/3}$, indicating that the position of the impurity density maximum saturates. It is further evidence that the state saturates for the infinite interaction limit, not only the energy but also the density. Of course, the value where $x_{\rho_{\max}}$ saturates depends on the number of particles. We also found (even if it is not shown) that the mean-field results saturate, with a derivative power-law $\sim 1/(gN_b)^{10/3}$, but the results obtained in that limit with this method are not a good estimate.

3.4 Conclusions

In this Chapter, we have presented a study on few-particle systems in a harmonic oscillator trap with contact interaction. We have studied systems with distinguishable particles, starting by analyzing the symmetric $SU(N)$ configuration, which is experimentally feasible using high-spin particles, with one particle per spin projection. In the symmetric case, we examined the energy spectrum as well as the density, crosschecking our results with the analytical solutions where they exist.

We then explored non-symmetric interaction configurations, providing an explanation of the ground state in the infinite interacting limit for non-trivial configurations formed by four particles. These systems were studied using the density and pair correlations, allowing us to describe how particles correlate with one another even in the absence of direct interaction.

With this information, we further examined the energy spectrum as a function of the interaction strength turning on interactions sequentially. We discussed the impact of correlations between particles on the energy gain as additional interactions were introduced: energy increases significantly if particles were previously correlated, while it remains almost constant if they were anti-correlated.

Finally, we explored in detail the case of an impurity, a specific configuration, exploring the energy spectrum as well as the density. In the impurity case, we also considered more particles, up to eight. We used two support methods: a mean-field approach and an ansatz for the infinite interaction limit. We interpreted the system as an effective system where the impurity is immersed in a double-well potential, where the central barrier is created by the rest of the particles. We found two phases, a miscible phase, where the impurity remains in the center of the trap, and an immiscible phase where the impurity is repelled at the edges.

4

FRACTAL LATTICE

Fractals are fascinating structures with unique properties, such as an infinite perimeter (Mandelbrot, 1967) or a non-integer dimension (Gefen et al., 1980). Fractals can be defined as self-similar constructions repeated at different scales. There are many well-known fractal structures, and here, we focus on the study of the Sierpiński gasket while also considering the Sierpiński carpet, formed by triangles and squares, respectively. The fractal Hausdorff dimension, d_f, was introduced to characterize fractals by quantifying how the area of the structure scales with the length.

Fractal systems have been largely studied in the 20th century, with an extensive study on classical diffusion since the 1980s (Alexander and Orbach, 1982; Gefen et al., 1981, 1983; Havlin and Ben-Avraham, 1987; Rammal and Toulouse, 1983). Then, a sub-diffusive behavior was found with a diffusion exponent $\alpha = d_s/d_f$, where d_s is the spectral dimension. The spectral dimension considers the fractal lattice's connectivity, unlike the fractal dimension, which relates to the area growth. According to the Alexander-Orbach conjecture (Alexander and Orbach, 1982), the spectral dimension has a universal percolation threshold at $d_s = 4/3$. With random fractals, one can tune both dimensions independently, and the spectral dimension has been shown to be relevant in the context of quantum transport (Kosior and Sacha, 2017).

Recent advances in the engineering of quantum systems have driven quantum technology applications. Different experimental platforms allow for the design and control of completely artificial quantum systems. Numerous studies in quantum physics extend beyond standard geometries, exploring quantum particles in fractal lattices, with various setups. For example, using photonic systems of coupled optical fibers (Biesenthal et al., 2022; Xu et al., 2021), electronic systems generated by molecular assembly (Shang et al., 2015), and scanning tunneling microscopy (Kempkes et al., 2019), or cold atoms in optical tweezers (Tian et al., 2023). The effects of fractal geometry on the dynamics of quantum systems have garnered considerable attention, revealing notable results even in single-particle systems. Several studies based on fractal geometry and topology have been conducted (Brzezińska et al., 2018; Fremling et al., 2020; Iliasov et al., 2020; Ivaki et al., 2022; Li et al., 2022; Manna et al., 2020, 2022a,b; Pai and Prem, 2019). In addition, there are studies considering Bose-Einstein condensates (Koch and Posazhennikova,

2024), or Ising model (Xu et al., 2017b; Yi, 2015) in a fractal lattice,

In recent years, the experimental realizations of quantum systems on fractal geometries have been possible using photonic waveguide arrays (Biesenthal et al., 2022), where they studied the transport properties (Xu et al., 2021). In that last experiment, they reported a sub-diffusive transport for both the Sierpiński gasket and carpet diffusion exponent $\alpha = d_f$, where d_f is the Hausdorff dimension of the fractal. The transport they reported is slower than the one of a planar Bravais lattice (Razzoli et al., 2020; Tang et al., 2018), where the transport is ballistic with $\alpha = 2$. However, the super-diffusive transport they reported for the fractals seems to be in contradiction compared to the large return probability and the expected localization effect of the fractals (Darázs et al., 2014).

In this Chapter, we begin by analyzing the properties of the fractal under consideration, the Sierpiński gasket and Sierpiński carpet, respectively in Section 4.1. Later, in Section 4.2, we introduce a single particle into the fractal and we study its motion in the Sierpiński lattice. We also compare the effect of the transport exponent on both lattices. Additionally, we study the energy spectral properties, such as the integrated level spacing, which allows us to connect it with the transport properties. In Section 4.3 we study several variations of the lattice, including interpolation from the fractal to the standard lattice and the introduction of a disorder potential. After that, we study the memory effects of the Sierpiński gasket, where we explore dynamics with a non-classical initial state. We extend our study in Section 4.4 by adding a second particle and considering interactions. In this system, we explore how transport is influenced by the interactions, as well as the entanglement between the particles, and how it can be disrupted by measurements. Finally, in Section 4.5, we summarize and present the main conclusions of the Chapter.

4.1 Sierpiński fractal lattice properties

Here, we concentrate on Sierpiński fractals, specifically the Sierpiński gasket, which is created by triangles. We also complement the study by including some results from the Sierpiński carpet, which is created by squares. In Fig. 4.1(a,b) we show the creation procedure of these fractals including the first generations.

The fractal Hausdorff dimension indicates how the area grows with the length of the fractal,

$$S = L^{d_f} \,, \tag{4.1}$$

where S is the surface area, L is the length and d_f is the fractal dimension. For the gasket, when we increase the generation, the length is doubled, but the surface increases three times. Therefore, the fractal dimension is $d_f = \log(3)/\log(2) \approx 1.585$. Similarly, for the carpet, to create a higher generation, the length must be multiplied by three, but the surface area grows eight times, resulting in $d_f = \log(8)/\log(3) \approx 1.893$ (Gefen et al., 1980).

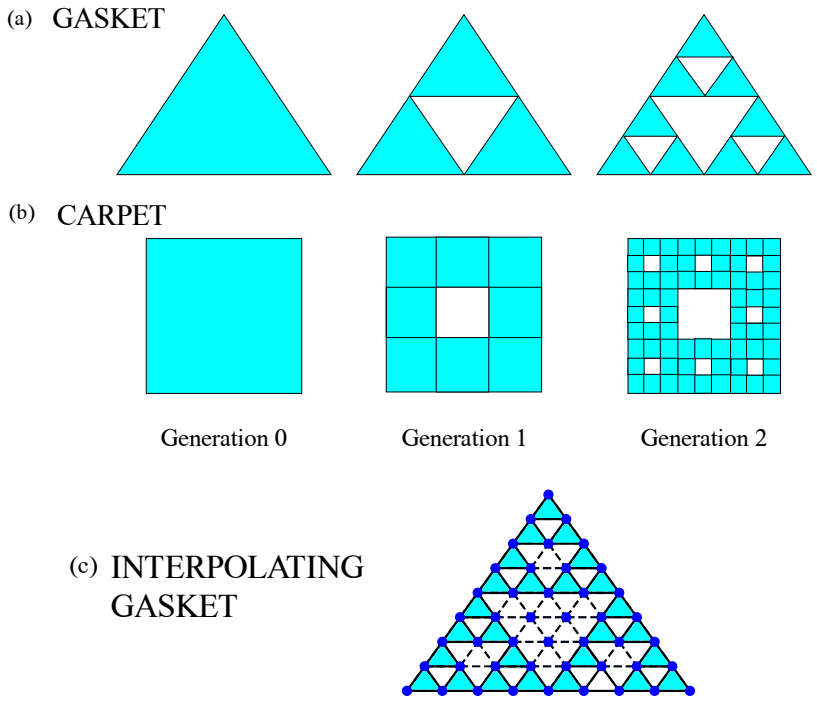

Figure 4.1: Scheme of the fractal structures. Panel (a) corresponds to the Sierpiński gasket and panel (b) corresponds to the Sierpiński carpet at different generations. In all cases, the white regions correspond to a void area, while the light blue regions represent the fractal surface. In panel (c) we plot an interpolated lattice, where the solid lines represent generation 3 of the Sierpiński gasket, and the dashed lines interpolate between the fractal gasket and a regular triangular lattice. The background color is maintained for better identification of the fractal.

An interesting study of fractal systems is how particles move across non-standard regions. A simple way to characterize particle movement is by computing the mean square displacement, $\mathrm{MSD}(t)$, from the initial position and its dependence on time scaling. Assuming that the MSD follows a power-law dependence on time, we can propose a function

$$\mathrm{MSD}(t) \sim t^{\alpha}\,, \tag{4.2}$$

where depending on the power exponent α, we can identify the kind of particle transport. Diffusive transport is defined by $\alpha = 1$, whereas for $\alpha = 2$, the transport is ballistic. Transport is sub-diffusive for $\alpha < 1$, and hyper-ballistic for $\alpha > 2$. The intermediate regime, $1 < \alpha < 2$, is called either super-diffusive or sub-ballistic. Classical systems exhibit a sub-diffusive behavior with $\alpha = d_s/d_f$, where d_s is the spectral dimension. For Sierpiński fractals, the values $d_s = 2\log(3)/\log(5) \approx 1.365$ and $d_s \approx 1.805$ have been obtained for the gasket and carpet, respectively (Darázs et al., 2014).

Quantum transport in the Sierpiński gasket has been compared to the classical random walk (Darázs et al., 2014). One can compare the return probability, i.e., the probability

of finding the particle on the initial site, of a quantum system to that of the classical random walk. The classical return probability decay as $t^{-d_s/2}$ compared to the quantum one, which oscillates and is always above the classical value. This is not the case for finite Sierpiński carpets, indicating clear differences with the gasket (van Veen et al., 2016). The differences can be interpreted geometrically, where the Sierpiński carpet has an infinite ramification number whereas the gasket is finite (Gefen et al., 1984). The ramification number counts the number of bonds that have to be cut to separate different fractal generations.

The increased return probability obtained in the Sierpiński gasket compared to a classical random walk is indicative that localized states exist. These localized states were found in Domany et al. (1983) using the Migdal-Kadanoff decimation technique and were conjectured that all the quantum states are exponentially localized with similar spectral properties to 1-dimensional quasi-crystal (Aubry and André, 1980; Kohmoto et al., 1983). Similar to a disordered system or quasi-crystals, the absence of Bloch theorem can create a quantum interference effect slowing the motion and possibly leading to Anderson localization (Anderson, 1958). However, it has been found that the Sierpiński gasket also has an infinite number of extended states (Wang, 1995), creating a more complex behavior.

In random matrix theory, it is known that the spacing between adjacent energy levels is related to the dynamics of a quantum system (Haake, 2006). In addition, ergodic systems have level-repulsion, and as a consequence, the level spacing distribution $p(s)$ shows a power-law behavior $p(s) \sim s^{\beta}$ for $s \to 0$, where s is the energy gap of consecutive levels. This property allows to classify systems according to their exponent β. For the fractal case, the level spacing study presents some issues because of the large degeneracies in the energy spectrum (Pal and Saha, 2018). For that reason, the level spacing distribution must be redefined for degenerate Cantor spectrum (Fleischmann et al., 1995; Geisel et al., 1991; Sire et al., 1993), obtaining an inverse power law $p(s) \sim s^{-\beta}$. To test this behavior, one can compute the integrated level spacing distribution

$$p_{\text{int}} = \int_s^{\infty} p(s')ds' \,, \tag{4.3}$$

which counts the number of gaps larger than s. In a finite system, it can be described by a power-law

$$p_{\text{int}}(s) \sim s^{1-\beta} \,. \tag{4.4}$$

The exponent β of the level spacing distribution, a static property, and the exponent α from the mean square displacement, a dynamic property, can be related using scaling arguments as in Fleischmann et al. (1995); Geisel et al. (1991).

By definition, the integrated level spacing distribution counts the number of states that can be energetically resolved with an energy s. On the other hand, the volume of the system scales with length according to the (fractal) dimension as L^{d_f}, and so, $L^{d_f} \sim p_{\text{int}}(s)$. Using the previous result, we relate the length of the system with the energy resolution gaps, $L \sim s^{(1-\beta)/d_f}$. At the same time, we have the relation between

the mean square displacement and the time $\mathrm{MSD} \sim t^{\alpha}$, allowing us to relate the distance with the time $L \sim t^{\alpha/2}$. The smallest energy scale is related to time via $s \sim t^{-1}$, and with all of that, we have $L \sim s^{-\alpha/2}$. Combining both expressions, we derive the relation between the exponents α and β

$$\alpha = \frac{2\,(\beta - 1)}{d_f}\,. \tag{4.5}$$

This relation allows us to connect the dynamics of the system with static properties.

The Sierpiński gasket exhibits different transport behavior than a regular triangular lattice. We know that the regular lattice has a ballistic transport, which is in contrast with the results we obtained for the fractal geometry. In addition, Eq. (4.5) is not valid for the regular geometry. For this reason, we consider intermediate systems by interpolating between the fractal and the regular geometries by having intermediate connections as illustrated in Fig. 4.1(c).

4.2 One particle evolution in a Sierpiński lattice

Now, our goal is to simulate transport on fractal lattices and compute spectral properties, such as the integrated level spacing. With both calculations, we can obtain the characteristic exponents α and β and we are able to crosscheck Eq. (4.5). First, the Hamiltonian we are dealing with can be modeled in the second quantization as

$$\hat{H} = -J \sum_{\langle i,j\rangle'} \hat{a}_i^{\dagger}\hat{a}_j\,, \tag{4.6}$$

where $\langle i, j\rangle'$ denotes the nearest neighbors allowed by the fractal lattice. This Hamiltonian not only excludes the sites out of the fractal but also excludes the links that cross non-fractal regions. The tunneling rate J is the energy unit of our system, and the operators $a_i^{\dagger}$ (a_i) are the creation (annihilation) operators for site i.

To obtain the time evolution, since the Hamiltonian is time-independent we can expand the initial state in the eigenbasis of the Hamiltonian and evolve each component with its corresponding energy,

$$|\Psi(t)\rangle = \sum_i \langle \Psi(t=0)|\phi_i\rangle \mathrm{e}^{-iE_i t/\hbar}|\phi_i\rangle\,, \tag{4.7}$$

where $|\psi_i\rangle$ are the eigenstates with eigenenergies E_i. To use this procedure, we need to obtain all the eigenstates of the system, which implies diagonalizing the whole Hamiltonian. For this reason, our time-dependent calculations are restricted to the maximum generation we can compute. We work with systems up to the seventh generation of the Sierpiński gasket and the fourth generation of the Sierpiński carpet.

In Tab. 4.1 we show the dimension of the Hilbert space for a single particle across

	Gasket							Carpet			
$G(i)$	1	2	3	4	5	6	7	1	2	3	4
D	6	15	42	123	366	1095	3282	16	96	688	5280
L/a	2	4	8	16	32	64	128	3	9	27	81

Table 4.1: Hilbert dimension D, and the length of the basis L as a function of a Sierpiński gasket and Sierpiński carpet generation $G(i)$. The length is normalized with the distance between the first neighbor sites a.

different generations of both fractals we are studying. As we only consider one particle, the Hilbert space coincides with the number of lattice sites. We also show the length of these fractals.

4.2.1 Anomalous transport

Here, we study the mean square displacement of a particle initially prepared on a single site of a Sierpiński gasket. In Fig. 4.2 we show the MSD as a function of time for different Sierpiński gasket generations, from the fourth to the seventh.

First, we study the case of preparing the particle in a corner. In this case, we explore the effects for different generations by examining the $\mathrm{MSD}(t)$ of the fractal lattice in Fig. 4.2(a). There, we also compare it with the results of a classical random walk, obtaining a completely different behavior across all the time scales. For the quantum particle, we identify three different time regimes in MSD.

For short times, $tJ/\hbar \lesssim 1$, the system is ballistic, $\mathrm{MSD}(t) \sim t^{\alpha}$ and $\alpha \approx 2.1$. In this regime, the particle has no sense of fractal geometry yet and behaves as if it were in a regular lattice. Although we have obtained a hyper-ballistic exponent, this is due to the initial preparation in a corner. The same exponent is observed for short times even in a regular lattice.

For intermediate times, $1 \lesssim tJ/\hbar \lesssim TJ/\hbar$, we obtain a sub-diffusive regime with $\alpha \approx 0.56$. The boundary time is defined as

$$T = (L/a)^{d_f}\hbar/(4J)\,, \tag{4.8}$$

where L the length of the system, a the distance between first neighbors, and J the tunneling rate. Note that the duration of this regime depends on the size of the system, indicating that for larger generations, this regime lasts longer. We also find that the exponent α depends on the initial configuration, i.e., where the particle is localized at $t = 0$. However, in all cases, the behavior remains sub-diffusive.

For long times, $tJ\hbar \gtrsim TJ/\hbar$, we observe an extremely slow evolution, with $\alpha \sim 0.15$, as shown in Fig. 4.2(b). This regime can be considered a quasi-localized regime, despite its slow evolution. We have obtained the exponent for the largest Sierpiński gasket

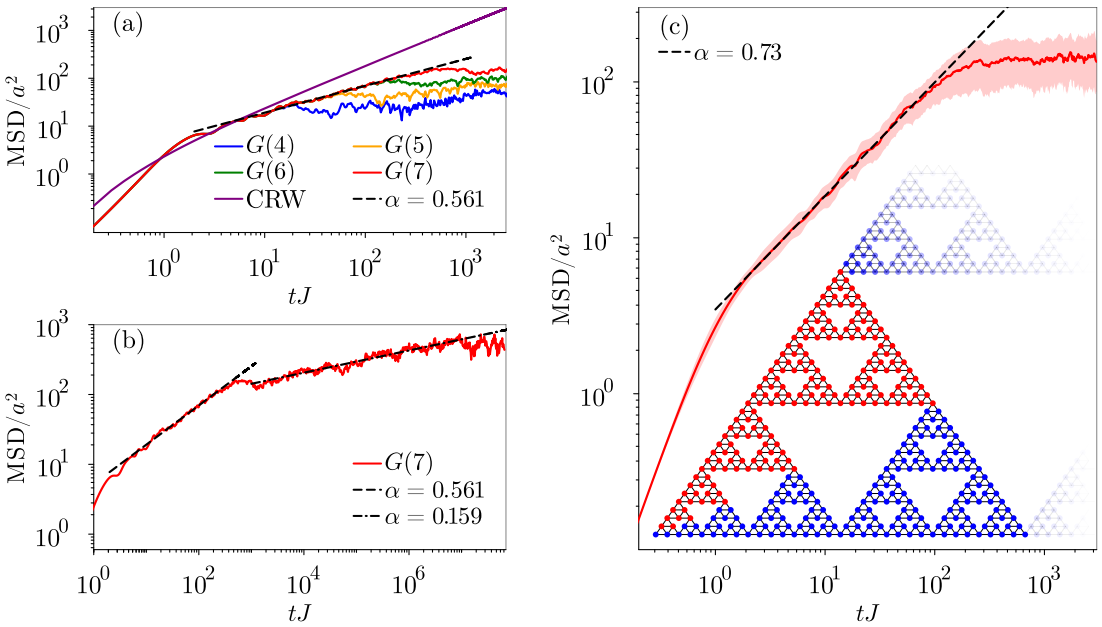

Figure 4.2: Mean square displacement as a function of time for a particle in a Sierpiński gasket. Panel (a) corresponds to the case where the particle starts from one corner of a Sierpiński gasket of generation $G(X)$ with $X = 4, 5, 6, 7$. We also include the results of a classical random walk (CRW) on a $G(7)$ gasket. Additionally, there is a tendency line Eq. (4.2), with a fitted exponent $\alpha = 0.561 \pm 0.005$ obtained on the region $1 \lesssim tJ/\hbar \lesssim TJ/\hbar$ for the $G(7)$ gasket, with T defined in Eq. (4.8). Panel (b) corresponds to the case for the $G(7)$ gasket on a long-time scale. We show two tendency lines, one for the intermediate times $1 \lesssim tJ/\hbar \lesssim TJ/\hbar$ with the same exponent as in panel (a), and the other for long times $tJ\hbar \gtrsim TJ/\hbar$ with a fitted exponent $\alpha = 0.159 \pm 0.003$. Panel (c) corresponds to the averaged mean square displacement $\mathrm{MSD}(t)$ as a function of time for different initial conditions on a $G(6)$ gasket. The initial sites considered are the red ones in the panel, obtaining the average and the variance of the $\mathrm{MSD}(t)$. We also show a tendency line with a fitted exponent $\alpha = 0.73 \pm 0.01$.

generation we can handle. However, the behavior does not depend on the size of the fractal. We assume this regime also exists for larger generations with a similar exponent.

We found that a particle in a fractal lattice is always evolving and increasing the mean square displacement, even when finite size effects play a role. Moreover, the value of the MSD during the transition, i.e., at $t \approx T$ is still far from the thermalized value. A thermalized system has the wavefunction spread all around the lattice with the same probability in each site. This situation implies that the center of mass of the system is at the center of the triangle. Therefore, for the case where the initial system is prepared with the particle in the corner, the mean square displacement of the thermalized system is $\mathrm{MSD}_{\mathrm{th}} = L^2/3$, where L is the length of the triangle basis. Our results show that the system does not thermalize in the intermediate region, and then, with the slow evolution of the long-time regime, the system cannot

thermalize. Note that in Fig. 4.2(b) we show a long time evolution, up to $tJ/\hbar = 10^6$, i.e. a time scale beyond experimentally realistic values. Even on this time scale, the displacement of the particle remains much below the thermalized value, obtaining $\mathrm{MSD}/a^2 < 1000$ but the thermalized value is $\mathrm{MSD}_{\mathrm{th}}/a^2 = 5461$ with $L = 128$ in the reported case. Although we cannot definitively rule out thermalization for a longer time, it becomes difficult to simulate due to numerical precision errors. However, it is possible to argue rigorously that the system does not thermalize in the thermodynamic limit.

It is interesting that $\mathrm{MSD}(T)$ scales sub-linearly with the system size,

$$\mathrm{MSD}(T) \sim T^{\alpha} \sim L^{0.56 d_f} \,. \tag{4.9}$$

In contrast, the thermalized value scales as $\mathrm{MSD}_{\mathrm{th}} \sim L^2$. Consequently, for larger systems, the difference from a thermalized state becomes more pronounced. This implies that fractal geometry has a more significant role in larger generation systems.

In contrast to an infinite Bravais lattice, where all the sites are identical, this is not the case for a finite fractal lattice, where large differences can exist depending on the lattice site. Although all the sites are connected to four others (except the corners that are connected to only two sites), the position with respect the fractal generation bottlenecks has a large impact on the transport properties of these sites. Therefore, we need to complement the previous studies presented in this Chapter, where we have studied the transport of a particle prepared in a corner of the lattice. Here, we consider all the possible initial localized states showed in Fig. 4.2(c) as red dots. The rest of the sites can be mapped to a red one by symmetry. We also exclude the corner initial state in this study. For every initial state, we have computed the mean square displacement as a function of time, and in Fig. 4.2(c) we show the average of the $\mathrm{MSD}(t)$ of all the configurations, with the variance error indicated as a shaded area. With the average $\mathrm{MSD}(t)$, we obtain the three regimes reported before, but now, although the exponent in the short-times remains the same, $\alpha \approx 2$, the value in the intermediate times is slightly larger, $\alpha = 0.73$. We did not compute the exponent of the long-time behavior due to the larger variance in that regime. Alternatively, we computed the exponent for each one of the initial states, obtaining that a generic initial site has an exponent α_i larger than the one obtained for the corner initial case. By averaging over all the exponents, we obtained a similar average value as with the previous averaging method $\alpha' \sim 0.73$. Therefore we have shown that the transport of a particle in a Sierpiński gasket is sub-diffusive in the intermediate time regime.

We have demonstrated the different transport behavior for the Sierpiński gasket compared to the regular triangular lattice. For the regular geometry, the transport is ballistic, exactly as for the initial times obtained in the fractal structure, until it saturates at times $T' \sim L^2$, where the system is almost thermalized, with $\mathrm{MSD}(t)$ oscillating around $\mathrm{MSD}_{\mathrm{th}}$. For the regular lattice, it is already possible to obtain $\alpha > 2$ at short times if the initial state is prepared near a border.

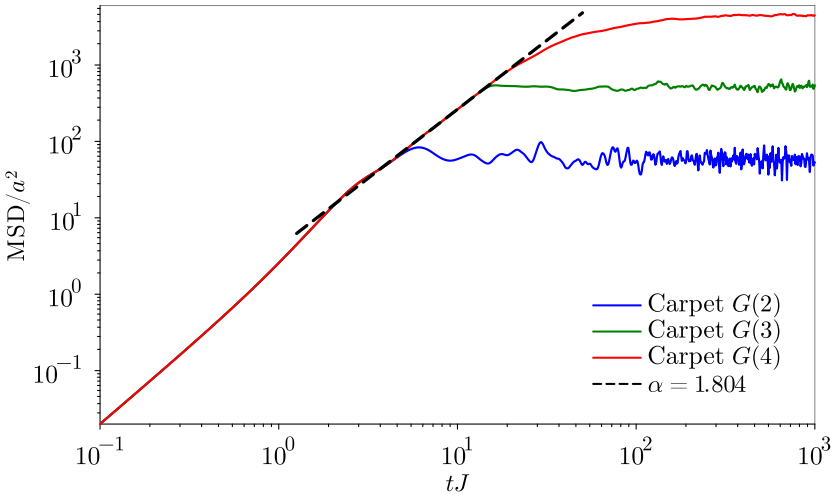

Figure 4.3: Mean square displacement as a function of time for a Sierpiński carpet. We considered the generations $G(2)$, $G(3)$, and $G(4)$. The initial system is prepared with the particle in a corner of the lattice. We show a tendency line in the intermediate region, with a fitted exponent $\alpha \approx 1.804 \pm 0.001$.

A different fractal that we have explored is the Sierpiński carpet, with an example of the creation in Fig. 4.1(b). In that case, we also explore the transport of a particle through this fractal geometry in Fig. 4.3. Similarly to the gasket, the carpet transport presents three regimes. For short times, it is ballistic with exponent $\alpha \sim 2$. Then, there is an intermediate time regime with boundary dependence on the size of the system. And, for a long time, there is a different regime. However, we observe a different behavior compared to the Sierpiński gasket, with an intermediate time regime super-diffusive (or sub-ballistic) with exponent $\alpha \approx 1.804$ contrary to the sub-diffusive regime found for the gasket. The exponent obtained for the carpet is similar to the one previously obtained in Xu et al. (2021), being much larger than the classical value $\alpha = d_s/d_f \approx 0.95$, indicating a quantum speed-up. It is interesting to note that there are some non-Bravais periodic lattices with sub-ballistic quantum transport, for example, the honeycomb lattice with $\alpha \approx 1.71$ (Razzoli et al., 2020).

In Xu et al. (2021), they obtained a super-diffusive behavior for the Sierpiński gasket, in contrast with our sub-diffusive results. This difference is an effect of the definition of the fractal lattice. In their case, all the first neighbors are connected. But in our definition, as shown in Fig. 4.2(c), we only consider connections between first neighbors within the same generation. In this case, the three corners of each generation act as a bottleneck, as the different generations are connected only by these sites. In contrast with Xu et al. (2021), where the connection between different generations is possible through additional tunneling. Even though both lattices have the same Hausdorff fractal dimension, they present different transport behavior. This indicates that the dynamics depends on the connectivity of the lattice. For the Sierpiński carpet, we used the same

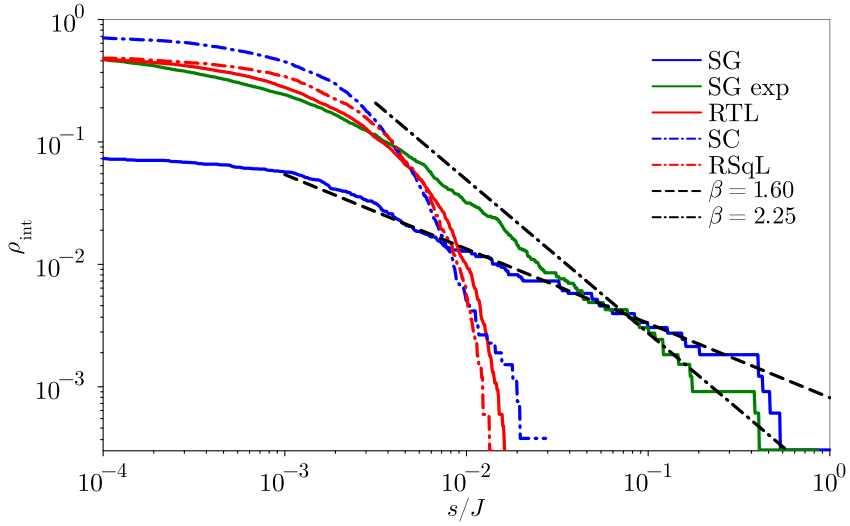

Figure 4.4: Integrated level spacing distribution as a function of the energy gap resolution for the energy spectra on different lattices. Solid lines represent triangular geometries, with the $G(7)$ Sierpiński gasket (SG) in blue, the corresponding regular triangular lattice (RTL) in red, and the Sierpiński gasket used in the experiment of Xu et al. (2021) (SG exp) in green. The dash-dotted lines correspond to square geometries, with the $G(4)$ Sierpiński carpet (SC) in blue, and the regular square lattice (RSqL) in red. We include a tendency line for the gasket (SG and SG exp), with fitted exponents $\beta = 1.60 \pm 0.05$ and $\beta = 20.25 \pm 0.05$ respectively.

lattice with the same connections, and we obtained the same results.

4.2.2 Spectral properties

Here, we are interested in exploring the spectral properties of the different systems studied, such as the Sierpiński gasket and carpet. In particular, we have computed and studied the integrated level spacing distribution $p_{\text{int}}(s)$, Eq. (4.3), which gives the normalized number of energy gaps larger than s. In Fig. 4.4 we show the integrated level spacing distribution as a function of the gap energy for different systems. We observe that for the Sierpiński gasket, there exists a region that fits with a power-law function, $p_{\text{int}} \sim s^{1-\beta}$, as exposed in Eq. (4.4).

Numerically, we have obtained $\beta \approx 1.6$, close to the Hausdorff fractal dimension d_f. The similarity between β and d_f could be a signal that both quantities are equal, but we do not have any a priori argument to ensure this relation. Nevertheless, as exposed in Section 4.1, we relate the exponent of the transport α with the exponent of the spectrum β with Eq. (4.5). Using the values we have obtained with the corresponding error $\beta = 1.60 \pm 0.05$ we expect $\alpha = 0.76 \pm 0.06$, in accordance with the $\alpha = 0.73 \pm 0.01$ we have obtained by averaging over all the different initial configurations, corresponding to Fig. 4.2(c). The error in fitting the β parameter comes from two sources. The most obvious is the numerical error in fitting a numerical dataset. The second one is produced

by the region where one fits the function. As the limits of the power-law behavior are diffuse, and the exponent is sensitive to the boundary, it creates an additional error. For the integrated level spacing distribution of the lattice used in Xu et al. (2021) we obtain that there is also a power-law region but with a different exponent, $\beta \approx 2.25$. With this exponent we obtain $\alpha \approx 1.58$, which is compatible with their reported exponent. This result indicates that if p_{int} can be modeled by a power-law, it is possible to relate the properties of the energy spectra to the transport behavior.

Although we succeded in finding an exponent for the Sierpiński gasket lattices, both ours and the experimental one of Xu et al. (2021), this is not the case for the rest of the analyzed systems. The regular triangular and the regular square lattices present a different behavior compared with the Sierpiński gasket. These regular lattices do not present a region that can be mapped with a power-law, and the results of Fig. 4.4 indicate that there are no large gaps for the regular structures. Note that the regime where we fitted the power-law behavior corresponds to large energy gaps. In contrast, the Sierpiński carpet p_{int} is more similar to the regular geometries than to the Sierpiński gasket. For the carpet, we are unable to find an extended region suitable for fitting a power-law, and therefore, we cannot compare the spectral properties with the dynamics.

4.3 Robustness of the Sierpiński fractal transport

Until here, we have explored the transport of a single particle on a perfect fractal lattice. However, we now consider what might happen if the fractality is not perfect, exploring an interpolation between the fractal structure and a regular one. Another realistic imperfection to consider is a disorder on the lattice, such as having a random potential that introduces detuning at each site. Additionally, we investigate how sub-diffusive transport could be exploited to preserve information.

4.3.1 Transport on interpolating lattices

The results we have obtained for the transport and the dependence on the connectivity, motivate us to explore the interpolation between the Sierpiński gasket and the regular triangular lattice. This interpolation incorporates all the sites corresponding to a regular lattice and introduces two different tunneling ratios. Specifically, we consider the fractal connections with an amplitude J and the regular triangular connections, excluding the fractal ones, with amplitude J'. The scheme of this configuration is represented in Fig. 4.1(c), where the solid lines indicate the fractal connections J, and the dashed lines represent the interpolating connections J'. We define $\gamma \equiv J'/J$ as the interpolating parameter. Using this notation, we can define the Hamiltonian

$$\hat{H} = -J \left((1-\gamma) \sum_{\langle i,j \rangle'} \hat{a}_i^\dagger \hat{a}_j + \gamma \sum_{\langle i,j \rangle} \hat{a}_i^\dagger \hat{a}_j \right) , \tag{4.10}$$

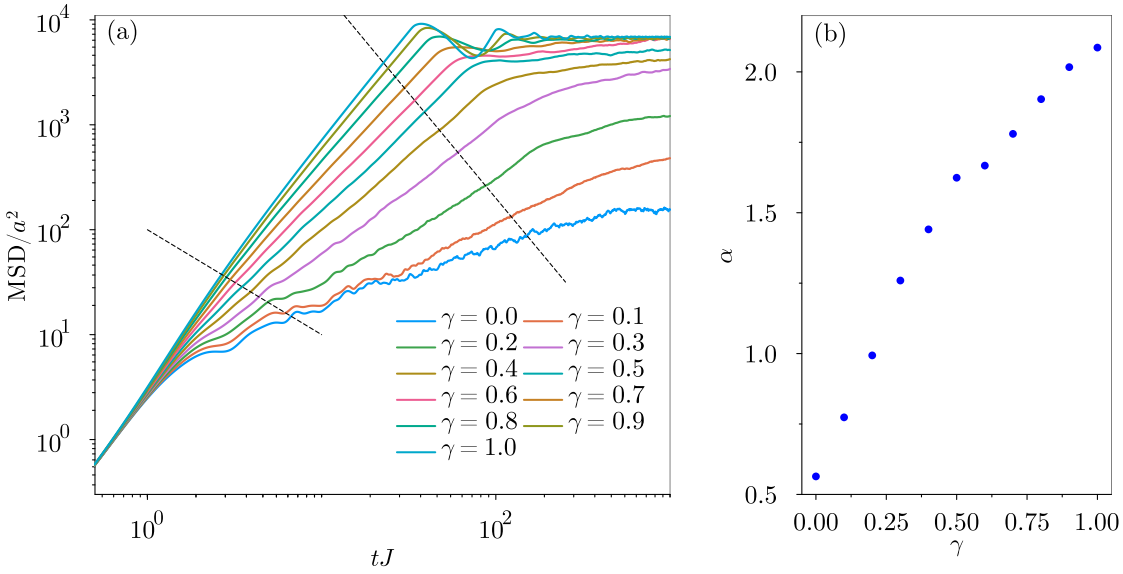

Figure 4.5: Mean square displacement of a particle in an interpolated Sierpiński gasket. Panel (a) corresponds to the mean square displacement as a function of time for a particle in an interpolating lattice, as depicted in Fig. 4.1(c), characterized by the ratio $\gamma \equiv J'/J$ between hopping parameters J' (exclusive to the regular lattice) and J (present in both regular and fractal lattices). We initiate the particle evolution in one corner of an interpolating $G(7)$ gasket. The slowest behavior is obtained in a fully fractal geometry ($\gamma = 0$), whereas the fastest behavior corresponds to a regular triangular lattice ($\gamma = 1$). Panel (b) corresponds to the exponent α of the mean square displacement extracted for different values of γ by fitting the curves from panel (a) within the intermediate regime (as indicated by the dashed lines). The result is plotted as a function of γ.

where $\langle i, j\rangle'$ is the sum over all the first neighbors belonging to the fractal and $\langle i, j\rangle$ corresponds to the first neighbors of the whole regular triangular lattice. It is important to note that the second sum includes all the terms from the first one, so, the first term has the coefficient $(1 - \gamma)$. In our notation, $\gamma = 0$ corresponds to the pure Sierpiński gasket geometry, whereas $\gamma = 1$ represents the regular triangular lattice. The intermediate values $(0 < \gamma < 1)$ correspond to an interpolated lattice. In this study, we do not consider cases with $\gamma > 1$, which would imply $J' > J$.

In order to explore the effect of this interpolation, from fractal to regular geometries, we computed $\mathrm{MSD}(t)$, as shown in Fig. 4.5(a). Similar to the pure fractal case, we observe three regimes. For short times, a ballistic behavior is observed, independently of the interpolation value γ. In the intermediate time regime, we find variations in the exponent and the time intervals where this regime is valid, depending on the value of γ. The long-time regime also shows differences, ranging from the slow evolution typical of the fractal to the thermalization observed in the regular lattice. Our findings suggest that thermalization occurs for interpolated lattices with a coefficient $\gamma > 0.5$ within the time scale of our calculations. Moreover, our results could also be consistent

with thermalization for $\gamma > 0.2$ at larger times.

The intermediate time regime exhibits a smooth transition from the sub-diffusive characteristic of the fractal to the ballistic transport of the regular lattice. In Fig. 4.5(b) we present the exponent α fitted as a function of the interpolation parameter γ. The fitting of the exponent was realized between the two black-dashed lines in Fig. 4.5 that enclose the intermediate regime. We observe that the exponent varies smoothly with the interpolation. For weak interpolation (i.e., $\gamma \lesssim 0.2$), the system exhibits a sub-diffusive behavior, indicating that the fractal geometry is dominant. In contrast, for intermediate interpolation ($0.2 \lesssim \gamma \lesssim 0.8$), the system shows a super-diffusive (or sub-ballistic) behavior, transitioning to the ballistic regime when the system approaches a regular lattice ($\gamma \gtrsim 0.8$).

We have demonstrated that the connectivity plays an important role in the transport properties of a quantum particle on a lattice. We have illustrated how transport can be tuned by interpolating between a fractal geometry and a regular one, enabling a transition from sub-diffusive to ballistic regimes.

4.3.2 Role of disorder

Here, we turn our attention to another perturbation of the Sierpiński gasket, by introducing a disorder, modeled by a random potential on each site i. This random potential is reflected in the Hamiltonian,

$$\hat{H} = -J \sum_{\langle i,j \rangle'} \hat{a}_i^\dagger \hat{a}_j + V_d \sum_i \mu_i \hat{a}_i^\dagger \hat{a}_i \,, \tag{4.11}$$

where V_d is the disorder strength and μ_i are random numbers drawn from a uniform distribution $U(0,1)$ ranging between 0 and 1.

Our goal is to study how this disorder affects the transport properties of a quantum particle. In Fig. 4.6(a), we show the mean square displacement $\mathrm{MSD}(t)$ for different values of the disorder strength. All the cases correspond to an initial preparation of the particle localized in the corner of a $G(5)$ Sierpiński gasket. We have computed the evolution for 100 random samples for each value of V_d and then we have averaged the $\mathrm{MSD}(t)$, with the lines representing the mean and the shaded regions indicating the variance. The effect of the disorder, as one might expect, depends on the strength V_d. For weak disorder, the system exhibits dynamics similar to those of the pure fractal, with only a smoothing effect introduced by averaging over different configurations. This result is useful for experimental purposes because it implies that small perturbations (disorders) do not significantly alter the dynamics of these fractal systems. On the other hand, for extremely large disorders, $V_d \gg J$, the dynamics are slowed, and we observe a saturation at shorter times and small lengths.

In Fig. 4.6(b) we show the saturated MSD ($\mathrm{MSD}_{\mathrm{sat}}$) as a function of the disorder strength

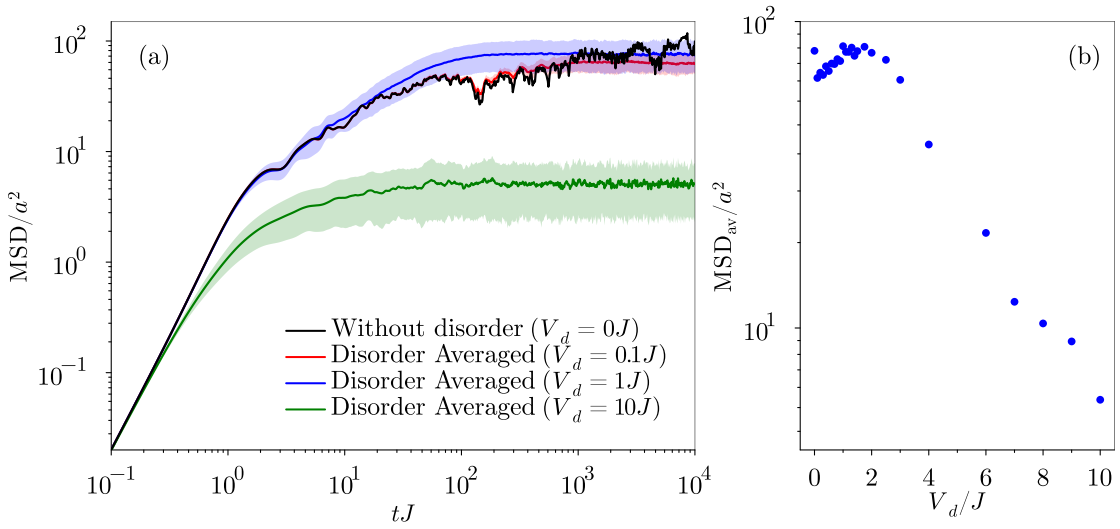

Figure 4.6: Mean square displacement of a particle on a disordered Sierpiński gasket Panel (a) corresponds to the mean square displacement as a function of time for a particle starting from one corner of a $G(5)$ Sierpiński gasket for different disorder strengths, V_d. The solid lines correspond to the average over 100 random configurations whereas the shaded region represents the standard deviation. Panel (b) corresponds to the mean square displacement for long times, $\mathrm{MSD_{sat}}$, obtained by averaging the MSD from $tJ/\hbar = 10^3$ to $tJ/\hbar = 10^4$, as a function of the strength of the random potential, V_d.

V_d. Here we can observe how for weak disorder $V_d \lesssim 2.5J$, there is almost no effect on the dynamics, with $\mathrm{MSD_{sat}}$ remaining similar. But, for larger V_d, the MSD_{sat} exhibits an exponential decay. To interpret this observation, we note that low-dimensional systems (i.e. 1D or 2D systems) are known to localize at any disorder strength, with a localization length that depends on the disorder strength and may exceed the size of a finite system for weak disorders. The behavior seen in the Sierpiński gasket can be interpreted as a competition between two different localization mechanisms. For weak disorder, the localizing effect of the fractal structure is dominant, resulting in minimal effects from the disorder. In contrast, strong disorders produce a localization length that confines the dynamics more strongly than the fractal structure. In this case, the effect of disorder becomes more pronounced in the system evolution.

4.3.3 Localization effects

Now, once we have determined how the transport of a quantum particle is slowed due to the fractality in a Sierpiński gasket with a sub-diffusive transport, we turn our attention to another related effect. Up to now, we have determined the particle distribution by computing the mean square displacement, but we could use other metrics for that. In Fig. 4.7(a) we show the probability of finding a particle in a sub-region. In this case, we prepare the initial state with a particle in the corner. We compare a $G(7)$ Sierpiński gasket with a regular triangle of the same length. The sub-regions correspond to the previous generations of the fractal starting in the initial corner. In Fig. 4.7(b) we show a

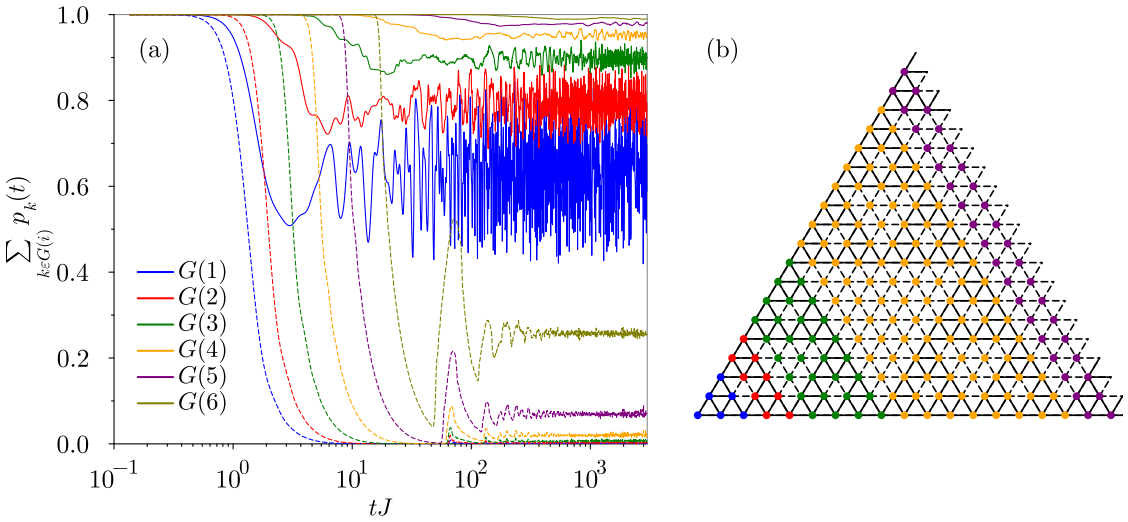

Figure 4.7: Probability of finding a particle in different areas as a function of time. Panel (a) corresponds to the probability of the system having the particle in the sub-regions $G(i)$ as a function of time when the particle starts on the left corner site. The case of a particle in a $G(7)$ Sierpiński gasket corresponds to the solid lines, whereas the regular triangular lattice case corresponds to the dashed lines. Panel (b) corresponds to a scheme indicating the sub-regions with color for better identification of the described cases.

scheme with the same color legend of Fig. 4.7(a) to clarify this situation. For the regular triangular lattice, we use the same nomenclature, but now include all the extra sites and connections, preserving the length of the sub-generations.

One can appreciate that in the case of the regular lattice, the system thermalizes, obtaining almost constant probabilities at long times in each sub-region. Additionally, the probabilities saturate (with small oscillations) around the quotient between the number of sites of the sub-region and the total number of sites. For example, $G(6)$ corresponds to about a one-third of the sites of a $G(7)$ structure, and the long-time probability of finding the particle in a $G(6)$ is about one-third.

The fractal is quite different in terms of the expansion through the different generations. We observe that even for a long time, there is a large probability, about 60%, of finding the particle near the initial corner, in the first generation of six sites. Also, the probability of finding the particle in the surrounding $G(6)$ structure that constitutes about one-third of the total sites is always larger than 95%. This result shows a kind of localization, where the bottlenecks between each fractal generation could play an important role.

With this localization effect in mind, we start to explore how to exploit it. One possibility is to enhance the quantum effects by considering a pure quantum initial state

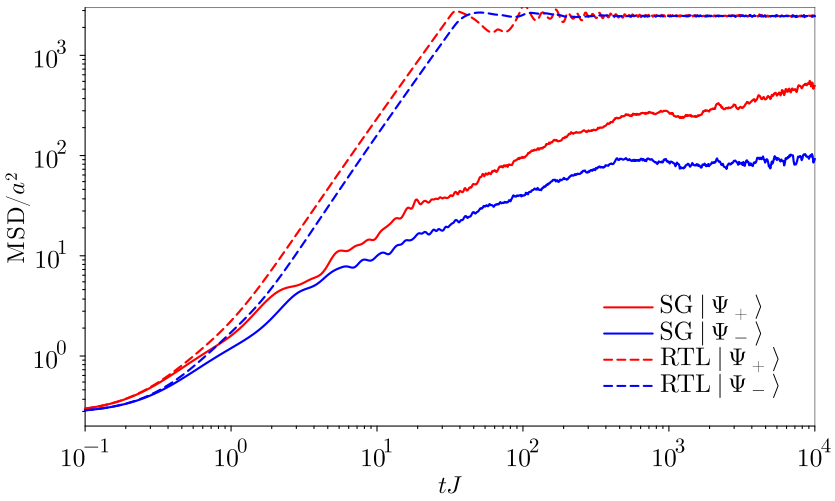

Figure 4.8: Mean square displacement as a function of time of a particle prepared in a non-classical initial state. The particle is in a superposition of being at the corner and one of its first neighbors. The solid red line corresponds to a $G(7)$ Sierpiński gasket with a symmetric initial configuration. The solid blue line corresponds to the anti-symmetric initial condition for the fractal geometry. The dashed lines correspond to a standard triangular lattice geometry with the same basis as the $G(7)$ gasket, where the red and blue colors correspond to the symmetric and anti-symmetric states, respectively.

in a superposition

$$|\Psi_\pm\rangle = \frac{1}{\sqrt{2}}\left(|A\rangle \pm |B\rangle\right) , \tag{4.12}$$

where $|A\rangle$ and $|B\rangle$ correspond to states in a localized sites. We also consider two possible superposition states, the symmetric $(+)$ and the anti-symmetric $(-)$. In our case, we prepare our initial system by choosing $|A\rangle$ as the corner and $|B\rangle$ as one of the first neighbor of $|A\rangle$. We also define the $\mathrm{MSD}(t)$ from the initial position of the center of mass. In Fig. 4.8 we show the evolution of the $\mathrm{MSD}(t)$, where we can see that $|\Psi_-\rangle$ evolves more slowly than $|\Psi_+\rangle$. This is because initially the tunneling from both sites to their common first neighbors is suppressed by destructive interference, while it is constructive in the $|\Psi_+\rangle$ case. This initial suppression of motion persists over time, causing the anti-symmetric state to expand more slowly than the symmetric one.

Even though $|\Psi_-\rangle$ is slower than the symmetric counterpart, there are important differences between the fractal and the regular lattice. In a regular triangular lattice, the system thermalizes for long times, resulting in a uniform probability distribution for finding the particle at each site. This causes the MSD to become constant once the state reaches thermal equilibrium, regardless of the initial phase. Thus, when thermalization occurs, information about the initial phase is lost in terms of particle spread. In contrast, with a Sierpiński gasket, the system does not fully thermalize due to slower evolution and localization effects. The spread of the wavefunction varies depending on the initial phase, allowing distinction of the initial phase by computing the MSD even over long time scales.

Interpreting the two states from Eq. (4.12) as a qubit, and considering slow dephasing noise, it is evident that the information of this qubit could eventually be lost with time. However, as demonstrated, the evolution in the fractal lattice encodes information in the spatial distribution of the wavefunction, which provides some robustness against dephasing noise. This suggests the potential for using such systems as a form of quantum batteries.

4.4 Two interacting particles

Now, we turn our attention to the effects of including a second particle in the system. We consider two scenarios: two identical bosons with contact interaction, where we study the entanglement between two regions of the lattice, and then two distinguishable particles with contact and long-range interactions where we study the entanglement between the particles.

For contact interactions, we consider the Hubbard model (Freericks and Monien, 1994). The interacting part of the Hamiltonian is given by

$$\hat{H}_{\text{cont}} = \frac{U}{2}\sum_i \hat{a}_i^\dagger \hat{a}_i^\dagger \hat{a}_i \hat{a}_i \equiv \frac{U}{2}\sum_i \hat{n}_i(\hat{n}_i - 1)\,, \tag{4.13}$$

where $\hat{n}_i = \hat{a}_i^\dagger \hat{a}_i$ is the number operator that counts the number of particles occupying site i.

On the other hand, for the long-range interaction, we consider a power-law decay of the interaction with an exponent α. To avoid divergence issues, we restrict the long-range interaction to different sites only. Thus, we can implement the on-site interaction as an effective contact interaction. The Hamiltonian then reads,

$$\hat{H}_{\text{l.r.}} = \frac{V}{2}\sum_{i\neq j}\frac{1}{r_{ij}^\alpha}\hat{n}_i\hat{n}_j\,, \tag{4.14}$$

where V is the long-range interaction strength, and r_{ij} is the distance between sites i and j.

Our goal is to study properties such as the entanglement of the two-particle system as a function of time. To achieve this, we use different initial preparations of the system and consider both contact and long-range interactions.

4.4.1 Entanglement

There are several ways to describe an entanglement, such as the entanglement between two regions of the system or between different particles. For single-particle systems, only the first type makes sense. Additionally, in two-particle systems, the interaction plays

an important role, as it can create more entanglement compared to the non-interacting case.

Here, we explore both types of entanglement. First, we compute the bipartite entanglement with two identical bosons. Then, we study how the interactions and time evolution affect the entanglement between two distinguishable particles.

4.4.1.1 Bipartite entanglement

We define bipartite entanglement as the entanglement between two sub-regions of our lattice sites. One approach is to compute the entanglement between the $(N-1)$th fractal generation and the remaining sites in the Nth fractal generation, similar to the probabilities computed in Fig. 4.7. This entanglement is computed using the reduced density matrix. First, we need to trace the density matrix over one of the sub-regions

$$\rho_{\text{red}} = \text{Tr}\left(\rho\right) \ , \tag{4.15}$$

and then obtain the eigenvalues of the reduced density matrix. From these eigenvalues, we compute the Shannon entropy (Shannon, 1948),

$$S = \sum_i \rho_{\text{red}_i} \log\left(\rho_{\text{red}_i}\right) \ , \tag{4.16}$$

where ρ_{red_i} are the eigenvalues of the reduced density matrix.

In Fig. 4.9 we show the bipartite entanglement between a generation of a Sierpiński lattice and the rest of the system. We compare the entanglement production of a two-boson system in a $G(3)$ Sierpiński gasket. We compare different cases, in panels (a) and (b), we have the initial state with both bosons localized in one corner, whereas in panel (c) we have the initial state with one boson in one corner and the other boson in the next neighbor site. In both panels (a) and (c), we compute the entanglement between the sub-region of the first fractal generation, i.e., the six sites next to the corner, and the rest of the system. Finally, in panel (b), we have the same initial condition as in (a), both bosons in the same corner, but now we compute the entanglement between the second generation, i.e., the fifteen sites closer to the corner, and the rest of the system. We study how the entanglement is created for interacting systems, where we only consider contact interaction, studying the effect of the strength of the interaction.

In Fig. 4.9(a) we compare the entanglement production for different interaction strengths with the same initial conditions. For the non-interacting system, we observe that the entanglement saturates for long times, with some oscillations that do not surpass a certain value. This maximum entanglement found here does not correspond to the maximum entropy that the system can reach. When we consider the interaction, then the entanglement creation behaves differently. In the case of interactions of the order of the tunneling rate J, the entanglement production is enhanced. Specifically, for short times, the entanglement is the same as in the non-interacting regime, but when

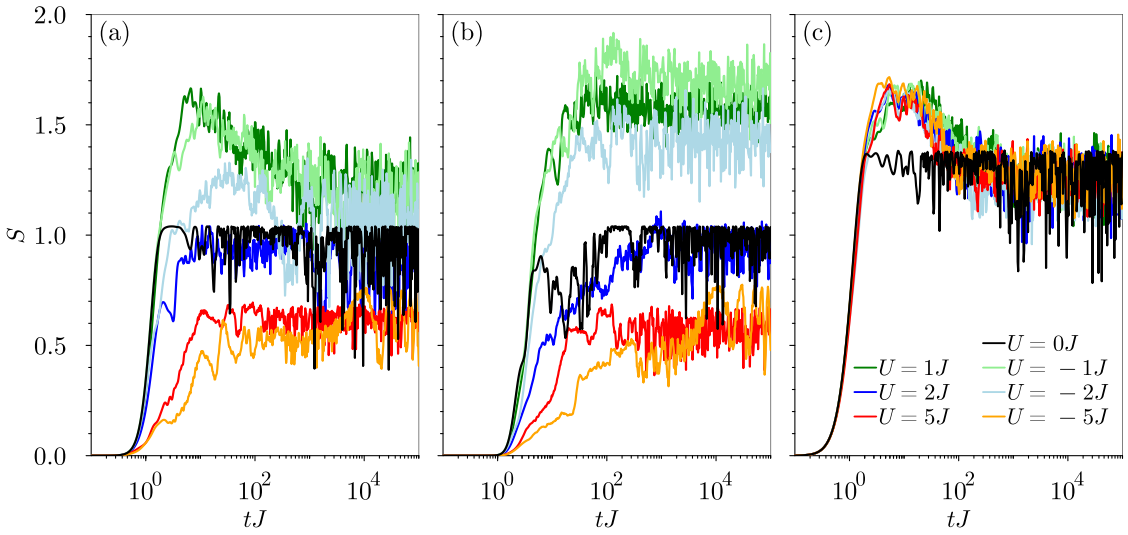

Figure 4.9: Bipartite entanglement as a function of time for a two-boson system with contact interaction in a third generation of a Sierpiński gasket. Panel (a) corresponds to the case where the initial system is prepared with both bosons in the same corner, and the entanglement is computed between the first fractal generation around that corner and the rest of the system. Panel (b) is when the initial system is prepared with both bosons initially in the same corner, and the entanglement is computed between the second fractal generation and the rest of the system. Panel (c) corresponds to the case where the initial system is prepared with one particle in the corner and the other on a first neighbor site, and the entanglement is computed between the first fractal generation and the rest of the system.

the non-interacting case reaches its maximum, the interacting case continues to gain entropy. After that, the entanglement has a maximum and then decreases, but it is always larger than the saturated value of the non-interacting case. We obtain almost the same behavior for $U = \pm J$. The extra amount of entropy in the system can be created by the presence of correlations induced by the interactions.

However, as we increase the interaction, we do not obtain the same behavior as for $U = \pm J$. In particular, for $U = -2J$ we obtain a similar entropy production as for $U = \pm J$, but generating a smaller amount. This is not the case with $U = 2J$, where we obtain behavior more similar to the non-interacting system than to the other cases discussed. It can surpass the non-interaction maximum entropy but remains below it for almost any time. With this result, we observe a difference between the attractive and the repulsive regimes. For much larger interactions, $U = \pm 5J$, we find that the entanglement production is suppressed, needing more time to increase and saturating to lower values than the non-interacting regime. We can argue that when the interaction is much larger and both particles start on the same site, then the system has a large amount of energy, and the particles cannot separate. Thus, the movement is slower, causing the system to start to entangle both parts of the lattice for longer times. In addition, the Hilbert space where the particles behave as one is smaller than the general

case, reducing the amount of possible entropy generated.

All of these effects are enhanced in Fig. 4.9(b), where we are now considering the entanglement between the second fractal generation instead of the first generation. This difference means that the system needs more time to reach the border of the tracing regions, and as a consequence, it needs more time to generate entanglement. Here, we can better appreciate the differences between the interactions $U = \pm J$ and the non-interacting regime. Also, the differences between $U = -2J$ and $U = 2J$ are larger than in panel (a).

In Fig. 4.9(c), we show a different setup, with distinct behavior. The effect of having the particles initially on different sites implies that the energy of the system is almost independent of the interaction strength. In addition, it is faster at gaining entanglement, as one particle is close to the border. The maximum entropy value that the non-interacting system reaches is larger than when both particles start in the same position. When interactions play a role, we obtain an interesting behavior of the entropy generation that is independent of the value of the interaction for $|U| \geq J$. For short times, the amount of entropy created is the same as the non-interacting system, but when the non-interacting case saturates, interacting systems still increase their entropy, reaching a maximum for intermediate times. For long times, the entropy decreases until it reaches the saturated value of the non-interacting case.

4.4.1.2 Entanglement between particles

Another correlation to observe is the entanglement between particles. In that case, when we compute the reduced density matrix, we trace over one particle. For that, we need to have two distinguishable particles to trace over one of them.

As we showed in Section 4.4.1.1, the interaction creates entanglement in the time evolution. Here, we show how, for another type of entanglement, this is still true, and we study this entanglement creation as a function of the initial state and the potential strength.

In Fig. 4.10 we show the entanglement entropy between both particles as a function of time on the x-axis and the interaction strength U of the contact potential on the y-axis. We also compare the generation of entropy in the regular triangular lattice and the Sierpiński gasket fractal. For a non-interacting state, we obtain zero entanglement entropy at any time. When we turn on the interaction, the entanglement is generated quickly until the interaction strength reaches a critical value, at $U \sim 2$. For larger values of the interaction, the system becomes entangled at short times, but then the entanglement decreases compared to lower interaction values. This effect is due to large interactions causing both particles to occupy the same site, leading to a high-energy state and preventing the particles from separating, causing both to evolve as one heavy particle. This situation creates a less entangled system because it has only local correla-

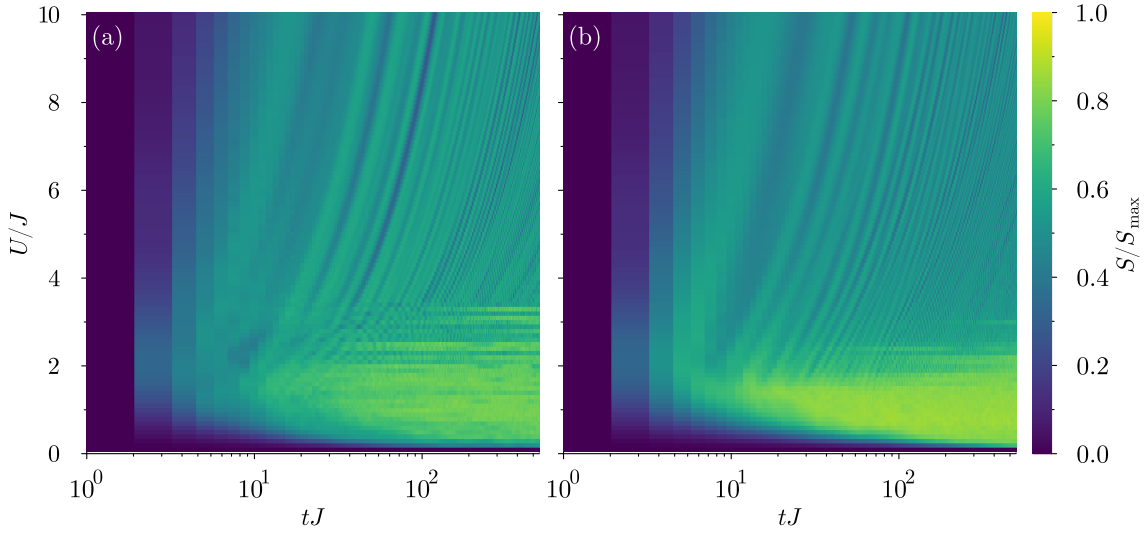

Figure 4.10: Entanglement entropy between two particles as a function of time and the interaction strength. Panel (a) corresponds to a Sierpiński gasket, and panel (b) corresponds to a triangular regular lattice. Both systems have the same basis length. The system interacts via a contact potential, and the initial state is prepared with both particles in the same corner. The entanglement is normalized by the maximum value it can obtain in this situation, which is $\log(N_s)$, where N_s is the number of sites.

tions instead of possible long-range ones.

In this situation, the fractal geometry and the regular one do not exhibit large differences. The main difference lies in the region where we observe the maximum entanglement, which exists for a larger range of interactions. This suggests that for the fractal geometry, the threshold for reaching large entanglement increases.

In Fig. 4.11 we show the entanglement entropy between two particles considering both long-range and contact interactions. We compare the fractal and the regular geometries by considering different signs of the interactions. We used a long-range exponent $\alpha = 1$ as the behavior is the same, with small detail variations with different exponents for the range of parameters examined. We used a third generation of a Sierpiński gasket and the equivalent regular lattice. The initial state is created by localizing both particles on the same corner.

In Fig. 4.11(a), we show the entanglement between two distinguishable particles in a fractal lattice as a function of time. We compare four different cases with different signs, i.e., attractive or repulsive contact and long-range interactions. We have used notably large interaction strengths, but neither in the infinite interacting limit, specifically $|U| = 2J$ and $|V| = 3J$. First of all, we observe that the cases with both interactions being attractive or repulsive ($U > 0$, $V > 0$ and $U < 0$, $V < 0$) have the same behavior, being equivalent at any time. On the other hand, when both interactions have opposite signs, there are two different behaviors. However, in general, the case of different signs

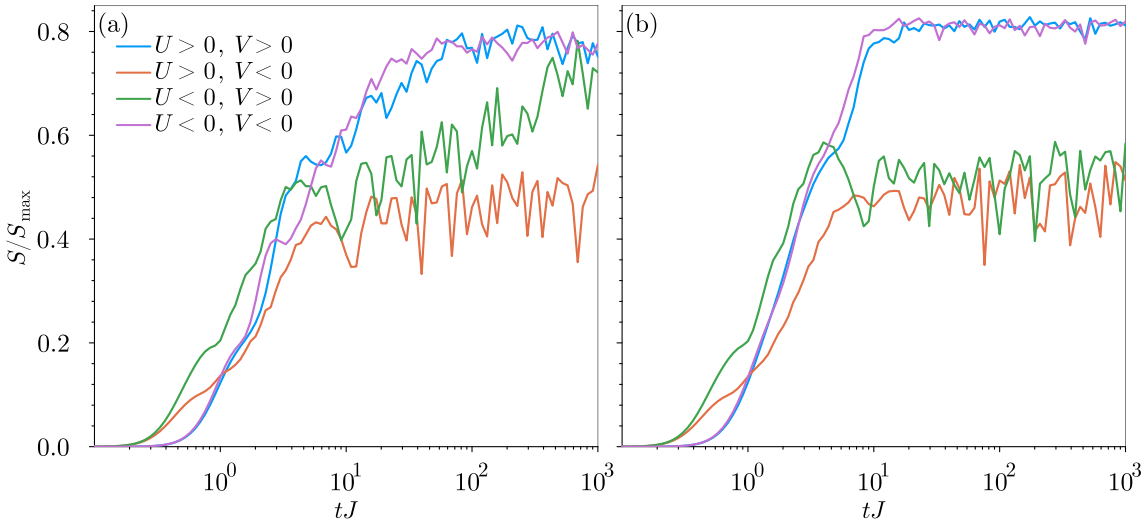

Figure 4.11: Entanglement entropy between two distinguishable particles as a function of time including long-range interaction. We use for the long-range interaction an exponent $\alpha = 1$ with strength V and on-site interaction U. We compare the four cases by changing the signs of the interaction strengths. We used $U = \pm 2J$ and $V = \pm 3J$. The long-range interaction has exponent $\alpha = 1$, but the results are equivalent for different exponents α. In all cases, the initial position is prepared with both particles in the same corner site. Panel (a) corresponds to the evolution of these particles in a $G(3)$ Sierpiński gasket. Panel (b) corresponds to the same entanglement with the same interactions but in a regular lattice with the same lengths as the $G(3)$ Sierpiński gasket.

reaches less entanglement than the case of equal signs.

As both particles are localized initially on the same site, the energy of the system is tuned by the contact interaction strength U. At the same time, the energy associated with the particles localized on nearest-neighbor sites is related to the long-range interaction strength V. Thus, the energy difference between U and V is needed to transition from having both particles on the same site to the particles in the nearest neighbors. This implies that in the cases where the contact and the long-range interactions have different signs, the gap is much larger, avoiding the separation of the particles due to energetic arguments. When both interactions have the same sign, the pair of particles are allowed to spread. This difference can explain the differences in entropy production, as when both particles remain correlated and move together in the same site, then, even if they are correlated and entangled, the Hilbert space where they move is reduced, creating less entropy. When both interactions have the same sign, the particles are still correlated, but with more freedom, allowing them to explore larger Hilbert spaces and reach more entropy.

It is worth mentioning that there are differences between the case of attractive contact and repulsive long-range interactions and the case of repulsive contact and attractive long-range interactions. In particular, the contact interaction strengths are $U = 2J$ and

$U = -2J$, where we also observed a difference between these two values in Fig. 4.9(a-b). It is possible that for larger values, and maybe smaller values such as $U = \pm J$, we obtain the same behavior for both signs.

In Fig. 4.11(b), we show the entanglement for two distinguishable particles in a regular triangular lattice as a function of time. In a similar way to the fractal, the cases with both interactions having the same signs have the same behavior. In this case, as a difference from the fractal case, the entanglement saturates for a finite time. On the other hand, both cases with opposite signs behave equally, without the differences we observe in the fractal. In addition, the entropy in this case also saturates to a smaller value than that obtained with the interactions with the same sign, due to the extra localization effect described previously.

4.5 Conclusions

In this Chapter, we have presented a study on the transport and localization properties of a fractal lattice. We have focused on the Sierpiński gasket, but we also considered the Sierpiński carpet, comparing the transport of a single particle through the system. We have obtained a sub-diffusive transport for the gasket, compared with the super-diffusive transport of the carpet or the ballistic regime of the regular triangular lattice. We also studied the robustness of this transport by adding a random potential. Additionally, we studied the interpolation between the fractal geometry and the standard one by introducing extra connections with an interpolate tunneling ratio. We showed that these extra connections can control the transport regime of the system, ranging from sub-diffusive to ballistic. We also explored the localization induced by the geometry and identified a memory effect. Finally, we have studied a system with two interacting particles, computing correlations via the entanglement entropy, and how it depends on the geometry and the interaction strength.

5

Quantum batteries

One of the main challenges of our time is managing energy, from production to storage. Indeed, our daily lives require a constant supply of energy, whether for lights, home appliances, or transportation such as cars, trains, or planes. Therefore, one of the current challenges is energy storage in batteries, such as those in electric cars. Classical batteries have limitations in terms of charge speed and lifespan, and existing research aims to overcome these issues.

In parallel, we are living in a quantum world, where quantum technologies have increasing importance and presence in our lives each day. Quantum devices also need their own power systems, so, we need batteries for these systems, see more detailed perspective in Auffèves (2022). For these and other reasons, quantum batteries have emerged, trying to overcome these problems. Basically, a quantum battery is a device capable of storing and delivering energy using quantum physics mechanisms, as quantum entanglement (Alicki and Fannes, 2013; Gyhm and Fischer, 2024; Rosa et al., 2020).

The field of quantum batteries is a huge discipline (Deffner and Campbell, 2019; Myers et al., 2022) where the community explores topics such as energy management (Allahverdyan et al., 2004; Andolina et al., 2019; Roßnagel et al., 2016), methods and benefits compared with classical batteries in charge and discharge (Barra, 2019; Binder et al., 2015; Campaioli et al., 2017; Crescente et al., 2020; Deffner, 2021; Kim et al., 2022; Rossini et al., 2020; Song et al., 2024), how to maintain stability (Arjmandi et al., 2023; Carrega et al., 2020; Santos et al., 2019; Yang et al., 2023) avoiding spontaneous discharge due to the quantum recurrence theorem of Poincaré (Bocchieri and Loinger, 1957). In addition, quantum batteries show improvements in the scaling properties of charge with the number of cells (Ferraro et al., 2018; Gyhm et al., 2022).

Nowadays, there are several proposals for quantum batteries such as using superconducting integrated circuits, demonstrated experimentally by Hu et al. (2022) and Gemme et al. (2022). There are theoretical proposals for using micromasers as quantum batteries (Rodríguez et al., 2023; Shaghaghi et al., 2022). Other experimental realizations have been achieved using quantum dots (Maillette de Buy Wenniger et al., 2023), using nuclear magnetic resonance (Joshi and Mahesh, 2022), or organic microcavities (Quach

et al., 2022). Quantum batteries have been achieved at room temperature, first demonstrated by Cruz et al. (2022) using a carboxylate-based metal complex. From the theoretical point of view, several methods have been proposed to exploit a system to create quantum batteries. These methods include collective dark-states (Quach and Munro, 2020), adiabatic evolution (Santos et al., 2019, 2020), Zeno protection (Gherardini et al., 2020), transitionless driving (Moraes et al., 2021), disordered spin systems (Arjmandi et al., 2023; Le et al., 2018; Rossini et al., 2019), a nonreciprocal approach (Ahmadi et al., 2024), qubits into a waveguide (Monsel et al., 2020), systems with noise or imperfections (Ghosh and Sen, De; Zhao et al., 2021), or ultracold mixtures (Konar et al., 2022).

In this Chapter, we present a quantum battery based on a system of ultracold bosons trapped in three adjacent lattice sites. We assume the system to be well described by a three-well Bose-Hubbard Hamiltonian. We propose a setup with a ramping potential, creating a system with different single-particle energies in each well. The setup is experimentally feasible, see a two-well realization with fermions Murmann et al. (2015). The goal of the charging process is to move the particles from the first site, which has the lowest energy, to the third one, which is the most energetic. To induce this motion and simultaneously maintain the stability of the system at the end of the protocol, we use a Spatial Adiabatic Passage (SAP) (Bradly et al., 2012; Menchon-Enrich et al., 2016; Rubio et al., 2016) based mechanism, where the tunneling ratios are different and time-dependent.

The SAP protocol was first proposed by Eckert et al. (2004) and implemented with light beams in coupled waveguides by Longhi (2006); Longhi et al. (2007) and later it was achieved with optical tweezers, see an example in Florshaim et al. (2024). This protocol uses a counter-intuitive coupling application order; i.e., it starts without coupling between the populated state and the intermediate one, while coupling between the target and the intermediate states, and ends with the opposite configuration. There are many studies that use the SAP protocol, some examples can be found in Loiko et al. (2014, 2011); Lunghi et al. (2018); Menchon-Enrich et al. (2012, 2013); Taie et al. (2020) The SAP protocol is a derivation from the Stimulated Raman Adiabatic Passage (STIRAP) used in the quantum optics community (Bergmann et al., 2019; Shore, 2017; Vitanov et al., 2017). Unlike SAP, STIRAP uses internal transitions instead of spatial movement of the particles. Even though the analytical treatment is similar in both cases, the experimental implementations differ significantly in terms of the complexities and parameters involved.

In this Chapter, we start by describing the SAP protocol for a single particle in Section 5.1. Then, in Section 5.1.1, we explore the single-particle case analyzing how the protocol works. In Section 5.2 we study systems with a few particles, introducing the interaction. That section includes the main results of the Chapter. Specifically, in Section 5.2.1, we explore the two-particle battery, including an extensive analysis, with numerical simulations and analytical calculations. We extend the study to more than two particles in Section 5.2.2 where we study the charging process using numerical methods and

develop an effective theory. Finally, we conclude in Section 5.3, summarizing the main results we have obtained.

5.1 SAP protocol

For a single particle inspired by the STIRAP, appears SAP, in which now the particle is moving spatially instead on internal levels. The goal of the SAP protocol is to populate an excited state by passing through an intermediate state without populating it. This is useful when there does not exist a direct way to promote from the initial state to the desired state, but both can be connected through the intermediate state. In addition, if the intermediate state is unstable and has a fast decay rate, then one does not want to populate it. In that situation, the SAP allows, with the appropriate parameters, to overcome this problem. Even though in general this protocol is introduced for single-particle systems, here we use the second quantization formalism. With that formalism, we can add more particles and study the interaction effects.

We model our three-level system, with the Hamiltonian,

$$\hat{H} = \sum_{i=1}^{3} \epsilon_i \hat{n}_i + \sum_{i=1}^{2} \left(\Omega_{i,i+1}(t) \mathrm{e}^{i\omega_{i,i+1}} \hat{a}_i^\dagger \hat{a}_{i+1} + \mathrm{H.c.} \right) , \tag{5.1}$$

where $\omega_{i,j} = \epsilon_i - \epsilon_j$, with ϵ_i the energy of well i, and the operators $\hat{a}_i$ ($\hat{a}_i^\dagger$) are the creation (annihilation) operators. The number operator is defined as $\hat{n}_i = \hat{a}_i^\dagger \hat{a}_i$. This Hamiltonian describes a coupling between the first and second sites and also between the second and the third. For convenience, we define

$$\hat{H}_0 = \sum_{i}^{3} \epsilon_i \hat{n}_i \, , \tag{5.2}$$

which represents the energy due to the population of the sites.

To compute time evolution, it is convenient to move to the interaction picture. In this picture, the Hamiltonian is simplified and explicitly written as

$$\hat{H} = \Omega_{12}(t) \left(\hat{a}_1^\dagger \hat{a}_2 + \hat{a}_2^\dagger \hat{a}_1 \right) + \Omega_{23}(t) \left(\hat{a}_2^\dagger \hat{a}_3 + \hat{a}_3^\dagger \hat{a}_2 \right) . \tag{5.3}$$

Now, the Hamiltonian resembles a Bose Hubbard model without interaction, where Ω_{ij} is the transition ratio between the states ij. Note that this Hamiltonian includes transitions from state 1 to 2 and from 2 to 3 but does not include a direct coupling between 1 and 3. In the single-particle case, this Hamiltonian can be written as a 3×3 matrix, and its analytical instantaneous eigenvalues are,

$$E_0 = 0 \tag{5.4}$$

$$E_\pm(t) = \pm \sqrt{\Omega_{12}^2(t) + \Omega_{23}^2(t)} \equiv \pm \Lambda(t) \, , \tag{5.5}$$

with corresponding eigenvectors

$$|\Psi_0(t)\rangle = (-\Omega_{23}(t), 0, \Omega_{12}(t))\,/\Lambda(t) \tag{5.6}$$

$$|\Psi_\pm(t)\rangle = (\Omega_{12}(t), \pm\Lambda, \Omega_{23}(t))\,/\sqrt{2}\Lambda(t)\,. \tag{5.7}$$

The $|\Psi_0\rangle$ solution is known as a dark state. This state can be used for our goal, by setting the parameters Ω as time-dependent and following the conditions at the beginning of the protocol $\Omega_{12}(t=0) = 0$ and $\Omega_{23}(t=0) \neq 0$, and at the end of the protocol, $\Omega_{12}(t=\tau) \neq 0$ and $\Omega_{23}(t=\tau) = 0$.

One possibility to fulfill these conditions is by taking a simple linear dependence, as follows,

$$\Omega_{12}(t) = \Omega\frac{t}{\tau} \tag{5.8}$$

$$\Omega_{23}(t) = \Omega\left(1 - \frac{t}{\tau}\right)\,, \tag{5.9}$$

where the time goes from $t = 0$ to $t = \tau$.

Of course, any other functions that fulfill the conditions at the beginning and the end of the evolution should also work. In the Section 5.1.1, we explore the effects of different functional forms, but in the rest of the analysis we focus on the linear time-dependent functions Eq. (5.8) and Eq. (5.9).

With the explicit time-dependent Hamiltonian, we can solve numerically the time-dependent Schrödinger equation

$$i\hbar\frac{d|\Psi\rangle}{dt} = H(t)|\Psi\rangle\,, \tag{5.10}$$

where we can introduce $s = t/\tau$, with $0 < s < 1$. With a couple of transformations, we can write the time-dependent Schrödinger equation as

$$i\frac{d|\Psi\rangle}{ds} = \frac{\tau}{\hbar}H(s)|\Psi\rangle\,. \tag{5.11}$$

Noting that H is proportional to Ω, see Eq. (5.3), Eq. (5.8) and Eq. (5.9), our dynamics depend on the product of $\tau\Omega/\hbar$. For this reason, we cannot separate the coupling strength and the duration of the protocol in the time evolution effects. The same effect happens with the interaction strength, introduced in the next section.

5.1.1 Charging the system

To compute the amount of energy gained with the protocol, we define a charge as

$$C = \langle\Psi|\hat{H}_0|\Psi\rangle\,, \tag{5.12}$$

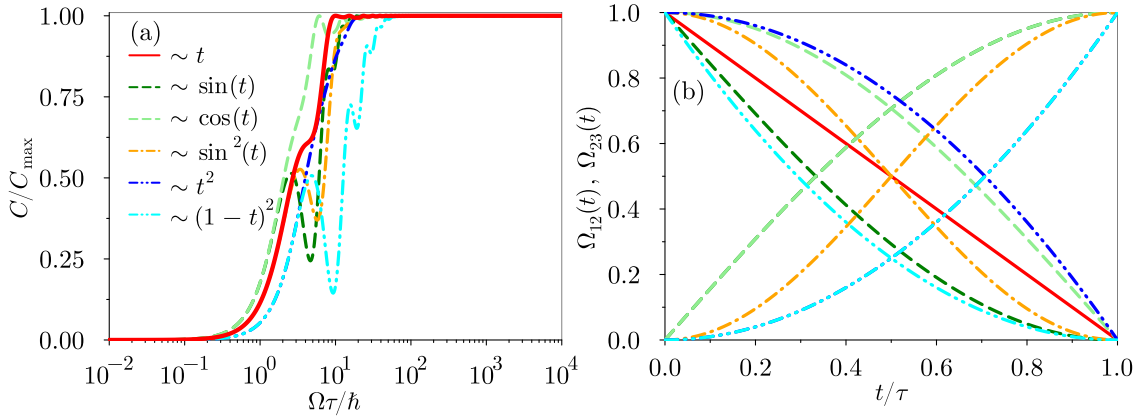

Figure 5.1: Charge of a single particle using a SAP protocol Panel (a) corresponds to the charge of a single-particle system using the SAP protocol as a function of the coupling $\Omega\tau/\hbar$ for different time-dependent functions. Panel (b) is a graphical representation of the time dependence of the coupling for each configuration. The Ω_{12} are those that start at 0 and end at 1, and Ω_{23} vice versa. Some of the Ω_{12} are equal, such as green (dark and light) and blue (dark and light).

where $\hat{H}_0$ is the internal energy levels Hamiltonian of Eq. (5.2). To have some universality criteria, we can define the maximum charge $C_{\max}$ and normalize the charge as $C/C_{\max}$. The maximum value of the charge is given by $C_{\max} = N\epsilon_3$ where N is the number of particles in the system, in the general case.

The case of a single particle with this protocol in the context of a quantum battery has already been explored by Santos et al. (2019). Nevertheless, the protocol can be used as a stable quantum battery with an analytical result. For the protocol to be successful, adiabatic evolution is required. The adiabaticity of the process depends on the parameters used, such as the total time employed and the coupling strength. They show that the protocol is adiabatic for large values of the product of coupling strength and total time.

To understand the performance of the protocol in the single-particle case, we present in Fig. 5.1 the normalized charge as a function of the coupling for one particle under the SAP protocol. We compare the results for several time-dependent couplings indicated in the legend. For simplicity, we neglect the normalization of the time with τ, where t is implemented as t/τ. Also, we do not show explicitly the frequency of the sinusoidal functions, which to fulfill the boundary conditions is $\pi/2$, running the sine from 0 to 1 when the time varies from 0 to τ. The explicit contribution of the coupling strength Ω is not shown, but for all of them, the coupling strength is the same for both couplings.

The functions used are

$$t \begin{cases} \Omega_{12}(t) = \Omega s \\ \Omega_{23}(t) = \Omega(1-s) \end{cases}, \qquad \sin(t) \begin{cases} \Omega_{12}(t) = \Omega \sin\left(\frac{\pi}{2}s\right) \\ \Omega_{23}(t) = \Omega\left(1 - \sin\left(\frac{\pi}{2}s\right)\right) \end{cases},$$

$$\cos(t) \begin{cases} \Omega_{12}(t) = \Omega \sin\left(\frac{\pi}{2}s\right) \\ \Omega_{23}(t) = \Omega \cos\left(\frac{\pi}{2}s\right) \end{cases}, \qquad \sin^2(t) \begin{cases} \Omega_{12}(t) = \Omega \sin^2\left(\frac{\pi}{2}s\right) \\ \Omega_{23}(t) = \Omega \cos^2\left(\frac{\pi}{2}s\right) \end{cases},$$

$$t^2 \begin{cases} \Omega_{12}(t) = \Omega s^2 \\ \Omega_{23}(t) = \Omega\left(1 - s^2\right) \end{cases}, \qquad (1-t)^2 \begin{cases} \Omega_{12}(t) = \Omega s^2 \\ \Omega_{23}(t) = \Omega\left(1-s\right)^2 \end{cases},$$

where $s = t/\tau$.

For all the functions we used in the protocol, we can appreciate that for small values of the coupling $\tau\Omega/\hbar$, the system almost does not charge. On the other hand, for larger values, the system reaches the maximum charge.

For small values of the coupling, i.e. $\tau\Omega/\hbar < 10^{-1}$, there are two possibilities, either a small coupling $\Omega \ll \hbar/\tau$ or a short time evolution $\tau \ll \hbar/\Omega$. In the first case, we can explain that the system remains in the initial configuration because of the probability of having a transition from the first to the second state (and also from second to third) is small enough and cannot occur within the finite time evolution. In the second case, if $\tau \ll 1$, the system remains in the initial state because the short time does not allow the system to evolve sufficiently, even if the coupling has a finite strength.

When the effective coupling becomes $\tau\Omega/\hbar > 10$, then the system reaches the maximum charge configuration, indicating that the particle has transitioned from the initial state to the third one.

The behavior for the limits of the coupling is shared by all the time-dependent functions, but not necessarily the intermediate regions or the minimum coupling where the system reaches the maximum charge. Almost all the functions have similar charging effects. The most different used in that example is the corresponding to $\Omega_{12} = \Omega(t/\tau)^2$ and $\Omega_{23} = \Omega(1 - t/\tau)^2$, as shown in light blue. These functions need a value of Ω almost one order of magnitude higher to reach the maximum charge compared with the other ones.

In general, the function used does not affect the dynamics significantly, or at least, does not change substantially the state obtained at the end of the protocol. For this reason, from now on, all the calculations use linear functions. This choice is made for simplicity more than for any other reason.

5.2 Few interacting particles

Now, we turn our attention to a system populated with more particles. In that sense, it opens the door to the study of the effect of inter-particle interaction (Benseny et al.,

2016; Reshodko et al., 2017). Here, we study a contact interaction, occurring when a pair of particles populate the same internal state. Globally, this system can be viewed as a Bose-Hubbard model with three sites, with time-dependent hopping between the sites, and also a ramping on the energy levels. To obtain the Hamiltonian of the system, we take the Hamiltonian described in Eq. (5.1), we include the interaction term, and write explicitly the time-dependence of the couplings Ω_{ij}. For convenience, we work in the Interaction picture, where the Hamiltonian that governs the time evolution reads

$$\hat{H}(t) = \Omega\left((t/\tau)\hat{a}_1^\dagger\hat{a}_2 + (1-t/\tau)\hat{a}_2^\dagger\hat{a}_3 + H.c.\right) + \frac{U}{2}\sum_{i=1}^{3}\hat{n}_i\left(\hat{n}_i - 1\right) . \tag{5.13}$$

The non-interacting case does not add new physics, due to the rest of the Hamiltonian being a one-body operator. Therefore, the system can be factorized for each particle and the time evolution is just the single-particle evolution.

First of all, we start analyzing the case $N = 2$, where the interaction starts to play a role. We explore the effects of the interaction on the charging, and we can explain certain limits analytically. Then, we continue exploring the case with more than two particles, studying up to six. We follow a similar study methodology. However, for larger systems, the states and the spectra become more complex and it is not possible to obtain an exact analytical solution. For this reason, we work with an effective model inspired by the two-particle solution and supported by the results obtained.

5.2.1 Two particle charging

Here we analyze the charge of a two-particle system. In Fig. 5.2 we show the charge at the end of the protocol ($t = \tau$) obtained by computing the time-evolution for a system of two particles. We show the normalized charge as a function of the coupling and the interaction. We find that the sign of the interaction does not affect the charge at the end of the protocol; only the absolute value of the interaction strength $|U|$ matters.

We can appreciate three different regions depending on the ratio between the interaction and the coupling. The first region we identified is where the interaction is much stronger than the coupling ($|U| \gg \Omega$), in the bottom right of Fig. 5.2 the system remains discharged at the end of the protocol. The second region corresponds to the inverse case, where the coupling is much larger than the interaction($\Omega \gg |U|$), where there are some oscillations on the charge as a function of $|U|$. Finally, the third region is where both terms (coupling and interaction) are comparable, leading to complex charging.

The two first regions, corresponding to both limits, can be analyzed. The case with $|U| \gg \Omega$ is well understood by taking into account energy arguments. As the initial state corresponds to both particles on the same site, then the energy of the system is U. At the same time, the coupling is a single-particle operator and can only connect the

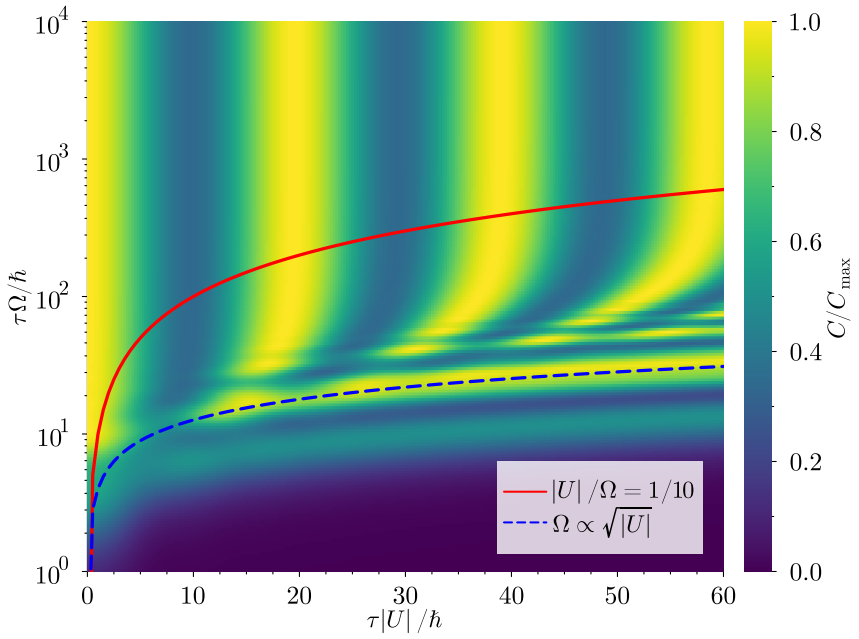

Figure 5.2: Normalized charge at the end of the protocol as a function of the coupling and the interaction at the end of the protocol for the two-particle case. The results are obtained from time-evolution numerical calculations with energy ratios of $\epsilon_1 = 0$ and $\epsilon_3/\epsilon_2 = 1.95$. There are two lines to indicate the behavior of the system in certain regimes.

initial state with a Fock state with one particle at the first site and another at the second. This Fock state is characterized by a state without interaction, and so, the energy of the state is ~ 0. Therefore, the probability of having a transition between two states with a gap $\sim U$ with a coupling $\Omega \ll |U|$ is almost zero. In conclusion, the state remains in the initial state isolated, without the possibility of evolving.

The second limit case, where $\Omega \gg |U|$ is much richer in physics than the previous one. In that limit, we observe an oscillatory behavior of the charge as a function of the interaction $|U|$ that does not depend on the coupling Ω. These oscillations are periodic and their frequency does not depend on the value of the energy of each site. An important point is that these oscillations reach the maximum charge in each period, so, it indicates that one can fully charge the battery for discrete values of the interaction. It can be useful in systems where the interaction exists and can be modulated but without the possibility of eliminating it. In these systems, we show that is possible to charge due to the interaction effect. The minimum of the oscillations depends on the energies of the sites, even if we do not show this in Fig. 5.2. That dependency only takes into account the ratios of the different energies instead of the absolute values.

Of course, there exists another region, the intermediate one, where the coupling and the interaction are of the same order $|U| \sim \Omega$. In that scenario, the system can reach a maximum charge, but as one can expect, the value of the charge depends on both parameters. One zone in that regime with a maximum charge seems to follow

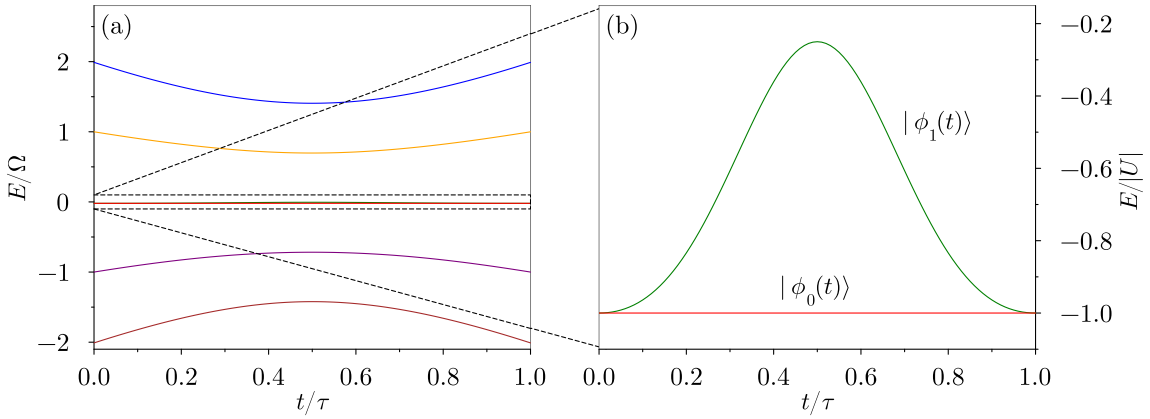

Figure 5.3: Instantaneous energy spectrum as a function of time for the two-particle case. Panel (a) shows all the states, normalized by the coupling Ω, whereas panel (b) shows the central manifold normalized by the interaction strength $|U|$. The energies are computed with attractive interaction, but normalized by the absolute value of it.

a function of the interaction and the coupling. Also, there is a parallel zone without maximum charge, but higher than the surrounding region. We found that these zones follow a function $\Omega \propto \sqrt{|U|}$. However, we do not have a clear explanation for why this is happening, and it requires a much more complex analysis. For this reason, we focus only on the large coupling (or weak interaction) limit, which we are able to explain with a simple effect using an analytical model.

5.2.1.1 Analytical model

In order to understand the physics beyond the oscillations of the charge due to the interaction in the two-particle case, we computed the energy spectrum as a function of time and analyzed it. In Fig. 5.3 we show the instantaneous energy spectrum as a function of time corresponding to our protocol. In panel (a) we show the whole energy spectrum, where there are the six states of the Hilbert space, corresponding to two bosons in three lattice sites. We have two states with energies $E \sim \pm 2\Omega$, two more with $E \sim \pm\Omega$, and the last two with $E \sim 0$. In general, these energies are affected by the time t/τ and the value of the interaction strength U. To be more precise, both states with $E \sim 0$ in the Ω scale have energy $E \sim U$ in the fine structure.

The initial state, with both particles in the first well, corresponds to an eigenstate of the initial Hamiltonian with energy $E = U$. At the same time, the target state, both particles in the third well, is also an eigenstate of the final Hamiltonian with energy $E = U$. As the initial state belongs to the central manifold, we can assume that the system evolves in that manifold in the first approximation. For this reason, we turn our attention to this manifold, shown in Fig. 5.3(b), where we show a zoom on that region, and the energy is scaled by the interaction strength. We can observe a state, we refer to it as $|\Phi_0\rangle$ from now on, with constant energy E_0, and the state is also time-independent

if one computes it. There is another state, we refer to it as $|\Phi_1(t)\rangle$ from now on, with energy time-dependent $E_1(t)$.

The initial state, $|\Psi(t=0)\rangle$, can be expressed as a superposition of $|\Phi_0\rangle$ and $|\Phi_1(t=0)\rangle$ as

$$|\Psi(t=0)\rangle = \sqrt{\frac{1}{3}}|\Phi_0\rangle + \sqrt{\frac{2}{3}}|\Phi_1(t=0)\rangle\,. \tag{5.14}$$

Now, if we let the system evolve, and we suppose an adiabatic evolution because it fulfills the parallel transport condition $\langle\Phi_i|\frac{\partial}{\partial t}\Phi_i\rangle = 0$, and as a consequence, each instantaneous eigenstate evolves with its own phase independently. We can express the state at any time as

$$|\Psi(t)\rangle = \sqrt{\frac{1}{3}}\mathrm{e}^{-i\int_0^t E_0 dt/\hbar}|\Phi_0\rangle + \sqrt{\frac{2}{3}}\mathrm{e}^{-i\int_0^t E_1 dt/\hbar}|\Phi_1(t)\rangle\,, \tag{5.15}$$

where we can rearrange multiplying by an arbitrary phase in order to obtain the state as

$$|\Psi(t)\rangle = \sqrt{\frac{1}{3}}|\Phi_0\rangle + \sqrt{\frac{2}{3}}\mathrm{e}^{-i\int_0^t (E_1-E_0) dt/\hbar}|\Phi_1(t)\rangle\,. \tag{5.16}$$

Now, we have the state as a function of time, but as our protocol has a final, we can compute the state at the end of the protocol, being

$$|\Psi(\tau)\rangle = \sqrt{\frac{1}{3}}|\Phi_0\rangle + \sqrt{\frac{2}{3}}\mathrm{e}^{-i\int_0^\tau (E_1-E_0) dt/\hbar}|\Phi_1(\tau)\rangle\,, \tag{5.17}$$

where the integral can be solved analytically, obtaining

$$\int_0^\tau (E_1(t) - E_0) dt/\hbar = \frac{3(\pi-4)}{8}\frac{U\tau}{\hbar}\,. \tag{5.18}$$

This means that the relative phase induced by the time evolution is proportional to the interaction and the time of the protocol. With these results, one can compute the charge at $t=\tau$, obtaining

$$C = C_{\max}\left[1 - \frac{4(2\epsilon_3 - \epsilon_1 - \epsilon_2)}{9\epsilon_3}\sin^2\left(\frac{3(\pi-4)}{16}\frac{\tau U}{\hbar}\right)\right]\,, \tag{5.19}$$

where we obtain also a periodical oscillation on the charge as a function of the interaction $\tau|U|$, with a constant frequency, oscillating between full charge and a value that depends on the ratios of the energies ϵ_i, as we have seen in the numerical time-evolution calculations. For this reason, in Fig. 5.4 we have compared the results obtained with the analytical model with the results obtained with the numerical time evolution. We compared the results obtained with a fixed value of the coupling and varying the interaction strength. Here, we show the behavior of the charge for different values of the coupling. The regime of validity of our approximation, $\Omega/|U| \gg 1$ belongs to a different region for each line plotted. The weak coupling $\tau\Omega = 100\hbar$ fulfills the condition of small interaction up to $\tau|U| \sim 10\hbar$, and so, the first part of the plot. We can observe that when

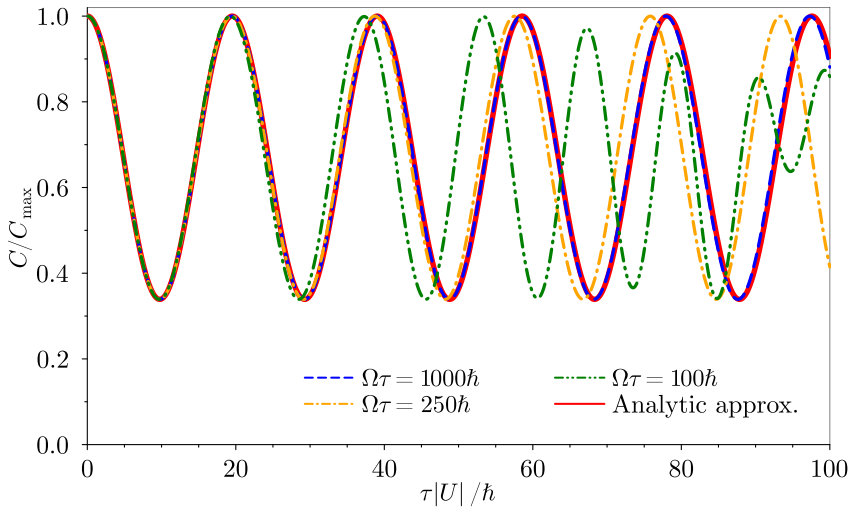

Figure 5.4: Charge as a function of the interaction at the end of the protocol for the two-particle case. We compare the results obtained with the analytical calculations in the limit of $|U|/\Omega \ll 1$ with the numerical time evolutions for different coupling values.

the condition is fulfilled, the approximation reproduces the numerical simulation with high accuracy. Of course, out of the regime, the behavior of the charge as a function of the interaction is not still a constant oscillation and does not reach the maximum charge.

So, we can conclude that our analytical model works perfectly when the coupling is much larger than the interaction strength. This is because the system is isolated into a two-level manifold and each level evolves adiabatically.

5.2.1.2 Site occupations

To gain a deeper understanding of the dynamic effects we deal with, we can examine how the wells are populated as a function of time, and also check if the system is coherent.

We define a coherent system if the wavefunction can be expressed as a single-particle function powered N times, where N is the number of particles. It is trivial to see that a non-interacting system is coherent if the initial state is, as in our case. But when we add interactions, this is no longer necessarily true.

One property of a coherent state is that the one body density matrix (OBDM) has only one non-zero eigenvalue. The eigenvalues of the density matrix are called occupations. The elements of the OBDM (ρ_{ij}) are defined as

$$\rho_{ij} = \langle \Psi | \hat{a}_i^\dagger \hat{a}_j | \Psi \rangle \,, \tag{5.20}$$

where $a_i^\dagger$ (a_i) are the creation (annihilation) operators of the site i and $|\Psi\rangle$ is the state. As we are dealing with a three-site system, the OBDM has three eigenvalues. The

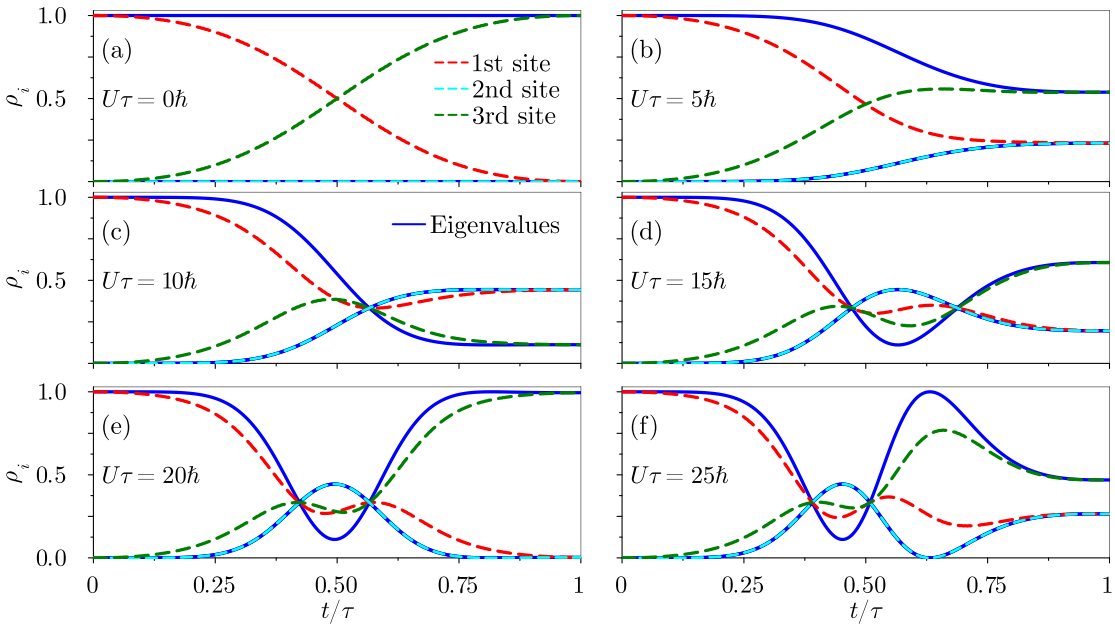

Figure 5.5: Site occupations and OBDM eigenvalues as a function of time for the two-particle case. The occupations of the three sites are represented with dashed lines. The OBDM eigenvalues are represented as solid lines. Note that there are three different eigenvalues, but two of them are degenerate and also have the same value as the occupation in the second site. Each panel corresponds to a different value of the interaction strength. The time-evolution calculations are done using $\Omega\tau/\hbar = 1000$.

diagonal elements of the OBDM give the population of each site. Defined as Eq. (5.20) the OBDM is normalized to the number of particles N. In our case, we use a normalized density matrix, dividing by the number of particles. This is useful when we deal with different numbers of particles to compare one density matrix with the others. In Fig. 5.5 we show the occupations as a function of time for the two-particle case for different interaction values. All the instances correspond to a much larger coupling ensuring to be in the weak interacting regime $U/\Omega \ll 1$. The occupations are plotted as solid blue lines, where for $t = 0$ we obtain one occupation with a value of 1 and the other two at 0, meaning that the initial state is coherent. For the non-interacting case, the coherence is maintained, as we expected. But for an interacting system, the coherence is lost for intermediate times of the protocol. We can recover a coherent state if the system reaches the maximum charge, as in panel (e) for $\tau U/\hbar = 20$, where we are near this situation. The other two occupations are almost degenerated for any interaction and time.

At the same time, we are showing the population of each site with dashed lines. The populations are normalized as the occupations. The non-interacting case, panel (a), has the single-particle effect of not populating the middle site, with a transfer of the particles from the first site to the third one. For finite interactions, the population of the second site starts to populate with almost the same value of the degenerated occupations, for any time and interaction. When the system reaches a maximum charge,

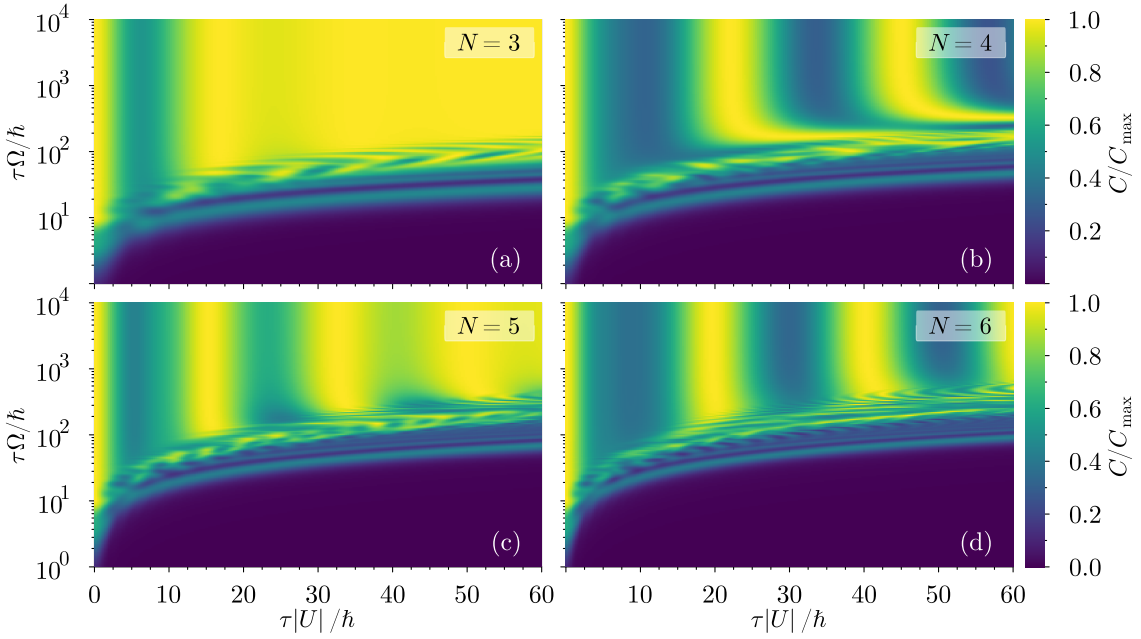

Figure 5.6: Charge as a function of the coupling and the interaction at the end of the protocol for three to six particles. The results are obtained from time-evolution numerical calculations with energy ratios of $\epsilon_1 = 0$ and $\epsilon_3/\epsilon_2 = 1.95$.

the population of the second site vanishes at the end of the protocol.

A common effect that occurs independently of the interaction strength is that the population of the first and the second sites becomes equal at the end of the protocol. This can be understood as these two sites being coupled with enough strength (or time) to transition from one site to another. For that, the average populations in both of them must be equal when the third well is decoupled.

5.2.2 $N > 2$ particles

After understanding the two-particle system, we turn our attention to systems with more particles. First, we examine the $N = 3$, just adding one particle to our previous case. Now, we can compute the charge at the end of the protocol as a function of the interaction and the coupling, as we did before. In Fig. 5.6 we show the numerical calculations and we appreciate some similarities and differences with respect the $N = 2$ case. The first thing we observe is the same regions depending on the ratio between the coupling and the interaction. On the larger interaction region, the system remains discharged for the same reason as $N = 2$. Where both parameters are comparable, we obtain a complicated pattern, and we do not study that situation in detail. Then, with the weak interaction regime, we obtain that the system can reach the maximum charge for several values of the interaction, contrary to the $N = 2$ system, the oscillations saturate to the maximum value. There are still oscillations with a constant frequency (different from the $N = 2$) but with the amplitude modulated.

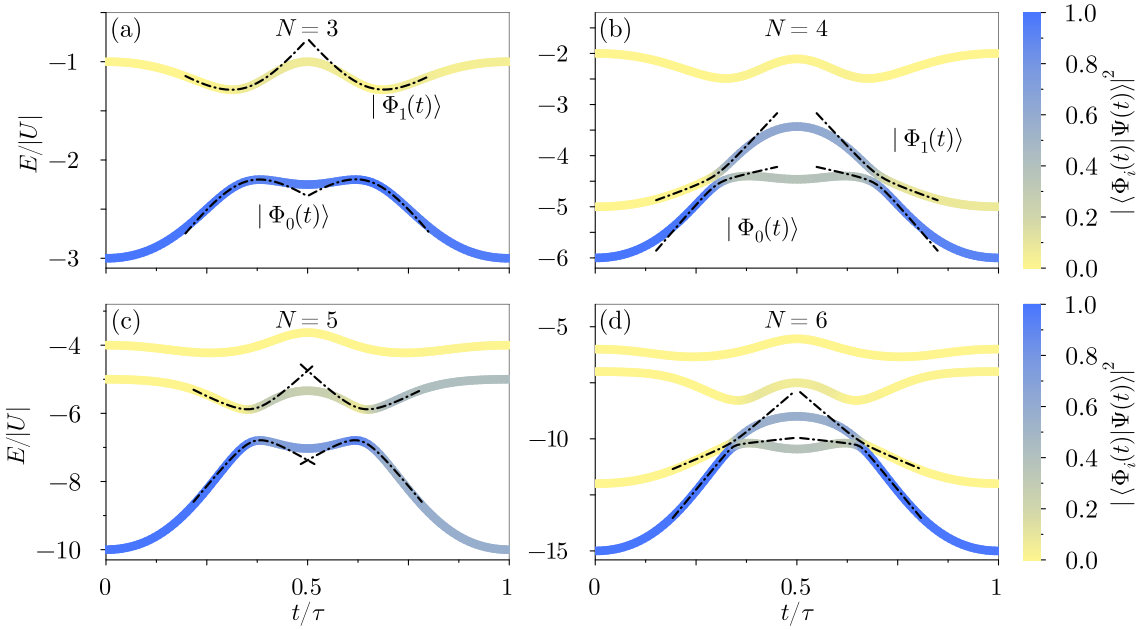

Figure 5.7: Instantaneous energy spectrum of the central manifold and population of the states as a color map, as a function of time for three to six particles. The dash-dotted lines correspond to lines fitted to the Landau-Zener energies. The time-dependent state populations are obtained from a numerical time evolution using $\tau U/\hbar = -20$ and $\tau\Omega/\hbar = 1000$.

When we add another particle to the system, we obtain slightly different results. Of course, the regions remain with the same behavior, but for $N = 4$ in the weak interaction regime we obtain a pattern similar to the $N = 2$. We observe oscillations with constant frequency and amplitude, but these values differ from both numbers of particle systems.

From analyzing the $N = 5$ and $N = 6$ cases, we observe a difference between an odd number of particles and an even one. The systems with an odd N have a damped amplitude. On the other hand, the systems with an even N have a constant amplitude, or else the decrease is very slow.

5.2.2.1 Two level model

Now, we explain the physics in the case of a general number of particles using the information we obtained from the charge diagrams of the $N = 3$ to $N = 6$. Similar to the $N = 2$ we use the information of the energy spectrum to derive the dynamics of the system. In Fig. 5.7 we show the energy spectrum manifold as a function of time corresponding to $N = 3$ to $N = 6$. This manifold corresponds to the states with $E/\Omega \sim 0$, similar to the analysis of the two-particle case.

The number of states in this manifold depends on the number of particles as $\lfloor N/2+1 \rfloor$, where the floor function is defined as $\lfloor x \rfloor = \max\{m \in \mathbb{Z} \,|\, m \leq x\}$. The number of states in this manifold can be obtained as follows. For simplicity, we use the non-interacting case, but the states when it is considered are different, but they are just a superposition of the states we obtain now. In the non-interacting regime, the system is coherent, and so, its wavefunction can be expressed as a product of a single-particle wavefunctions. As we described in Eq. (5.4) and Eq. (5.1), the single-particle energies can be 0 and $\pm\Omega$. So, the states with energy $E = 0$ can be created with pairs of particles on the $|\Psi_\pm\rangle$ states and the rest on the $|\Psi_0\rangle$. So, the number of pairs you can create is $\lfloor N/2 \rfloor$ and we need to add the case with all the particles on the zero-energy state, in total $\lfloor N/2+1 \rfloor$, as we observed. When we include the interaction, if it is small, we can treat it as a perturbation, that breaks the degeneracy, but only mixes these states without including any of the others with energy $|E/\Omega| > 0$.

These energy spectra present some differences with respect to the $N = 2$ case. First of all, there is no degeneracy at the beginning and at the final of the protocol. Moreover, the states do not have any direct crossing anywhere. It is important to remark that our initial state, all the particles in the first site, corresponds to the ground state of this manifold at $t = 0$. Also, the target state, all the particles in the third site, is again the ground state at the end of the protocol time, $t = \tau$. But we can identify avoided crossings, where the most remarkable are between the ground state $|\Phi_0(t)\rangle$ and the first excited $|\Phi_1(t)\rangle$. Here we identify a difference if the number of particles is even or odd. For an even N, the minimum gap is of the order of $\sim 0.2U$, whereas for an odd N, the minimum gap is of the order of $\sim U$.

In addition, in Fig. 5.7 we plot using color the population of each instantaneous eigenstate as a function of time, for a numerical simulation using $\Omega\tau = 1000\hbar$ and $U\tau = -20\hbar$. With this time evolution, we can extract some conclusions. For example, for $N = 3$ the system evolves almost adiabatically through the ground state, obtaining almost the maximum charge. The first excited state is populated with a small probability. The $N = 4$ case is quite different. We find that the first excited state is largely populated in the intermediate times, but then it recombines and most of the population ends in the ground state. However, the system does not reach the maximum charge in that case, as the first excitation remains with a non-zero population. be close anyway. The system with $N = 5$ also populates the first excited, but in that case, the final state does not reach a state close to the maximum charge because the first excited at the end has almost the same population as the ground state, the one with the maximum charge. Finally, for $N = 6$, in the intermediate times, the first excited state becomes more populated than the ground state, but then it recombines and in the end, the system is in the ground state, so, it is charged completely. As a difference from the other cases, here the second excited state becomes slightly populated.

These findings encourage us to develop a simple model, where we consider that the physics of the system occurs only between the ground state and the first excitation.

As we described it is accurate for $N < 6$, and the case $N = 6$ is also pretty accurate for this assumption. In addition, note that the population remains more or less constant away from the minimum gaps. With that, we propose in our model that the evolution through each state is adiabatic and there are transitions only in the minimum gap times. We modeled these transitions as instantaneous in the corresponding time with probability given by the transition probability P.

Summarizing, we start at the ground state of the manifold,

$$|\Psi(t=0)\rangle = |\Phi_0(t=0)\rangle\,, \tag{5.21}$$

it evolves adiabatically until the first avoided crossing, ideally until it reaches the minimum gap time, being $t = \tau_0$, approximately at $t = 0.3\tau$. The state acquires a global phase and we can neglect it,

$$|\Psi(t=\tau_0)\rangle = |\Phi_0(t=\tau_0)\rangle\,. \tag{5.22}$$

Now, with a probability P the state transitions to $|\Phi_1\rangle$, and with $1-P$ it remains in the same state. The state just after the transition is

$$|\Psi(t=\tau_0)\rangle = \sqrt{1-P}|\Phi_0(t=\tau_0)\rangle + i\sqrt{P}|\Phi_1(t=\tau_0)\rangle\,, \tag{5.23}$$

where the relative phase i in principle could be an arbitrary phase, but we need to have it at the end to ensure the normalization of the state. Now, we assume that each state evolves adiabatically with its own phase, and so, the state can be expressed as

$$|\Psi(t)\rangle = \sqrt{1-P}\mathrm{e}^{-i\int_{\tau_0}^{t}E_0 dt/\hbar}|\Phi_0(t)\rangle + i\sqrt{P}\mathrm{e}^{-i\int_{\tau_0}^{t}E_1 dt/\hbar}|\Phi_1(t)\rangle\,. \tag{5.24}$$

It evolves until the second gap minimum at time $t = \tau_1$, approximately at $t = 0.7\tau$. Then, there is another transition, where each state has exactly the same probability P to transition to the other. At that step, we multiplied the wavefunction by a global phase in order to simplify the relative phase,

$$|\Psi(t=\tau_1^-)\rangle = \sqrt{1-P}|\Phi_0(\tau_1)\rangle + i\sqrt{P}\mathrm{e}^{-i\int_{\tau_0}^{\tau_1}(E_1-E_0)dt/\hbar}|\Phi_1(\tau_1\rangle \tag{5.25}$$

$$\begin{aligned}|\Psi(t=\tau_1^+\rangle =&\sqrt{1-P}\left(\sqrt{1-P}|\Phi_0(\tau_1)\rangle + i\sqrt{P}|\Phi_1(\tau_1)\rangle\right)\\ &+ i\sqrt{P}\mathrm{e}^{-i\int_{\tau_0}^{\tau_1}(E_1-E_0)dt/\hbar}\left(i\sqrt{P}|\Phi_0(\tau_1)\rangle + \sqrt{1-P}|\Phi_1(\tau_1)\rangle\right)\,,\end{aligned} \tag{5.26}$$

where $|\Psi(t=\tau_1^-)\rangle$ is the wavefunction just before the transition occurs and $|\Psi(t=\tau_1^+\rangle$ is the wavefunction just after the transition. We can rearrange the equation

$$\begin{aligned}|\Psi(t=\tau_1^+)\rangle = &\left[(1-P) - P\mathrm{e}^{-i\int_{\tau_0}^{\tau_1}(E_1-E_0)dt/\hbar}\right]|\Phi_0(\tau_1)\rangle\\ &+ i\sqrt{P(1-P)}\left[1+\mathrm{e}^{-i\int_{\tau_0}^{\tau_1}(E_1-E_0)dt/\hbar}\right]|\Phi_1(\tau_1)\rangle\,,\end{aligned} \tag{5.27}$$

where we show explicitly the population of the ground state and the first excitation. Note that the relative phase acquired from the other transition up to here caused an

interference affecting the populations of each state. At this point, we suppose that the system evolves adiabatically until the end of the protocol. Each term evolve with its phase, but it does not change the population, reaching at the end of the protocol

$$|\Psi(t=\tau)\rangle = \left[(1-P) - P\mathrm{e}^{-i\int_{\tau_0}^{\tau_1}(E_1-E_0)dt/\hbar}\right]\mathrm{e}^{-i\int_{\tau_1}^{\tau}E_0dt/\hbar}|\Phi_0(\tau)\rangle + i\sqrt{P(1-P)}\left[1+\mathrm{e}^{-i\int_{\tau_0}^{\tau_1}(E_1-E_0)dt/\hbar}\right]\mathrm{e}^{-i\int_{\tau_1}^{\tau}E_1dt/\hbar}|\Phi_1(\tau)\rangle\,. \tag{5.28}$$

At this point, we want to compute the charge of the system, that corresponds to an operator that only takes into account the population of each component, so, the relative phase created in the latter evolution does not play any role. We can define the relative phase as $\phi = \int_{\tau_0}^{\tau_1}(E_0 - E_1)dt/\hbar$, and so, the charge is

$$\frac{C}{C_{\max}} = \frac{\langle\Psi(\tau)|H_0|\Psi(\tau)\rangle}{\langle\Phi_0(\tau)|H_0|\Phi_0(\tau)\rangle}\,, \tag{5.29}$$

writing explicitly the wavefunction at the end of the protocol corresponding to Eq. (5.28),

$$\frac{C}{C_{\max}} = \frac{\left[(1-P) - P\mathrm{e}^{-i\phi}\right]\left[(1-P) - P\mathrm{e}^{i\phi}\right]\langle\Phi_0(\tau)|H_0|\Phi_0(\tau)\rangle}{\langle\Phi_0(\tau)|H_0|\Phi_0(\tau)\rangle} + \frac{(P(1-P))\left[1+\mathrm{e}^{-i\phi}\right]\left[1+\mathrm{e}^{i\phi}\right]\langle\Phi_1(\tau)|H_0|\Phi_1(\tau)\rangle}{\langle\Phi_0(\tau)|H_0|\Phi_0(\tau)\rangle}\,. \tag{5.30}$$

Now simplifying the bra-kets, we obtain

$$\frac{C}{C_{\max}} = (1-P)^2 + P^2 - (P(1-P))\left(\mathrm{e}^{i\phi} + \mathrm{e}^{-i\phi}\right) + (P(1-P))\left(2 + \mathrm{e}^{i\phi} + \mathrm{e}^{-i\phi}\right)(1-c)\,, \tag{5.31}$$

where we apply some basic algebra,

$$\frac{C}{C_{\max}} = (1-P)^2 + P^2 - 2P(1-P)\cos(\phi) + 2(1-c)P(1-P)(1+\cos(\phi)) \tag{5.32}$$

$$= 1 - 2P(1-P) - 2P(1-P)\cos(\phi) + 2P(1-P) + 2P(1-P)\cos(\phi) - 2cP(1-P)(1+\cos(\phi))\,, \tag{5.33}$$

and finally, we simplify the equation to

$$\frac{C}{C_{\max}} = 1 - 4cP(1-P)\sin^2(\phi/2)\,, \tag{5.34}$$

where we defined

$$c = 1 - \frac{\langle\Phi_1(\tau)|H_0|\Phi_1(\tau)\rangle}{\langle\Phi_0(\tau)|H_0|\Phi_0(\tau)\rangle} \tag{5.35}$$

for convenience. With that result, we obtained periodic oscillations governed by the integrated energy separation between the ground state and the first exited between the

minimum gaps. Also, the amplitude of these oscillations is given by the transition probability P. In order to model these probabilities, we used the Landau-Zener transition probability, by fitting the energy spectrum to obtain the parameters.

The Landau-Zener transition describes a two-level system, where both states have a lineal time-dependent energy and an off-diagonal Hamiltonian term that induces an avoided crossing in the system. The Hamiltonian of that system reads

$$\hat{H} = \begin{pmatrix} \alpha_1 t & a \\ a & \alpha_2 t \end{pmatrix} , \tag{5.36}$$

where α_i are the slopes of each state away from the crossing and the off-diagonal element a induces the avoided crossing creating a minimum gap of $2a$ between both states. The Landau-Zener formula says that the probability of having a transition between the states is given by

$$P = \mathrm{e}^{-2\pi \frac{a^2}{\hbar|\alpha|}} , \tag{5.37}$$

where $\alpha = \alpha_1 - \alpha_2$. In our case, we want to obtain the parameters a and α_i for each system we deal with. Even though the value of a can be directly extracted from the energy spectrum by taking half of the minimum gap, we use a fit function to determine it, and the half-gap minimum is a crosscheck.

As the energies in our energy spectrum of Fig. 5.7 are not like the ideal case of a Landau-Zener approximation and does not have a lineal slope away from the crossing, we cannot take the slopes α_i with a linear fit. Instead of that, we fitted the energies around the minima with the energies of the eigenstates of Eq. (5.36), being

$$E_\pm = \frac{1}{2}\left((\alpha_1 + \alpha_2)t \pm \sqrt{4a^2 + (\alpha_1 - \alpha_2)^2 t^2}\right) . \tag{5.38}$$

We use these energies to fit the three parameters, a, α_1, and α_2 for both energies in each crossing. We plotted with dash-dotted lines in Fig. 5.7 the fitted function. We observe that in general, these fits follow the energies, and so, it aims us to use the parameters of the fit to compute the transition probability P.

In Fig. 5.8 we plot the charge as a function of the interaction obtained in the regime of weak interactions ($|U|/\Omega \ll 1$), comparing the results obtained with the numerical time evolution and the results predicted by the two-level model developed. Note the different interaction regimes used in the odd N and for even N. Both results are in qualitative agreement, obtaining almost the same frequency, and also a similar modulation on the amplitude of the oscillations, with better results on the four-particle system.

To obtain the dependence of the model with the interaction it is worth developing a bit the dependence of the phase and the parameters of the Landau-Zener approximation and its dependence on U. First, the phase ϕ is an integral between two states, whose spectrum is invariant when it is represented as in Fig. 5.7, so, the energy scales as E/U

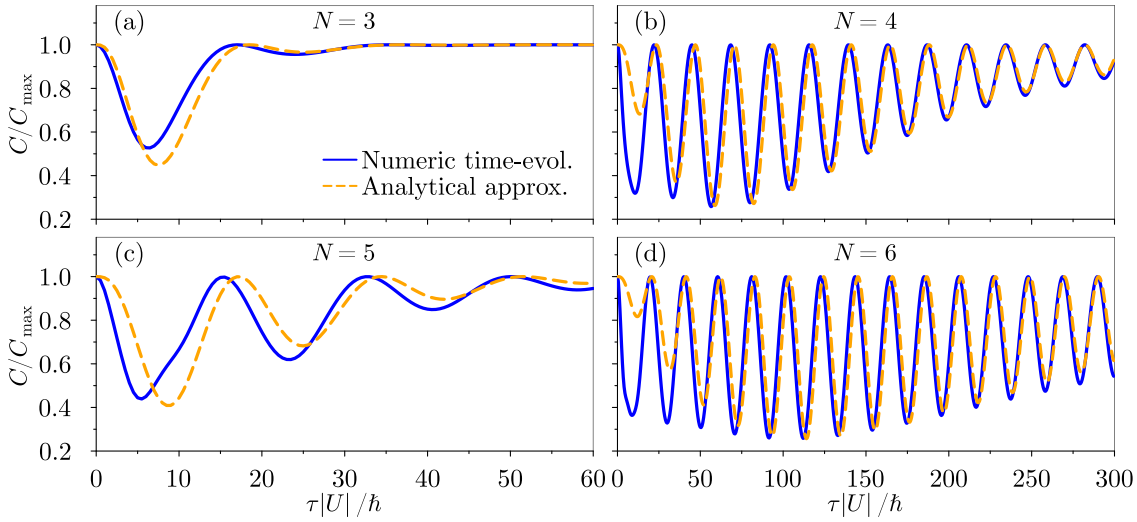

Figure 5.8: Charge as a function of the interaction at the end of the protocol for three to six particles. The numeric values are obtained in the limit of $|U|/\Omega \ll 1$.

and the time as t/τ. Immediately, we can compute the dimensionless phase ϕ' on these units, and so, the phase of the system is $\phi = \phi' U\tau/\hbar$.

The second part corresponds to the transition probability, where we have the parameters a and $|\alpha|$. The first parameter, a, scales with the interaction U, and the slopes α_i, and so, $|\alpha|$ scales as U/τ. With that, we can write the probability as

$$\begin{aligned} P &= \exp\left(-2\pi \frac{(a')^2 U^2}{\hbar |\alpha'| U/\tau}\right) \\ &= \exp\left(-2\pi \frac{(a')^2}{|\alpha'|}\frac{U\tau}{\hbar}\right), \end{aligned} \tag{5.39}$$

where a' and α' are the dimensionless parameters.

One possibility of the discrepancy could be that the Landau-Zener approximation is not exact in our system, as it does not fulfill all the conditions. Also, the assumption that the transition is instantaneous can be a source of the error. Of course, assuming that physics takes place only on these two states is also an approximation, and for more precise details could be necessary to include the second (and the rest) excitation of these manifolds.

5.2.2.2 Occupations

Here we show a similar study of the occupations and populations as in Section 5.2.1.2 but for the systems with more than two particles. In Fig. 5.9 we show the occupations and the populations of each site for $N = 3$ to $N = 6$. We obtain similar effects as in the two-particle case, where the coherence is lost for a finite interaction, and recovering

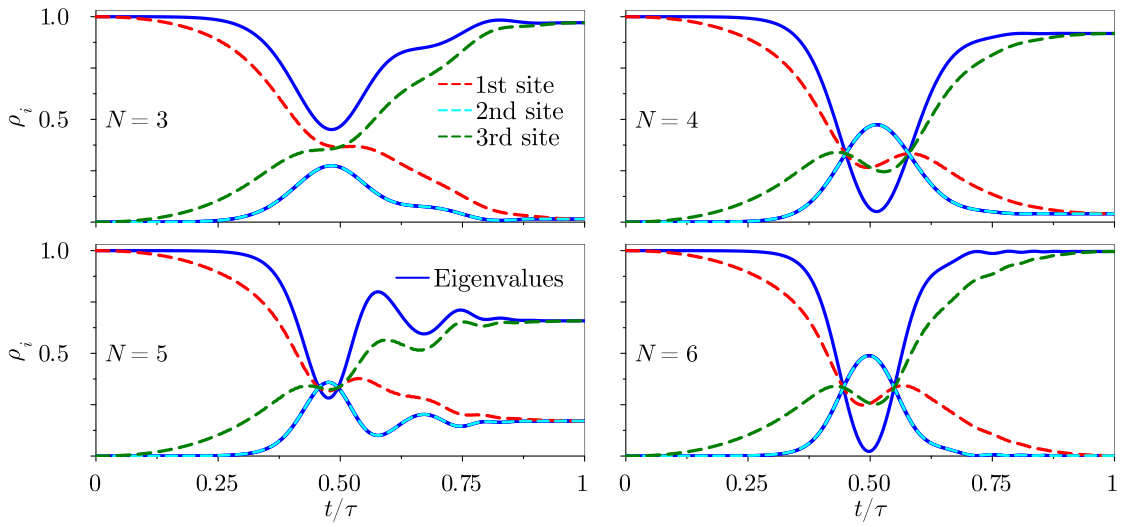

Figure 5.9: Site occupations and the OBDM eigenvalues as a function of time for three to six particles. The occupations of the three sites are represented with dashed lines. The OBDM eigenvalues are represented as solid lines. Note that there are three different eigenvalues, but two of them are degenerate and also have the same value as the occupation in the second site. The time evolution is computed using $\Omega\tau/\hbar = 1000$ and $U\tau/\hbar = 20$, for any number of particles.

it if the system becomes maximum charged. Also, the other two occupations are still quasi-degenerated and with almost the same value as the population of the second site.

We can appreciate that for systems that reach the maximum charge, the occupations and populations are almost symmetrical with respect to the time $t = \tau/2$, not being the case for non-full charged systems.

5.3 Conclusions

In this Chapter, we have presented a proposal for a quantum battery device. It is based on the Spatial Adiabatic Passage (SAP) protocol, where we have included interaction between the particles. We have explored and explained the charge as a function of the interaction strength, showing that it is possible to charge the system even with the presence of the interaction. We also demonstrate that the charging with interaction is no longer adiabatic, where we have excitations on the system. We have used a simple model, assuming that all the dynamics takes place on a two-level system, where we obtained analytical results for two particles, or we have used information from the energy spectrum for larger systems. These models are useful to understand what happens in the time evolution of the state. In addition, comparing the results predicted with those computed numerically agree indicates that our model is accurate even with the approximations we did.

6

SUMMARY AND CONCLUSIONS

In this Thesis, we explored several few-particle systems in which interaction plays a significant role. We examined setups ranging from the continuous harmonic oscillator potential to finite-sized lattice structures. For the systems we examined, no analytical solution exists; therefore, we employed numerical calculations. We specifically chose the exact diagonalization method, enabling us to compute both the low-energy spectrum and the quantum states. We computed other quantities using these states, such as densities or correlations.

Our main goal was to study how interactions affect quantum systems, examining setups ranging from an impurity system to a quantum battery model. In these cases, interaction plays a key role in modifying the ground-state structure and influencing time evolution. Additionally, we examined the effects of system geometry by comparing the physics of regular two-dimensional lattices with those of fractal lattice structures.

We focused on analyzing the ground-state energy as a function of interaction strength and examining also the ground state density. We also used the low-energy spectrum to enhance our understanding of the system where necessary. In addition, we employed other observables to gain insight into the systems, for example by computing pair correlations, one body density matrix, and mean square displacement.

In Chapter 2, we began by explaining the basic quantum mechanics concepts used throughout this Thesis, such as the second quantization formalism. We also presented the Hamiltonians applied in subsequent Chapters: the harmonic oscillator potential with contact interaction and the Bose-Hubbard model. In addition, we addressed a limitation of the exact diagonalization technique when applied to an infinite single-particle basis system, such as the harmonic oscillator.

We explained that for these systems, one must to truncate the basis, resulting in calculation errors. We introduced a method to correct the calculation of the harmonic oscillator potential, leveraging the analytical solution of the two-particle system. This method offers high accuracy for systems with more than two particles, as demonstrated, and requires only information from the known two-particle solution. Thus, there is no

need for information about the specific system under analysis, such as the energy in the infinite interacting limit, to apply this correction.

Even though we presented only a solution for the harmonic trap, we believe it is possible to extrapolate to different potentials following the same described procedure. In such cases, the correction term would depend on the specific system being studied. Certainly, the process could become more complex if the potential does not allow separation of the center-of-mass and relative coordinates. However, we believe it remains feasible to obtain, at least, a numerical value for the correction term.

In Chapter 3, we focused on the study of few-particle systems in a harmonic oscillator potential. As in ultracold atom experiments, we used contact interaction, modeled by a delta function. This interaction was chosen because it is experimentally feasible to reproduce, as is the trap potential. In this Chapter, we explored the effect of the interaction on the systems of distinguishable particles, which can be created by having a set of particles with high spin, each occupying a different spin projection.

Under these conditions, we began by presenting the $SU(N)$ case, where all the particles interact with each other with the same strength. Although this case has been extensively studied previously, we present it as an introduction, and to benchmark the correction procedure introduced in the previous Chapter. In particular, a possible extension of the $SU(N)$ system is to break the symmetry, allowing for different interactions between each particle in the system, beginning with the studies of the rest of this Chapter.

The first step in breaking the symmetry was to study specific scenarios where we turned off some of the interactions between certain pairs of particles. In this situation, we obtained one non-trivial configuration with three particles and five non-trivial configurations with four particles. Then, we explored the ground state in the infinite interacting limit of four non-trivial configurations of the four-particle system, obtaining the density and pair correlations. We described the structure of the systems, as well as the correlations induced by the interactions, showing that it is possible to correlate a pair of particles even though they do not interact with each other. We also obtained a relation of the ground state energies when transitioning from one configuration to another, establishing a connection between the correlation and the energy gap.

These studies could be extrapolated to more particles, where we expect more configurations, as well as some configurations that could be interpreted as generalizations of those studied here. With more particles, it is possible to observe richer physics and increased correlations in the system.

Then, we explored the other non-trivial cases, which correspond to an impurity in a non-interacting bath. With the identification of the system, we can generalize and generate this configuration for a larger number of particles. To study the impurity problem, we have computed the ground state energy of systems with up to eight particles, as

well as the ground state density and low-energy spectrum. Through this analysis, we approximated the system as a double-well potential, where the bath particles create an effective barrier in the center of the trap. We cross-checked our findings using a mean-field approach, which agrees with the double-well interpretation. We also found two different phases in the system: a miscible phase when the impurity remains in the center of the trap, and an immiscible phase that occurs when the interaction increases, causing the impurity to move to the edges of the trap. However, the immiscible phase cannot be described by a mean-field wavefunction because it exhibits large correlations. In this limit, we proposed a new ansatz, with whom we obtained better results than the previous proposals.

Our study of the impurity can be extended in several directions. For example, by including interactions between the bath particles or by adding a second impurity to the system. We described the system with two non-interacting bath particles and two impurities when we examined the non-trivial configurations for four particles, but this can be generalized to study the system in the intermediate interaction regime.

In Chapter 4, we studied the effects of geometry on the time-evolution observables, in particular, the effects of a fractal lattice. We focused on the study of the Sierpiński gasket, but we also compared some results with the Sierpiński carpet. We compared the effects on the gasket with the effects on a regular triangular lattice, maintaining the same length. As it is not possible to simulate an infinite system, we used finite fractal generations.

We started by analyzing the diffusion of a single particle in the fractal, where we obtained a sub-diffusive behavior, compared with the ballistic behavior on the regular lattice. This is not the case for the carpet fractal, where the movement is super-diffusive, also known as sub-ballistic. We found that the movement of a particle on the fractal is largely determined by the connectivity of the lattice. However, using our definition of the Sierpiński gasket lattice, we obtained that the particle does not thermalize for extremely long times.

More interestingly, we obtained a relation between the time evolution and the energy spectrum. Specifically, we relate the exponent of the diffusion to the exponent we obtained from the integrated level spacing. This relation was obtained using scaling arguments and also includes the fractal dimension. Unfortunately, this relation is not universal because a general expression of the exponent of the integrated level spacing cannot usually be found, as in the Sierpiński carpet.

Once the sub-diffusive behavior of a particle in the Sierpiński gasket was determined, we studied in more detail other properties that can be related to the transport. In particular, we have explored the effect of having an interpolated lattice between the fractal and the regular geometry, obtaining a gradual transition in the transport behavior. We also analyzed the effect of a random potential in the lattice sites, where we observed that the

localization associated with the random potential plays a role only for strong random potentials. This is because the localization induced by the fractal dominates over the random one when the random potential strength is weak. We also observed that the particle has a large probability of being found near the initial position, even for a long time. Moreover, we found that for an initial system in a quantum superposition, the fractal can retain information about the relative phase for a long time compared with the regular lattice, where the information is lost when the system thermalizes.

A possibility to expand this study is by considering other fractal structures and checking if the properties obtained here are universal or if they depend largely on the lattice structure. Of course, the diffusion exponents could be different, but the relation between the spatial distribution as a function of time and the energy spectrum could be universal for these fractal systems.

We also expanded the study by adding a second particle and allowing interaction between them. We considered contact interactions, as in a Bose-Hubbard model, and also long-range interactions. We studied the effects of the interaction employing the entanglement of the system, computing two different entropies: a bipartite, where we measure the entanglement between two regions of space, and the entropy between the particles. We found that the entanglement generated depends on the initial state. In particular, if both particles start on the same site then a large contact interaction creates an effective binding, avoiding the separation of the particles.

Moreover, systems with two or more particles can be extremely useful to examine, for example, by studying how the entanglement is affected by the initial conditions. Also, the effect of measurements on the destruction of entanglement can be studied, and whether fractal systems are more robust against entanglement destruction than regular systems.

In Chapter 5, we proposed a three-tilted-site system as a quantum battery by using the SAP protocol. In that protocol, we apply time-dependent coupling between the sites, and with the appropriate functions and parameters, it transfers a single particle from the first site to the third, maintaining the system stable. Our goal was to produce the same protocol but with several interacting particles. This is the reason why we explored the charge as a function of the parameters of the system, including the coupling strength and the interaction strength.

For the two-particle case, we found that weak interactions prevent reaching the maximum charge. However, we observed that for large coupling compared with the interaction, the charge acquires an oscillatory behavior with the interaction strength. Thus, it is possible to reach the maximum charge for some interaction values. We solved analytically the system on the limit of strong coupling, obtaining this oscillatory behavior, with perfect agreement with our numerical simulations. We found that the cause of the oscillation is an interference of the wavefunction.

For more particles, we observed similar behaviors, also with oscillations. For these systems, it was not possible to obtain an analytical derivation. However, we proposed a two-level model to explain the time evolution of the system. In this case, our model includes two transitions modulated by Landau-Zener probabilities and also an interference of the relative phase of the wavefunction. This model is qualitatively useful because it captures most of the physics that occurs in the system.

In contrast to the single-particle case, where the intermediate site is not populated at any time, when we include interactions this intermediate site acquires some population in intermediate times. We also realized that the protocol becomes diabatic since there are transitions during the time evolution. The key thing is that we can obtain the maximum charge by using the appropriate interaction strength.

A natural continuation of this project is to consider a longer array of sites with the appropriate protocol. Furthermore, it could be feasible to study fermionic systems by examining the non-interacting case and introducing an appropriate interaction.

In conclusion, we have studied several quantum systems with different geometries where the interactions played an important role. We have considered two-body interactions, obtaining a precise description of the systems under the effect of the interactions. We derived a method to correct the effect of the truncation when working with the exact diagonalization for the harmonic oscillator confinement. We have explored $SU(N)$ broken symmetry configurations, being novel systems, by analyzing some configurations and how the ground state is configured. In addition, we explored a fractal system encoded in a lattice, by describing a single-particle and two-particle effects. Finally, we have proposed a system in the field of a quantum battery created with a three-well system using the SAP protocol, where we studied the effect of the interaction. In all the research done, we have obtained novel results that could be obtained experimentally in the future.

A

ANALYTICAL ANSATZ CALCULATIONS

In the following, we examine ansatz Eq. (3.10) in more detail. First, we write explicitly about how we determine the weight of each contribution. Then, we show the ansatz for four and five particles, and finally, we present a table with the values of σ_I and σ_b obtained up to $N = 8$.

In order to obtain the weights of each component of the ansatz, we start from the simplest version, i.e., the superposition of Eq. (3.11) and Eq. (3.12). This reads

$$\Psi(x_I, x_i) = \alpha \left[(x_I - x_A)(x_I - x_A) - c|x_I - x_A||x_I - x_A|\right] \mathrm{e}^{-(x_I^2+x_A^2+x_B^2)/2} , \tag{A.1}$$

where we use c as a relative weight between each two components. The energy is obtained by integrating $\Psi(x_I, x_i)\hat{H}\Psi(x_I, x_i)$ and normalizing the constant α. Therefore, for Eq. (A.1) we obtain

$$E = \frac{57\pi c^2 + 102\sqrt{3}c + 38\pi c + 57\pi}{6\left(\pi(c(3c+2)+3) + 6\sqrt{3}c\right)} . \tag{A.2}$$

By minimizing for c, we obtain $E \simeq 3.06916$ with $c = 1$. The solution with $c = 1$ is also obtained numerically when we introduce the σ parameters.

For a larger number of particles we also obtain that all the wavefunction components have the same weight. In Tab. A.1 we show the variational constants σ for values of $N = 3$ to 8 that minimize the total energy corresponding to ansatz Eq. (3.10). We find that σ_b is roughly independent of N, whereas σ_I shows a stronger dependence on N.

To further illustrate the ansatz, we present the explicit expression for four and five particles. The expression for three particles is in the main text in Eq. (3.13). For four particles the ansatz reads

$$\begin{aligned} |\Psi_4, \sigma\rangle = \exp\left[-x_I^2/2\sigma_I^2 - \left(x_A^2 + x_B^2 + x_C^2\right)/2\sigma_b^2\right] &\left[(x_I - x_A)|x_I - x_B||x_I - x_C|\right. \\ &+(x_I - x_B)|x_I - x_A||x_I - x_C| + (x_I - x_C)|x_I - x_A||x_I - x_B| \\ &\left.+(x_I - x_A)(x_I - x_B)(x_I - x_C)\right] , \end{aligned} \tag{A.3}$$

N	3	4	5	6	7	8
σ_I	0.918427	0.853892	0.805508	0.767799	0.737288	0.711888
σ_b	0.946936	0.932079	0.927925	0.927379	0.928215	0.92959

Table A.1: Values of the parameters σ that minimize the energy of ansatz Eq. (3.10). These values are obtained numerically.

while for five particles it reads

$$
\begin{aligned}
|\Psi_{5,\sigma}\rangle = \exp\left[-x_I^2/2\sigma_I^2 - \left(x_A^2 - x_B^2 - x_C^2 - x_D^2\right)/2\sigma_b^2\right] \\
\cdot \left[|x_I - x_A||x_I - x_B||x_I - x_C||x_I - x_D| + (x_I - x_A)(x_I - x_B)(x_I - x_C)(x_I - x_D)\right. \\
+ (x_I - x_A)(x_I - x_B)|x_I - x_C||x_I - x_D| + (x_I - x_A)(x_I - x_C)|x_I - x_B||x_I - x_D| \\
+ (x_I - x_B)(x_I - x_C)|x_I - x_A||x_I - x_D| + (x_I - x_A)(x_I - x_D)|x_I - x_B||x_I - x_C| \\
\left. + (x_I - x_B)(x_I - x_D)|x_I - x_A||x_I - x_C| + (x_I - x_C)(x_I - x_D)|x_I - x_A||x_I - x_B|\right] .
\end{aligned}
\tag{A.4}
$$

Bibliography

B. Ahmadi, P. Mazurek, P. Horodecki, and S. Barzanjeh. Nonreciprocal Quantum Batteries. *Physical Review Letters*, **132**:210402, 2024. (Cited on page 94.)

S. Alexander and R. Orbach. Density of States on Fractals : « Fractons ». *Journal de Physique Lettres*, **43**:625–631, 1982. (Cited on page 69.)

R. Alicki and M. Fannes. Entanglement Boost for Extractable Work from Ensembles of Quantum Batteries. *Physical Review E*, **87**:042123, 2013. (Cited on page 93.)

A. E. Allahverdyan, R. Balian, and T. M. Nieuwenhuizen. Maximal Work Extraction from Finite Quantum Systems. *Europhysics Letters*, **67**:565, 2004. (Cited on page 93.)

M. H. Anderson, J. R. Ensher, M. R. Matthews, C. E. Wieman, and E. A. Cornell. Observation of Bose-Einstein Condensation in a Dilute Atomic Vapor. *Science*, **269**: 198–201, 1995. (Cited on pages 1 and 2.)

P. W. Anderson. Absence of Diffusion in Certain Random Lattices. *Physical Review*, **109**: 1492–1505, 1958. (Cited on page 72.)

G. M. Andolina, M. Keck, A. Mari, M. Campisi, V. Giovannetti, and M. Polini. Extractable Work, the Role of Correlations, and Asymptotic Freedom in Quantum Batteries. *Physical Review Letters*, **122**:047702, 2019. (Cited on page 93.)

L. A. P. Ardila, G. E. Astrakharchik, and S. Giorgini. Strong Coupling Bose Polarons in a Two-Dimensional Gas. *Physical Review Research*, **2**:023405, 2020. (Cited on page 34.)

M. B. Arjmandi, H. Mohammadi, A. Saguia, M. S. Sarandy, and A. C. Santos. Localization Effects in Disordered Quantum Batteries. *Physical Review E*, **108**:064106, 2023. (Cited on pages 93 and 94.)

S. Aubry and G. André. Analyticity Breaking and Anderson Localization in Incommensurate Lattices. *Ann. Israel Phys. Soc*, **3**:18, 1980. (Cited on page 72.)

A. Auffèves. Quantum Technologies Need a Quantum Energy Initiative. *PRX Quantum*, **3**:020101, 2022. (Cited on page 93.)

D. Banerjee, M. Bögli, M. Dalmonte, E. Rico, P. Stebler, U.-J. Wiese, and P. Zoller. Atomic Quantum Simulation of $\mathrm{U}(N)$ and $\mathrm{SU}(N)$ Non-Abelian Lattice Gauge Theories. *Physical Review Letters*, **110**:125303, 2013. (Cited on page 1.)

F. Barra. Dissipative Charging of a Quantum Battery. *Physical Review Letters*, **122**:210601, 2019. (Cited on page 93.)

M. Barth and W. Zwerger. Tan Relations in One Dimension. *Annals of Physics*, **326**: 2544–2565, 2011. (Cited on page 57.)

F. F. Bellotti, A. S. Dehkharghani, and N. T. Zinner. Comparing Numerical and Analytical Approaches to Strongly Interacting Two-Component Mixtures in One Dimensional Traps. *The European Physical Journal D*, **71**:37, 2017. (Cited on page 8.)

A. Benseny, J. Gillet, and T. Busch. Spatial Adiabatic Passage via Interaction-Induced Band Separation. *Physical Review A*, **93**:033629, 2016. (Cited on page 98.)

K. Bergmann, H.-C. Nägerl, C. Panda, G. Gabrielse, E. Miloglyadov, M. Quack, G. Seyfang, G. Wichmann, S. Ospelkaus, A. Kuhn, S. Longhi, A. Szameit, P. Pirro, B. Hillebrands, X.-F. Zhu, J. Zhu, M. Drewsen, W. K. Hensinger, S. Weidt, T. Halfmann, H.-L. Wang, G. S. Paraoanu, N. V. Vitanov, J. Mompart, T. Busch, T. J. Barnum, D. D. Grimes, R. W. Field, M. G. Raizen, E. Narevicius, M. Auzinsh, D. Budker, A. Pálffy, and C. H. Keitel. Roadmap on STIRAP Applications. *Journal of Physics B: Atomic, Molecular and Optical Physics*, **52**:202001, 2019. (Cited on page 94.)

H. Bethe. Zur Theorie der Metalle. *Zeitschrift für Physik*, **71**:205–226, 1931. (Cited on page 8.)

T. Biesenthal, L. J. Maczewsky, Z. Yang, M. Kremer, M. Segev, A. Szameit, and M. Heinrich. Fractal Photonic Topological Insulators. *Science*, **376**:1114–1119, 2022. (Cited on pages 69 and 70.)

F. C. Binder, S. Vinjanampathy, K. Modi, and J. Goold. Quantacell: Powerful Charging of Quantum Batteries. *New Journal of Physics*, **17**:075015, 2015. (Cited on page 93.)

I. Bloch, J. Dalibard, and W. Zwerger. Many-body Physics with Ultracold Gases. *Reviews of Modern Physics*, **80**:885–964, 2008. (Cited on pages 1 and 33.)

I. Bloch, J. Dalibard, and S. Nascimbène. Quantum Simulations with Ultracold Quantum Gases. *Nature Physics*, **8**:267–276, 2012. (Cited on page 1.)

D. Blume. Few-body Physics with Ultracold Atomic and Molecular Systems in Traps. *Reports on Progress in Physics*, **75**:046401, 2012. (Cited on page 33.)

P. Bocchieri and A. Loinger. Quantum Recurrence Theorem. *Physical Review*, **107**:337–338, 1957. (Cited on page 93.)

O. Bohigas, A. M. Lane, and J. Martorell. Sum Rules for Nuclear Collective Excitations. *Physics Reports*, **51**:267–316, 1979. (Cited on page 11.)

L. Bonnes, K. R. A. Hazzard, S. R. Manmana, A. M. Rey, and S. Wessel. Adiabatic Loading of One-Dimensional $SU(N)$ Alkaline-Earth-Atom Fermions in Optical Lattices. *Physical Review Letters*, **109**:205305, 2012. (Cited on page 33.)

Bose. Plancks Gesetz und Lichtquantenhypothese. *Zeitschrift für Physik*, **26**:178–181, 1924. (Cited on page 2.)

C. J. Bradly, M. Rab, A. D. Greentree, and A. M. Martin. Coherent Tunneling via Adiabatic Passage in a Three-Well Bose-Hubbard System. *Physical Review A*, **85**:053609, 2012. (Cited on page 94.)

F. Brauneis, A. Ghazaryan, H.-W. Hammer, and A. G. Volosniev. Emergence of a Bose Polaron in a Small Ring Threaded by the Aharonov-Bohm Flux. *Communications Physics*, **6**:1–9, 2023. (Cited on page 33.)

M. Brzezińska, A. M. Cook, and T. Neupert. Topology in the Sierpiński-Hofstadter Problem. *Physical Review B*, **98**:205116, 2018. (Cited on page 69.)

L. Budewig, S. I. Mistakidis, and P. Schmelcher. Quench Dynamics of Two One-Dimensional Harmonically Trapped Bosons Bridging Attraction and Repulsion. *Molecular Physics*, **117**:2043–2057, 2019. (Cited on page 15.)

T. Busch, B.-G. Englert, K. Rzażewski, and M. Wilkens. Two Cold Atoms in a Harmonic Trap. *Foundations of Physics*, **28**:549–559, 1998. (Cited on pages 1, 17, 18, 25, 48, and 59.)

F. Campaioli, F. A. Pollock, F. C. Binder, L. Céleri, J. Goold, S. Vinjanampathy, and K. Modi. Enhancing the Charging Power of Quantum Batteries. *Physical Review Letters*, **118**:150601, 2017. (Cited on page 93.)

S. Capponi, P. Lecheminant, and K. Totsuka. Phases of One-Dimensional SU(N) Cold Atomic Fermi Gases –from Molecular Luttinger Liquids to Topological Phases. *Annals of Physics*, **367**:50–95, 2016. (Cited on page 35.)

G. Carleo and M. Troyer. Solving the Quantum Many-Body Problem with Artificial Neural Networks. *Science*, **355**:602–606, 2017. (Cited on page 8.)

M. Carrega, A. Crescente, D. Ferraro, and M. Sassetti. Dissipative Dynamics of an Open Quantum Battery. *New Journal of Physics*, **22**:083085, 2020. (Cited on page 93.)

M. A. Cazalilla and A. M. Rey. Ultracold Fermi Gases with Emergent SU(N) Symmetry. *Reports on Progress in Physics*, **77**:124401, 2014. (Cited on page 34.)

J. Chen, S. I. Mistakidis, and P. Schmelcher. Intra- and Interband Excitations Induced Residue Decay of the Bose Polaron in a One-Dimensional Double-Well. *New Journal of Physics*, **24**:033004, 2022. (Cited on page 62.)

C. Chin, R. Grimm, P. Julienne, and E. Tiesinga. Feshbach Resonances in Ultracold Gases. *Reviews of Modern Physics*, **82**:1225–1286, 2010. (Cited on pages 2 and 35.)

S. Choudhury, K. R. Islam, Y. Hou, J. A. Aman, T. C. Killian, and K. R. A. Hazzard. Collective Modes of Ultracold Fermionic Alkaline-Earth-Metal Gases with SU(N) Symmetry. *Physical Review A*, **101**:053612, 2020. (Cited on page 34.)

R. S. Christensen, J. Levinsen, and G. M. Bruun. Quasiparticle Properties of a Mobile Impurity in a Bose-Einstein Condensate. *Physical Review Letters*, **115**:160401, 2015. (Cited on page 33.)

A. Chrostowski and T. Sowiński. Efficient Construction of Many-Body Fock States Having the Lowest Energies. *Acta Physica Polonica A*, **136**:566–570, 2019. (Cited on pages 5 and 21.)

A. Crescente, M. Carrega, M. Sassetti, and D. Ferraro. Ultrafast Charging in a Two-Photon Dicke Quantum Battery. *Physical Review B*, **102**:245407, 2020. (Cited on page 93.)

C. Cruz, M. F. Anka, M. S. Reis, R. Bachelard, and A. C. Santos. Quantum Battery Based on Quantum Discord at Room Temperature. *Quantum Science and Technology*, **7**:025020, 2022. (Cited on page 94.)

F. Dalfovo, S. Giorgini, L. P. Pitaevskii, and S. Stringari. Theory of Bose-Einstein Condensation in Trapped Gases. *Reviews of Modern Physics*, **71**:463–512, 1999. (Cited on pages 1, 5, and 8.)

Z. Darázs, A. Anishchenko, T. Kiss, A. Blumen, and O. Mülken. Transport Properties of Continuous-Time Quantum Walks on Sierpinski Fractals. *Physical Review E*, **90**:032113, 2014. (Cited on pages 70 and 71.)

K. B. Davis, M. O. Mewes, M. R. Andrews, N. J. van Druten, D. S. Durfee, D. M. Kurn, and W. Ketterle. Bose-Einstein Condensation in a Gas of Sodium Atoms. *Physical Review Letters*, **75**:3969–3973, 1995. (Cited on page 2.)

J. de Hond, J. Xiang, W. C. Chung, E. Cruz-Colón, W. Chen, W. C. Burton, C. J. Kennedy, and W. Ketterle. Preparation of the Spin-Mott State: A Spinful Mott Insulator of Repulsively Bound Pairs. *Physical Review Letters*, **128**:093401, 2022. (Cited on page 13.)

J. Decamp, P. Armagnat, B. Fang, M. Albert, A. Minguzzi, and P. Vignolo. Exact Density Profiles and Symmetry Classification for Strongly Interacting Multi-Component Fermi Gases in Tight Waveguides. *New Journal of Physics*, **18**:055011, 2016. (Cited on page 37.)

S. Deffner. Energetic Cost of Hamiltonian Quantum Gates. *Europhysics Letters*, **134**:40002, 2021. (Cited on page 93.)

S. Deffner and S. Campbell. *Quantum Thermodynamics: An Introduction to the Thermodynamics of Quantum Information*. Morgan & Claypool Publishers, 2019. (Cited on page 93.)

A. S. Dehkharghani, A. G. Volosniev, and N. T. Zinner. Coalescence of Two Impurities in a Trapped One-dimensional Bose Gas. *Physical Review Letters*, **121**:080405, 2018. (Cited on page 53.)

F. Deuretzbacher, K. Bongs, K. Sengstock, and D. Pfannkuche. Evolution from a Bose-Einstein Condensate to a Tonks-Girardeau Gas: An Exact Diagonalization Study. *Physical Review A*, **75**:013614, 2007. (Cited on pages 8 and 35.)

F. Deuretzbacher, K. Fredenhagen, D. Becker, K. Bongs, K. Sengstock, and D. Pfannkuche. Exact Solution of Strongly Interacting Quasi-One-Dimensional Spinor Bose Gases. *Physical Review Letters*, **100**:160405, 2008. (Cited on page 1.)

F. Deuretzbacher, J. C. Cremon, and S. M. Reimann. Ground-state Properties of Few Dipolar Bosons in a Quasi-One-Dimensional Harmonic Trap. *Physical Review A*, **81**: 063616, 2010. (Cited on page 33.)

J. Dobrzyniecki and T. Sowiński. Simulating Artificial One-Dimensional Physics with Ultra-Cold Fermionic Atoms: Three Exemplary Themes. *Advanced Quantum Technologies*, **3**:2000010, 2020. (Cited on page 1.)

E. Domany, S. Alexander, D. Bensimon, and L. P. Kadanoff. Solutions to the Schrödinger Equation on Some Fractal Lattices. *Physical Review B*, **28**:3110–3123, 1983. (Cited on page 72.)

M. Ebert, A. Volosniev, and H.-W. Hammer. Two Cold Atoms in a Time-Dependent Harmonic Trap in One Dimension. *Annalen der Physik*, **528**:693–704, 2016. (Cited on page 33.)

K. Eckert, M. Lewenstein, R. Corbalán, G. Birkl, W. Ertmer, and J. Mompart. Three-level Atom Optics via the Tunneling Interaction. *Physical Review A*, **70**:023606, 2004. (Cited on pages 4 and 94.)

A. Einstein. Über Einen Die Erzeugung Und Verwandlung Des Lichtes Betreffenden Heuristischen Gesichtspunkt. *Annalen der Physik*, **322**:132–148, 1905. (Cited on page 1.)

A. Einstein. Quantentheorie Des Einatomigen Idealen Gases. *Sitzungsberichte der Königlich Preussischen Akademie der Wissenschaften zu Berlin*, pages 261–267, 1924. (Cited on page 2.)

J. Erdmann, S. I. Mistakidis, and P. Schmelcher. Phase-separation Dynamics Induced by an Interaction Quench of a Correlated Fermi-Fermi Mixture in a Double Well. *Physical Review A*, **99**:013605, 2019. (Cited on page 62.)

T. Ernst, D. W. Hallwood, J. Gulliksen, H.-D. Meyer, and J. Brand. Simulating Strongly Correlated Multiparticle Systems in a Truncated Hilbert Space. *Physical Review A*, **84**: 023623, 2011. (Cited on pages 5, 17, and 24.)

A. Fabrocini and A. Polls. ^{3}He Impurity Excitation Spectrum in Liquid ^{4}He. *Physical Review B*, **58**:5209–5212, 1998. (Cited on page 33.)

M. Ferraretto, A. Richaud, L. Del Re, L. Fallani, and M. Capone. Enhancement of Chiral Edge Currents in (d+1)-Dimensional Atomic Mott-band Hybrid Insulators. *SciPost Physics*, **14**:048, 2023. (Cited on page 37.)

D. Ferraro, M. Campisi, G. M. Andolina, V. Pellegrini, and M. Polini. High-Power Collective Charging of a Solid-State Quantum Battery. *Physical Review Letters*, **120**: 117702, 2018. (Cited on page 93.)

R. P. Feynman. Forces in Molecules. *Physical Review*, **56**:340–343, 1939. (Cited on page 57.)

R. Fleischmann, T. Geisel, R. Ketzmerick, and G. Petschel. Quantum Diffusion, Fractal Spectra, and Chaos in Semiconductor Microstructures. *Physica D: Nonlinear Phenomena*, **86**:171–181, 1995. (Cited on page 72.)

Y. Florshaim, E. Zohar, D. Z. Koplovich, I. Meltzer, R. Weill, J. Nemirovsky, A. Stern, and Y. Sagi. Spatial Adiabatic Passage of Ultracold Atoms in Optical Tweezers. *Science Advances*, **10**:eadl1220, 2024. (Cited on page 94.)

J. K. Freericks and H. Monien. Phase Diagram of the Bose-Hubbard Model. *Europhysics Letters (EPL)*, **26**:545–550, 1994. (Cited on page 85.)

M. Fremling, M. van Hooft, C. M. Smith, and L. Fritz. Existence of Robust Edge Currents in Sierpiński Fractals. *Physical Review Research*, **2**:013044, 2020. (Cited on page 69.)

M. A. García-March, B. Juliá-Díaz, G. E. Astrakharchik, T. Busch, J. Boronat, and A. Polls. Quantum Correlations and Spatial Localization in One-Dimensional Ultracold Bosonic Mixtures. *New Journal of Physics*, **16**:103004, 2014. (Cited on page 43.)

M. A. García-March, A. V. Yuste-Roca, B. Juliá-Díaz, and A. Polls. Mesoscopic Superpositions of Tonks-Girardeau States and the Bose-Fermi Mapping. *Physical Review A*, **92**: 033621, 2015. (Cited on page 36.)

M. A. García-March, A. S. Dehkharghani, and N. T. Zinner. Entanglement of an Impurity in a Few-Body One-Dimensional Ideal Bose System. *Journal of Physics B: Atomic, Molecular and Optical Physics*, **49**:075303, 2016. (Cited on pages 55, 56, and 57.)

Y. Gefen, B. B. Mandelbrot, and A. Aharony. Critical Phenomena on Fractal Lattices. *Physical Review Letters*, **45**:855–858, 1980. (Cited on pages 69 and 70.)

Y. Gefen, A. Aharony, B. B. Mandelbrot, and S. Kirkpatrick. Solvable Fractal Family, and Its Possible Relation to the Backbone at Percolation. *Physical Review Letters*, **47**: 1771–1774, 1981. (Cited on page 69.)

Y. Gefen, A. Aharony, and S. Alexander. Anomalous Diffusion on Percolating Clusters. *Physical Review Letters*, **50**:77–80, 1983. (Cited on page 69.)

Y. Gefen, A. Aharony, and B. B. Mandelbrot. Phase Transitions on Fractals. III. Infinitely Ramified Lattices. *Journal of Physics A: Mathematical and General*, **17**:1277, 1984. (Cited on page 72.)

T. Geisel, R. Ketzmerick, and G. Petschel. New Class of Level Statistics in Quantum Systems with Unbounded Diffusion. *Physical Review Letters*, **66**:1651–1654, 1991. (Cited on page 72.)

G. Gemme, M. Grossi, D. Ferraro, S. Vallecorsa, and M. Sassetti. IBM Quantum Platforms: A Quantum Battery Perspective. *Batteries*, **8**:43, 2022. (Cited on page 93.)

S. E. Gharashi, K. M. Daily, and D. Blume. Three s-Wave-Interacting Fermions under Anisotropic Harmonic Confinement: Dimensional Crossover of Energetics and Virial Coefficients. *Physical Review A*, **86**:042702, 2012. (Cited on page 33.)

S. Gherardini, F. Campaioli, F. Caruso, and F. C. Binder. Stabilizing Open Quantum Batteries by Sequential Measurements. *Physical Review Research*, **2**:013095, 2020. (Cited on page 94.)

S. Ghosh and A. Sen(De). Dimensional Enhancements in a Quantum Battery with Imperfections. *Physical Review A*, **105**:022628, 2022. (Cited on page 94.)

T. Giamarchi. *Quantum Physics in One Dimension*. Clarendon Press, 2003. (Cited on pages 1 and 2.)

S. Giorgini, L. P. Pitaevskii, and S. Stringari. Theory of Ultracold Atomic Fermi Gases. *Reviews of Modern Physics*, **80**:1215–1274, 2008. (Cited on page 1.)

M. Girardeau. Relationship between Systems of Impenetrable Bosons and Fermions in One Dimension. *Journal of Mathematical Physics*, **1**:516–523, 1960. (Cited on page 35.)

M. Girardeau. Motion of an Impurity Particle in a Boson Superfluid. *Physics of Fluids*, **4**: 279, 1961. (Cited on page 33.)

M. D. Girardeau. Tonks-Girardeau and Super-Tonks-Girardeau States of a Trapped One-Dimensional Spinor Bose Gas. *Physical Review A*, **83**:011601, 2011. (Cited on page 35.)

M. C. Gordillo. One-dimensional SU(N) Clusters of Fermions in Optical Lattices. *New Journal of Physics*, **21**:103020, 2019. (Cited on page 34.)

M. C. Gordillo, F. Mazzanti, and J. Boronat. One-dimensional Harmonically Confined SU(N) Fermions. *Physical Review A*, **100**:023603, 2019. (Cited on page 33.)

T. Grining, M. Tomza, M. Lesiuk, M. Przybytek, M. Musiał, P. Massignan, M. Lewenstein, and R. Moszynski. Many Interacting Fermions in a One-Dimensional Harmonic Trap: A Quantum-Chemical Treatment. *New Journal of Physics*, **17**:115001, 2015a. (Cited on page 5.)

T. Grining, M. Tomza, M. Lesiuk, M. Przybytek, M. Musiał, R. Moszynski, M. Lewenstein, and P. Massignan. Crossover between Few and Many Fermions in a Harmonic Trap. *Physical Review A*, **92**:061601, 2015b. (Cited on page 8.)

C. Gross and I. Bloch. Quantum Simulations with Ultracold Atoms in Optical Lattices. *Science*, **357**:995–1001, 2017. (Cited on page 2.)

F. Grusdt, G. E. Astrakharchik, and E. Demler. Bose Polarons in Ultracold Atoms in One Dimension: Beyond the Fröhlich Paradigm. *New Journal of Physics*, **19**:103035, 2017. (Cited on page 53.)

F. Grusdt, N. Mostaan, E. Demler, and L. A. P. Ardila. Impurities and Polarons in Bosonic Quantum Gases: A Review on Recent Progress. arXiv:2410.09413, 2024. (Cited on page 3.)

J.-Y. Gyhm and U. R. Fischer. Beneficial and Detrimental Entanglement for Quantum Battery Charging. *AVS Quantum Science*, **6**:012001, 2024. (Cited on page 93.)

J.-Y. Gyhm, D. Šafránek, and D. Rosa. Quantum Charging Advantage Cannot Be Extensive without Global Operations. *Physical Review Letters*, **128**:140501, 2022. (Cited on page 93.)

F. Haake. *Quantum Signatures of Chaos*. Springer-Verlag, 2006. (Cited on page 72.)

N. L. Harshman. Spectroscopy for a Few Atoms Harmonically Trapped in One Dimension. *Physical Review A*, **89**:033633, 2014. (Cited on page 33.)

S. Havlin and D. Ben-Avraham. Diffusion in Disordered Media. *Advances in Physics*, 1987. (Cited on page 69.)

C. He, Z. Ren, B. Song, E. Zhao, J. Lee, Y.-C. Zhang, S. Zhang, and G.-B. Jo. Collective Excitations in Two-Dimensional SU(N) Fermi Gases with Tunable Spin. *Physical Review Research*, **2**:012028, 2020. (Cited on page 34.)

R. N. Hill. Rates of Convergence and Error Estimation Formulas for the Rayleigh–Ritz Variational Method. *The Journal of Chemical Physics*, **83**:1173–1196, 1985. (Cited on page 16.)

T.-L. Ho and V. B. Shenoy. Binary Mixtures of Bose Condensates of Alkali Atoms. *Physical Review Letters*, **77**:3276–3279, 1996. (Cited on page 66.)

M. J. Holland, B. DeMarco, and D. S. Jin. Evaporative Cooling of a Two-Component Degenerate Fermi Gas. *Physical Review A*, **61**:053610, 2000. (Cited on page 2.)

O. Hryhorchak, G. Panochko, and V. Pastukhov. Mean-field Study of Repulsive 2D and 3D Bose Polarons. *Journal of Physics B: Atomic, Molecular and Optical Physics*, **53**:205302, 2020. (Cited on page 34.)

C.-K. Hu, J. Qiu, P. J. P. Souza, J. Yuan, Y. Zhou, L. Zhang, J. Chu, X. Pan, L. Hu, J. Li, Y. Xu, Y. Zhong, S. Liu, F. Yan, D. Tan, R. Bachelard, C. J. Villas-Boas, A. C. Santos, and D. Yu. Optimal Charging of a Superconducting Quantum Battery. *Quantum Science and Technology*, **7**:045018, 2022. (Cited on page 93.)

M.-G. Hu, M. J. Van de Graaff, D. Kedar, J. P. Corson, E. A. Cornell, and D. S. Jin. Bose Polarons in the Strongly Interacting Regime. *Physical Review Letters*, **117**:055301, 2016. (Cited on page 33.)

J. Hubbard. Electron Correlations in Narrow Energy Bands. *Proceedings of the Royal Society of London. Series A. Mathematical and Physical Sciences*, **276**:238–257, 1963. (Cited on page 13.)

A. A. Iliasov, M. I. Katsnelson, and S. Yuan. Hall Conductivity of a Sierpiński Carpet. *Physical Review B*, **101**:045413, 2020. (Cited on page 69.)

M. N. Ivaki, I. Sahlberg, K. Pöyhönen, and T. Ojanen. Topological Random Fractals. *Communications Physics*, **5**:1–8, 2022. (Cited on page 69.)

R. Jastrow. Many-Body Problem with Strong Forces. *Physical Review*, **98**:1479–1484, 1955. (Cited on page 55.)

P. Jeszenszki, H. Luo, A. Alavi, and J. Brand. Accelerating the Convergence of Exact Diagonalization with the Transcorrelated Method: Quantum Gas in One Dimension with Contact Interactions. *Physical Review A*, **98**:053627, 2018. (Cited on pages 5 and 17.)

N. B. Jørgensen, L. Wacker, K. T. Skalmstang, M. M. Parish, J. Levinsen, R. S. Christensen, G. M. Bruun, and J. J. Arlt. Observation of Attractive and Repulsive Polarons in a Bose-Einstein Condensate. *Physical Review Letters*, **117**:055302, 2016. (Cited on pages 33 and 56.)

J. Joshi and T. S. Mahesh. Experimental Investigation of a Quantum Battery Using Star-Topology NMR Spin Systems. *Physical Review A*, **106**:042601, 2022. (Cited on page 93.)

K. Kanjilal and D. Blume. Nondivergent Pseudopotential Treatment of Spin-Polarized Fermions under One- and Three-Dimensional Harmonic Confinement. *Physical Review A*, **70**:042709, 2004. (Cited on page 1.)

J. W. T. Keeble, M. Drissi, A. Rojo-Francàs, B. Juliá-Díaz, and A. Rios. Machine Learning One-Dimensional Spinless Trapped Fermionic Systems with Neural-Network Quantum States. *Physical Review A*, **108**:063320, 2023. (Cited on page 8.)

S. N. Kempkes, M. R. Slot, S. E. Freeney, S. J. M. Zevenhuizen, D. Vanmaekelbergh, I. Swart, and C. M. Smith. Design and Characterization of Electrons in a Fractal Geometry. *Nature Physics*, **15**:127–131, 2019. (Cited on page 69.)

J. Kim, J. Murugan, J. Olle, and D. Rosa. Operator Delocalization in Quantum Networks. *Physical Review A*, **105**:L010201, 2022. (Cited on page 93.)

T. Kinoshita, T. Wenger, and D. S. Weiss. Observation of a One-Dimensional Tonks-Girardeau Gas. *Science*, **305**:1125–1128, 2004. (Cited on page 1.)

T. Kinoshita, T. Wenger, and D. S. Weiss. Local Pair Correlations in One-Dimensional Bose Gases. *Physical Review Letters*, **95**:190406, 2005. (Cited on page 43.)

D. Kleppner and R. Jackiw. One Hundred Years of Quantum Physics. *Science*, **289**: 893–898, 2000. (Cited on page 1.)

G. Koch and A. Posazhennikova. Loop Current States and Their Stability in Small Fractal Lattices of Bose-Einstein Condensates. *Phys. Rev. A*, **110**:033301, 2024. (Cited on page 69.)

M. Kohmoto, L. P. Kadanoff, and C. Tang. Localization Problem in One Dimension: Mapping and Escape. *Physical Review Letters*, **50**:1870–1872, 1983. (Cited on page 72.)

T. K. Konar, L. G. C. Lakkaraju, S. Ghosh, and A. Sen(De). Quantum Battery with Ultracold Atoms: Bosons versus Fermions. *Physical Review A*, **106**:022618, 2022. (Cited on page 94.)

M. Koschorreck, D. Pertot, E. Vogt, B. Fröhlich, M. Feld, and M. Köhl. Attractive and Repulsive Fermi Polarons in Two Dimensions. *Nature*, **485**:619–622, 2012. (Cited on page 34.)

A. Kosior and K. Sacha. Localization in Random Fractal Lattices. *Physical Review B*, **95**: 104206, 2017. (Cited on page 69.)

R. Krcmar, J. Genzor, Y. Lee, H. Čenčariková, T. Nishino, and A. Gendiar. Tensor-network Study of a Quantum Phase Transition on the Sierpiński Fractal. *Physical Review E*, **98**: 062114, 2018. (Cited on page 8.)

M. Kutschera and W. Wójcik. Proton Impurity in the Neutron Matter: A Nuclear Polaron Problem. *Physical Review C*, **47**:1077–1085, 1993. (Cited on page 33.)

E. K. Laird, Z.-Y. Shi, M. M. Parish, and J. Levinsen. SU(N) Fermions in a One-Dimensional Harmonic Trap. *Physical Review A*, **96**:032701, 2017. (Cited on pages 27, 28, 30, 33, 36, and 37.)

LD. Landau and SI. Pekar. Effective Mass of a Polaron. *Zh. Eksp. Teor. Fiz*, **18**:419–423, 1948. (Cited on page 33.)

T. P. Le, J. Levinsen, K. Modi, M. M. Parish, and F. A. Pollock. Spin-chain Model of a Many-Body Quantum Battery. *Physical Review A*, **97**:022106, 2018. (Cited on page 94.)

R. B. Lehoucq, D. C. Sorensen, and C. Yang. *ARPACK Users' Guide: Solution of Large-scale Eigenvalue Problems with Implicitly Restarted Arnoldi Methods*. SIAM, 1998. (Cited on page 9.)

M. Lewenstein, A. Sanpera, and V. Ahufinger. *Ultracold Atoms in Optical Lattices: Simulating Quantum Many-Body Systems*. OUP Oxford, 2012. (Cited on page 1.)

X. Li, M. C. Jha, and A. E. B. Nielsen. Laughlin Topology on Fractal Lattices without Area Law Entanglement. *Physical Review B*, **105**:085152, 2022. (Cited on page 69.)

S. Liang, D. Zhang, and W. Chen. Momentum Distribution and Tunneling Density of States of One-Dimensional Fermonic SU(N) Hubbard Model. *Journal of Physics: Condensed Matter*, **31**:185601, 2019. (Cited on page 34.)

E. J. Lindgren, J. Rotureau, C. Forssén, A. G. Volosniev, and N. T. Zinner. Fermionization of Two-Component Few-Fermion Systems in a One-Dimensional Harmonic Trap. *New Journal of Physics*, **16**:063003, 2014. (Cited on page 33.)

X.-J. Liu, H. Hu, and P. D. Drummond. Multicomponent Strongly Attractive Fermi Gas: A Color Superconductor in a One-Dimensional Harmonic Trap. *Physical Review A*, **77**: 013622, 2008. (Cited on page 33.)

Y. Loiko, V. Ahufinger, R. Menchon-Enrich, G. Birkl, and J. Mompart. Coherent Injecting, Extracting, and Velocity Filtering of Neutral Atoms in a Ring Trap via Spatial Adiabatic Passage. *The European Physical Journal D*, **68**:147, 2014. (Cited on page 94.)

Yu. Loiko, V. Ahufinger, R. Corbalán, G. Birkl, and J. Mompart. Filtering of Matter-Wave Vibrational States via Spatial Adiabatic Passage. *Physical Review A*, **83**:033629, 2011. (Cited on page 94.)

S. Longhi. Adiabatic Passage of Light in Coupled Optical Waveguides. *Physical Review E*, **73**:026607, 2006. (Cited on page 94.)

S. Longhi, G. Della Valle, M. Ornigotti, and P. Laporta. Coherent Tunneling by Adiabatic Passage in an Optical Waveguide System. *Physical Review B*, **76**:201101, 2007. (Cited on page 94.)

T. Lunghi, F. Doutre, A. P. Rambu, M. Bellec, M. P. D. Micheli, A. M. Apetrei, O. Alibart, N. Belabas, S. Tascu, and S. Tanzilli. Broadband Integrated Beam Splitter Using Spatial Adiabatic Passage. *Optics Express*, **26**:27058–27063, 2018. (Cited on page 94.)

Z. Luo, C. E. Berger, and J. E. Drut. Harmonically Trapped Fermions in Two Dimensions: Ground-state Energy and Contact of SU(2) and SU(4) Systems via a Nonuniform Lattice Monte Carlo Method. *Physical Review A*, **93**:033604, 2016. (Cited on page 5.)

I. Maillette de Buy Wenniger, S. E. Thomas, M. Maffei, S. C. Wein, M. Pont, N. Belabas, S. Prasad, A. Harouri, A. Lemaître, I. Sagnes, N. Somaschi, A. Auffèves, and P. Senellart. Experimental Analysis of Energy Transfers between a Quantum Emitter and Light Fields. *Physical Review Letters*, **131**:260401, 2023. (Cited on page 93.)

B. Mandelbrot. How Long Is the Coast of Britain? Statistical Self-Similarity and Fractional Dimension. *Science*, **156**:636–638, 1967. (Cited on page 69.)

S. Manna, B. Pal, W. Wang, and A. E. B. Nielsen. Anyons and Fractional Quantum Hall Effect in Fractal Dimensions. *Physical Review Research*, **2**:023401, 2020. (Cited on page 69.)

S. Manna, C. W. Duncan, C. A. Weidner, J. F. Sherson, and A. E. B. Nielsen. Anyon Braiding on a Fractal Lattice with a Local Hamiltonian. *Physical Review A*, **105**:L021302, 2022a. (Cited on page 69.)

S. Manna, S. Nandy, and B. Roy. Higher-order Topological Phases on Fractal Lattices. *Physical Review B*, **105**:L201301, 2022b. (Cited on page 69.)

P. Massignan, M. Zaccanti, and G. M. Bruun. Polarons, Dressed Molecules and Itinerant Ferromagnetism in Ultracold Fermi Gases. *Reports on Progress in Physics*, **77**:034401, 2014. (Cited on page 34.)

N. Matveeva and G. E. Astrakharchik. One-dimensional Multicomponent Fermi Gas in a Trap: Quantum Monte Carlo Study. *New Journal of Physics*, **18**:065009, 2016. (Cited on page 35.)

R. Menchon-Enrich, A. Llobera, V. J. Cadarso, J. Mompart, and V. Ahufinger. Adiabatic Passage of Light in CMOS-Compatible Silicon Oxide Integrated Rib Waveguides. *IEEE Photonics Technology Letters*, **24**:536–538, 2012. (Cited on page 94.)

R. Menchon-Enrich, A. Llobera, J. Vila-Planas, V. J. Cadarso, J. Mompart, and V. Ahufinger. Light Spectral Filtering Based on Spatial Adiabatic Passage. *Light: Science & Applications*, **2**:e90–e90, 2013. (Cited on page 94.)

R. Menchon-Enrich, A. Benseny, V. Ahufinger, A. D. Greentree, T. Busch, and J. Mompart. Spatial Adiabatic Passage: A Review of Recent Progress. *Reports on Progress in Physics*, **79**:074401, 2016. (Cited on page 94.)

H. D. Meyer, U. Manthe, and L. S. Cederbaum. The Multi-Configurational Time-Dependent Hartree Approach. *Chemical Physics Letters*, **165**:73–78, 1990. (Cited on page 8.)

S. I. Mistakidis, A. G. Volosniev, and P. Schmelcher. Induced Correlations between Impurities in a One-Dimensional Quenched Bose Gas. *Physical Review Research*, **2**: 023154, 2020. (Cited on page 43.)

S. I. Mistakidis, A. G. Volosniev, R. E. Barfknecht, T. Fogarty, Th. Busch, A. Foerster, P. Schmelcher, and N. T. Zinner. Few-body Bose Gases in Low Dimensions—A Laboratory for Quantum Dynamics. *Physics Reports*, **1042**:1–108, 2023. (Cited on page 1.)

J. Monsel, M. Fellous-Asiani, B. Huard, and A. Auffèves. The Energetic Cost of Work Extraction. *Physical Review Letters*, **124**:130601, 2020. (Cited on page 94.)

L. F. C. Moraes, A. Saguia, A. C. Santos, and M. S. Sarandy. Charging Power and Stability of Always-on Transitionless Driven Quantum Batteries. *Europhysics Letters*, **136**:23001, 2021. (Cited on page 94.)

P. Mujal, E. Sarlé, A. Polls, and B. Juliá-Díaz. Quantum Correlations and Degeneracy of Identical Bosons in a Two-Dimensional Harmonic Trap. *Physical Review A*, **96**:043614, 2017. (Cited on page 43.)

S. Murmann, A. Bergschneider, V. M. Klinkhamer, G. Zürn, T. Lompe, and S. Jochim. Two Fermions in a Double Well: Exploring a Fundamental Building Block of the Hubbard Model. *Physical Review Letters*, **114**:080402, 2015. (Cited on page 94.)

N. M. Myers, O. Abah, and S. Deffner. Quantum Thermodynamic Devices: From Theoretical Proposals to Experimental Reality. *AVS Quantum Science*, **4**:027101, 2022. (Cited on page 93.)

S. Nascimbène, N. Navon, K. J. Jiang, L. Tarruell, M. Teichmann, J. McKeever, F. Chevy, and C. Salomon. Collective Oscillations of an Imbalanced Fermi Gas: Axial Compression Modes and Polaron Effective Mass. *Physical Review Letters*, **103**:170402, 2009. (Cited on page 33.)

M. Olshanii. Atomic Scattering in the Presence of an External Confinement and a Gas of Impenetrable Bosons. *Physical Review Letters*, **81**:938–941, 1998. (Cited on page 35.)

M. Olshanii and V. Dunjko. Short-Distance Correlation Properties of the Lieb-Liniger System and Momentum Distributions of Trapped One-Dimensional Atomic Gases. *Physical Review Letters*, **91**:090401, 2003. (Cited on page 43.)

S. Pai and A. Prem. Topological States on Fractal Lattices. *Physical Review B*, **100**:155135, 2019. (Cited on page 69.)

B. Pal and K. Saha. Flat Bands in Fractal-like Geometry. *Physical Review B*, **97**:195101, 2018. (Cited on page 72.)

B. Paredes, A. Widera, V. Murg, O. Mandel, S. Fölling, I. Cirac, G. V. Shlyapnikov, T. W. Hänsch, and I. Bloch. Tonks–Girardeau Gas of Ultracold Atoms in an Optical Lattice. *Nature*, **429**:277–281, 2004. (Cited on page 35.)

D. Pęcak, A. S. Dehkharghani, N. T. Zinner, and T. Sowiński. Four Fermions in a One-Dimensional Harmonic Trap: Accuracy of a Variational-Ansatz Approach. *Physical Review A*, **95**:053632, 2017. (Cited on page 15.)

W. D. Phillips. Nobel Lecture: Laser Cooling and Trapping of Neutral Atoms. *Reviews of Modern Physics*, **70**:721–741, 1998. (Cited on page 2.)

M. Planck. Zur Theorie des Gesetzes der Energieverteilung im Normalspektrum. *Verhandlungen der Deutschen Physikalischen Gesellschaft*, **2**:237–245, 1900. (Cited on page 1.)

M. Płodzień, D. Wiater, A. Chrostowski, and T. Sowiński. Numerically Exact Approach to Few-Body Problems Far from a Perturbative Regime. arXiv:1803.08387, 2018. (Cited on pages 5 and 21.)

H. Pu and N. P. Bigelow. Properties of Two-Species Bose Condensates. *Physical Review Letters*, **80**:1130–1133, 1998. (Cited on page 66.)

M. Pyzh, S. Krönke, C. Weitenberg, and P. Schmelcher. Spectral Properties and Breathing Dynamics of a Few-Body Bose–Bose Mixture in a 1D Harmonic Trap. *New Journal of Physics*, **20**:015006, 2018. (Cited on page 15.)

J. Q. Quach and W. J. Munro. Using Dark States to Charge and Stabilize Open Quantum Batteries. *Physical Review Applied*, **14**:024092, 2020. (Cited on page 94.)

J. Q. Quach, K. E. McGhee, L. Ganzer, D. M. Rouse, B. W. Lovett, E. M. Gauger, J. Keeling, G. Cerullo, D. G. Lidzey, and T. Virgili. Superabsorption in an Organic Microcavity: Toward a Quantum Battery. *Science Advances*, **8**:eabk3160, 2022. (Cited on page 93.)

R. Rammal and G. Toulouse. Random Walks on Fractal Structures and Percolation Clusters. *Journal de Physique Lettres*, **44**:13–22, 1983. (Cited on page 69.)

L. Rammelmüller, W. J. Porter, J. Braun, and J. E. Drut. Evolution from Few- to Many-Body Physics in One-Dimensional Fermi Systems: One- and Two-Body Density Matrices and Particle-Partition Entanglement. *Physical Review A*, **96**:033635, 2017. (Cited on page 8.)

L. Rammelmüller, D. Huber, and A. G. Volosniev. A Modular Implementation of an Effective Interaction Approach for Harmonically Trapped Fermions in 1D. *SciPost Physics Codebases*, 012, 2023. (Cited on page 5.)

D. Raventós, T. Graß, M. Lewenstein, and B. Juliá-Díaz. Cold Bosons in Optical Lattices: A Tutorial for Exact Diagonalization. *Journal of Physics B: Atomic, Molecular and Optical Physics*, **50**:113001, 2017. (Cited on pages 5, 8, and 33.)

L. Razzoli, M. G. A. Paris, and P. Bordone. Continuous-time Quantum Walks on Planar Lattices and the Role of the Magnetic Field. *Physical Review A*, **101**:032336, 2020. (Cited on pages 70 and 77.)

I. Reshodko, A. Benseny, and T. Busch. Robust Boson Dispenser: Quantum State Preparation in Interacting Many-Particle Systems. *Physical Review A*, **96**:023606, 2017. (Cited on page 99.)

C. Rodríguez, D. Rosa, and J. Olle. Artificial Intelligence Discovery of a Charging Protocol in a Micromaser Quantum Battery. *Physical Review A*, **108**:042618, 2023. (Cited on page 93.)

A. Rojo-Francàs, A. Polls, and B. Juliá-Díaz. Static and Dynamic Properties of a Few Spin 1/2 Interacting Fermions Trapped in a Harmonic Potential. *Mathematics*, **8**:1196, 2020. (Cited on pages 5, 15, and 36.)

A. Rojo-Francàs, F. Isaule, and B. Juliá-Díaz. Direct Diagonalization Method for a Few Particles Trapped in Harmonic Potentials. *Physical Review A*, **105**:063326, 2022. (Cited on pages 3, 5, 24, and 36.)

A. Rojo-Francàs, F. Isaule, and B. Juliá-Díaz. Few Particles with an Impurity in a One-Dimensional Harmonic Trap. *Physica Scripta*, **99**:045408, 2024a. (Cited on page 3.)

A. Rojo-Francàs, F. Isaule, A. C. Santos, B. Juliá-Díaz, and N. T. Zinner. Stable Collective Charging of Ultracold-Atom Quantum Batteries. *Physical Review A*, **110**:032205, 2024b. (Cited on page 4.)

A. Rojo-Francàs, P. Pansari, U. Bhattacharya, B. Juliá-Díaz, and T. Grass. Anomalous Quantum Transport in Fractal Lattices. *Communications Physics*, **7**:1–8, 2024c. (Cited on page 3.)

D. Rosa, D. Rossini, G. M. Andolina, M. Polini, and M. Carrega. Ultra-stable Charging of Fast-Scrambling SYK Quantum Batteries. *Journal of High Energy Physics*, **2020**:67, 2020. (Cited on page 93.)

H. H. Rosenbrock. A Variational Principle for Quantum Mechanics. *Physics Letters A*, **110**:343–346, 1985. (Cited on page 5.)

D. Rossini, G. M. Andolina, and M. Polini. Many-body Localized Quantum Batteries. *Physical Review B*, **100**:115142, 2019. (Cited on page 94.)

D. Rossini, G. M. Andolina, D. Rosa, M. Carrega, and M. Polini. Quantum Advantage in the Charging Process of Sachdev-Ye-Kitaev Batteries. *Physical Review Letters*, **125**: 236402, 2020. (Cited on page 93.)

J. Roßnagel, S. T. Dawkins, K. N. Tolazzi, O. Abah, E. Lutz, F. Schmidt-Kaler, and K. Singer. A Single-Atom Heat Engine. *Science*, **352**:325–329, 2016. (Cited on page 93.)

J. Rotureau. Interaction for the Trapped Fermi Gas from a Unitary Transformation of the Exact Two-Body Spectrum. *The European Physical Journal D*, **67**:153, 2013. (Cited on page 5.)

G. Roux, S. Capponi, P. Lecheminant, and P. Azaria. Spin 3/2 Fermions with Attractive Interactions in a One-Dimensional Optical Lattice: Phase Diagrams, Entanglement Entropy, and the Effect of the Trap. *The European Physical Journal B*, **68**:293–308, 2009. (Cited on page 33.)

J. L. Rubio, V. Ahufinger, Th. Busch, and J. Mompart. Optimal Conditions for Spatial Adiabatic Passage of a Bose-Einstein Condensate. *Physical Review A*, **94**:053606, 2016. (Cited on page 94.)

A. C. Santos, B. Çakmak, S. Campbell, and N. T. Zinner. Stable Adiabatic Quantum Batteries. *Physical Review E*, **100**:032107, 2019. (Cited on pages 93, 94, and 97.)

A. C. Santos, A. Saguia, and M. S. Sarandy. Stable and Charge-Switchable Quantum Batteries. *Physical Review E*, **101**:062114, 2020. (Cited on page 94.)

F. Schäfer, T. Fukuhara, S. Sugawa, Y. Takasu, and Y. Takahashi. Tools for Quantum Simulation with Ultracold Atoms in Optical Lattices. *Nature Reviews Physics*, **2**:411–425, 2020. (Cited on page 1.)

A. Schirotzek, C.-H. Wu, A. Sommer, and M. W. Zwierlein. Observation of Fermi Polarons in a Tunable Fermi Liquid of Ultracold Atoms. *Physical Review Letters*, **102**: 230402, 2009. (Cited on page 33.)

E. Schrödinger. An Undulatory Theory of the Mechanics of Atoms and Molecules. *Physical Review*, **28**:1049–1070, 1926. (Cited on page 1.)

F. Serwane, G. Zürn, T. Lompe, T. B. Ottenstein, A. N. Wenz, and S. Jochim. Deterministic Preparation of a Tunable Few-Fermion System. *Science*, **332**:336–338, 2011. (Cited on pages 33 and 34.)

V. Shaghaghi, V. Singh, G. Benenti, and D. Rosa. Micromasers as Quantum Batteries. *Quantum Science and Technology*, **7**:04LT01, 2022. (Cited on page 93.)

J. Shang, Y. Wang, M. Chen, J. Dai, X. Zhou, J. Kuttner, G. Hilt, X. Shao, J. M. Gottfried, and K. Wu. Assembling Molecular Sierpiński Triangle Fractals. *Nature Chemistry*, **7**: 389–393, 2015. (Cited on page 69.)

C. E. Shannon. A Mathematical Theory of Communication. *The Bell System Technical Journal*, **27**:379–423, 1948. (Cited on page 86.)

B. W. Shore. Picturing Stimulated Raman Adiabatic Passage: A STIRAP Tutorial. *Advances in Optics and Photonics*, **9**:563–719, 2017. (Cited on page 94.)

C. Sire, B. Passaro, and V. G. Benza. Electronic Properties of 2D Quasicrystals: Level Spacing Distribution and Diffusion. *Journal of Non-Crystalline Solids*, **153-154**:420–424, 1993. (Cited on page 72.)

W.-L. Song, H.-B. Liu, B. Zhou, W.-L. Yang, and J.-H. An. Remote Charging and Degradation Suppression for the Quantum Battery. *Physical Review Letters*, **132**:090401, 2024. (Cited on page 93.)

T. Sowiński and M. Á. García-March. One-dimensional Mixtures of Several Ultracold Atoms: A Review. *Reports on Progress in Physics*, **82**:104401, 2019. (Cited on page 2.)

T. Sowiński, M. Brewczyk, M. Gajda, and K. Rzążewski. Dynamics and Decoherence of Two Cold Bosons in a One-Dimensional Harmonic Trap. *Physical Review A*, **82**:053631, 2010. (Cited on page 15.)

T. Sowiński, T. Grass, O. Dutta, and M. Lewenstein. Few Interacting Fermions in a One-Dimensional Harmonic Trap. *Physical Review A*, **88**:033607, 2013. (Cited on page 33.)

H. T. Stoof, K. B. Gubbels, and D. B. Dickerscheid. *Ultracold Quantum Fields*. Springer Dordrecht, 2009. (Cited on page 20.)

S. Taie, R. Yamazaki, S. Sugawa, and Y. Takahashi. An SU(6) Mott Insulator of an Atomic Fermi Gas Realized by Large-Spin Pomeranchuk Cooling. *Nature Physics*, **8**:825–830, 2012. (Cited on page 34.)

S. Taie, T. Ichinose, H. Ozawa, and Y. Takahashi. Spatial Adiabatic Passage of Massive Quantum Particles in an Optical Lieb Lattice. *Nature Communications*, **11**:257, 2020. (Cited on page 94.)

H. Tang, X.-F. Lin, Z. Feng, J.-Y. Chen, J. Gao, K. Sun, C.-Y. Wang, P.-C. Lai, X.-Y. Xu, Y. Wang, L.-F. Qiao, A.-L. Yang, and X.-M. Jin. Experimental Two-Dimensional Quantum Walk on a Photonic Chip. *Science Advances*, **4**:eaat3174, 2018. (Cited on page 70.)

W. Tian, W. J. Wee, A. Qu, B. J. M. Lim, P. R. Datla, V. P. W. Koh, and H. Loh. Parallel Assembly of Arbitrary Defect-Free Atom Arrays with a Multitweezer Algorithm. *Physical Review Applied*, **19**:034048, 2023. (Cited on page 69.)

E. C. Titchmarsh. Some Integrals Involving Hermite Polynomials. *Journal of the London Mathematical Society*, **s1-23**:15–16, 1948. (Cited on page 15.)

L. Tonks. The Complete Equation of State of One, Two and Three-Dimensional Gases of Hard Elastic Spheres. *Physical Review*, **50**:955–963, 1936. (Cited on page 35.)

C. Trefzger, C. Menotti, B. Capogrosso-Sansone, and M. Lewenstein. Ultracold Dipolar Gases in Optical Lattices. *Journal of Physics B: Atomic, Molecular and Optical Physics*, **44**: 193001, 2011. (Cited on page 33.)

E. van Veen, S. Yuan, M. I. Katsnelson, M. Polini, and A. Tomadin. Quantum Transport in Sierpinski Carpets. *Physical Review B*, **93**:115428, 2016. (Cited on page 72.)

A. Venegas-Gomez, J. Schachenmayer, A. S. Buyskikh, W. Ketterle, M. L. Chiofalo, and A. J. Daley. Adiabatic Preparation of Entangled, Magnetically Ordered States with Cold Bosons in Optical Lattices. arXiv:2003.10905, 2020. (Cited on page 33.)

F. Verstraete, V. Murg, and J. Cirac. Matrix Product States, Projected Entangled Pair States, and Variational Renormalization Group Methods for Quantum Spin Systems. *Advances in Physics*, **57**:143–224, 2008. (Cited on page 5.)

J. Viana-Gomes and N. M. R. Peres. Solution of the Quantum Harmonic Oscillator plus a Delta-Function Potential at the Origin: The *Oddness* of Its Even-Parity Solutions. *European Journal of Physics*, **32**:1377–1384, 2011. (Cited on page 1.)

N. V. Vitanov, A. A. Rangelov, B. W. Shore, and K. Bergmann. Stimulated Raman Adiabatic Passage in Physics, Chemistry, and Beyond. *Reviews of Modern Physics*, **89**: 015006, 2017. (Cited on page 94.)

J. Vlietinck, J. Ryckebusch, and K. Van Houcke. Quasiparticle Properties of an Impurity in a Fermi Gas. *Physical Review B*, **87**:115133, 2013. (Cited on page 34.)

U. Vogl and M. Weitz. Laser Cooling by Collisional Redistribution of Radiation. *Nature*, **461**:70–73, 2009. (Cited on page 2.)

A. G. Volosniev and H.-W. Hammer. Analytical Approach to the Bose-polaron Problem in One Dimension. *Physical Review A*, **96**:031601, 2017. (Cited on page 34.)

X. R. Wang. Localization in Fractal Spaces: Exact Results on the Sierpinski Gasket. *Physical Review B*, **51**:9310–9313, 1995. (Cited on page 72.)

A. Weiße and H. Fehske. Exact Diagonalization Techniques. In *Computational Many-Particle Physics*, pages 529–544. Springer, 2008. (Cited on page 5.)

A. N. Wenz, G. Zürn, S. Murmann, I. Brouzos, T. Lompe, and S. Jochim. From Few to Many: Observing the Formation of a Fermi Sea One Atom at a Time. *Science*, **342**: 457–460, 2013. (Cited on page 33.)

M. Will and M. Fleischhauer. Dynamics of Polaron Formation in 1D Bose Gases in the Strong-Coupling Regime. *New Journal of Physics*, **25**:083043, 2023. (Cited on pages 53 and 66.)

M. Will, G. E. Astrakharchik, and M. Fleischhauer. Polaron Interactions and Bipolarons in One-Dimensional Bose Gases in the Strong Coupling Regime. *Physical Review Letters*, **127**:103401, 2021. (Cited on page 66.)

K. Wu and H. Simon. Thick-Restart Lanczos Method for Large Symmetric Eigenvalue Problems. *SIAM Journal on Matrix Analysis and Applications*, **22**:602–616, 2000. (Cited on page 9.)

J. Xu, T. Feng, and Q. Gu. Spin Dynamics of Large-Spin Fermions in a Harmonic Trap. *Annals of Physics*, **379**:175–186, 2017a. (Cited on page 33.)

X.-Y. Xu, X.-W. Wang, D.-Y. Chen, C. M. Smith, and X.-M. Jin. Quantum Transport in Fractal Networks. *Nature Photonics*, **15**:703–710, 2021. (Cited on pages 69, 70, 77, 78, and 79.)

Y.-L. Xu, X.-M. Kong, Z.-Q. Liu, and C.-C. Yin. Scaling of Entanglement during the Quantum Phase Transition for Ising Spin Systems on Triangular and Sierpiński Fractal Lattices. *Physical Review A*, **95**:042327, 2017b. (Cited on page 70.)

X. Yang, Y.-H. Yang, M. Alimuddin, R. Salvia, S.-M. Fei, L.-M. Zhao, S. Nimmrichter, and M.-X. Luo. Battery Capacity of Energy-Storing Quantum Systems. *Physical Review Letters*, **131**:030402, 2023. (Cited on page 93.)

H. Yi. Quantum Critical Behavior of the Quantum Ising Model on Fractal Lattices. *Physical Review E*, **91**:012118, 2015. (Cited on page 70.)

X. Yin, X.-W. Guan, M. T. Batchelor, and S. Chen. Effective Super Tonks-Girardeau Gases as Ground States of Strongly Attractive Multicomponent Fermions. *Physical Review A*, **83**:013602, 2011. (Cited on page 35.)

A. Zeilinger. Experiment and the Foundations of Quantum Physics. *Reviews of Modern Physics*, **71**:S288–S297, 1999. (Cited on page 1.)

X. Zhang, M. Bishof, S. L. Bromley, C. V. Kraus, M. S. Safronova, P. Zoller, A. M. Rey, and J. Ye. Spectroscopic Observation of SU(N)-Symmetric Interactions in Sr Orbital Magnetism. *Science*, **345**:1467–1473, 2014. (Cited on page 34.)

Y. Zhang, L. Vidmar, and M. Rigol. Impenetrable SU(N) Fermions in One-Dimensional Lattices. *Physical Review A*, **98**:042129, 2018. (Cited on page 34.)

Y. Zhang, L. Vidmar, and M. Rigol. Quantum Dynamics of Impenetrable SU(N) Fermions in One-Dimensional Lattices. *Physical Review A*, **99**:063605, 2019. (Cited on page 34.)

F. Zhao, F.-Q. Dou, and Q. Zhao. Quantum Battery of Interacting Spins with Environmental Noise. *Physical Review A*, **103**:033715, 2021. (Cited on page 94.)

N. T. Zinner, A. G. Volosniev, D. V. Fedorov, A. S. Jensen, and M. Valiente. Fractional Energy States of Strongly Interacting Bosons in One Dimension. *Europhysics Letters*, **107**:60003, 2014. (Cited on pages 56, 57, 58, 59, 60, 63, and 64.)

S. Zöllner, H.-D. Meyer, and P. Schmelcher. Correlations in Ultracold Trapped Few-Boson Systems: Transition from Condensation to Fermionization. *Physical Review A*, **74**: 063611, 2006. (Cited on pages 5 and 33.)

G. Zürn, F. Serwane, T. Lompe, A. N. Wenz, M. G. Ries, J. E. Bohn, and S. Jochim. Fermionization of Two Distinguishable Fermions. *Physical Review Letters*, **108**:075303, 2012. (Cited on page 33.)